Detection of Gamma Rays from the Supernova Remnant RX J0852.0-4622 with H.E.S.S.

DISSERTATION

zur Erlangung des akademischen Grades
doctor rerum naturalium
(Dr. rer. nat.)
im Fach Physik

eingereicht an der
Mathematisch-Naturwissenschaftlichen Fakultät I
Humboldt-Universität zu Berlin

von
Herr Dipl.-Phys. Nukri Randolf Komin
geboren am 20.07.1973 in Berlin

Präsident der Humboldt-Universität zu Berlin:
in Vertretung Prof. Dr. Hans Jürgen Prömel

Dekan der Mathematisch-Naturwissenschaftlichen Fakultät I:
Prof. Thomas Buckhout, PhD

Gutachter:

1. Prof. Dr. Thomas Lohse
2. Prof. Dr. Hermann Kolanoski
3. Prof. Dr. Uli Katz

eingereicht am:	13. September 2005
Tag der mündlichen Prüfung:	25. Oktober 2005

Abstract

Shell-type supernova remnants are discussed to be a main source of the galactic cosmic rays. Very high energy γ-rays (energies between 30 GeV and 30 TeV) from these objects are a tracer for the acceleration of particles. Up to now, only a limited number of supernova remnants were observed in γ-rays. This work reports on the observations of γ-rays from the shell-type supernova remnant RX J0852.0−4622 carried out with the **H**igh **E**nergy **S**tereoscopic **S**ystem in February 2004.

H.E.S.S., a system of four imaging Cherenkov telescopes, is dedicated to the observation of γ-rays of energies between 100 GeV and several tens of TeV. It is currently the most sensitive instrument in its energy range. A source of the strength of the Crab Nebula can be detected with a significance of $5\,\sigma$ within 6 minutes. The direction of a single γ-ray can be reconstructed with an angular resolution of better than 0.1°. The energy of the γ-rays can be estimated with an accuracy of $\approx 20\%$.

Emission of γ-rays from RX J0852.0−4622 was detected with a significance of $12\,\sigma$ within a live time of 3.2 h. The morphology of the emission region is clearly extended and correlated with the morphology of the X-ray emission. A differential energy spectrum of the photon flux between 0.5 and 10 TeV was reconstructed. It is found to follow a power law $\mathrm{d}N/\mathrm{d}E \propto E^{-\Gamma}$ with a spectral index of $\Gamma = 2.1 \pm 0.1_{\mathrm{stat}} \pm 0.2_{\mathrm{syst}}$. The integral photon flux above 1 TeV from the entire remnant is $(1.9 \pm 0.3_{\mathrm{stat}} \pm 0.4_{\mathrm{syst}}) \times 10^{-11}\,\mathrm{cm}^{-2}\mathrm{s}^{-1}$ which is at the level of the Crab flux at these energies, establishing RX J0852.0−4622 as one of the brightest γ-ray sources in the sky. RX J0852.0−4622 is the second supernova remnant of which an extended γ-ray morphology could be proved.

The emission of γ-rays from shell-type supernova remnants can be explained as being produced by accelerated electrons or protons. The observed energy flux in γ-rays between 0.5 and 10 TeV is calculated to be $(9 \pm 1_{\mathrm{stat}} \pm 2_{\mathrm{syst}}) \times 10^{-11}\,\mathrm{erg\,cm}^{-2}\,\mathrm{s}^{-1}$. Based on the energy flux in X-rays the expected energy flux due to inverse Compton scattering of relativistic electrons on the cosmic microwave background is estimated. It is found to be several orders of magnitude lower than the observed flux, suggesting that another radiation component significantly contributes to the γ-ray emission of RX J0852.0−4622.

In strong interactions of relativistic protons with the ambient interstellar material neutral pions are produced. The decay of these pions produce γ-rays. The distance to RX J0852.0−4622 and the density of the ambient interstellar material are open parameters in the interpretation. It is shown for a wide range of these parameters that the transfer of several percent of the kinetic energy of the supernova remnant ($\sim 10^{51}$ erg) to the acceleration of protons could explain the observed energy flux in γ-rays. Thus, it is likely that RX J0852.0$-$4622 contributes to the acceleration of galactic cosmic rays.

Keywords:
Gamma-Rays, Supernova Remnants, RX J0852.0-4622, H.E.S.S.

Zusammenfassung

Es wird angenommen, dass schalenartige Supernova-Reste wesentliche Quellen der galaktischen kosmischen Strahlung sind. Die Beschleunigung von Teilchen in diesen Objekten kann mit hochenergetischer γ-Strahlung (Energien zwischen 30 GeV und 30 TeV) nachgewiesen werden. In dieser Arbeit wird die Beobachtung von γ-Strahlung des schalenartigen Supernova-Restes RX J0852.0−4622 beschrieben. Diese Beobachtungen wurden im Februar 2004 mit dem **H**igh **E**nergy **S**tereoscopic **S**ystem durchgeführt.

H.E.S.S., ein System von vier abbildenden Cherenkov Teleskopen, kann γ-Strahlung im Bereich zwischen 100 GeV und einigen 10 TeV nachweisen. Zur Zeit ist H.E.S.S. das leistungsfähigste Instrument in seinem Energiebereich. Eine Quelle in der Stärke des Krebsnebels kann mit einer Signifikanz von $5\,\sigma$ innerhalb von 6 Minuten nachgewiesen werden. Die Richtung eines einzelnen Photons der γ-Strahlung wird mit einer Winkelauflösung unter 0.1° rekonstruiert. Die Energie dieser Photonen wird mit einer Genauigkeit von etwa 20% bestimmt.

Die Emission von γ-Strahlung von RX J0852.0−4622 wurde mit einer Signifikanz von $12\,\sigma$ bei einer Belichtungszeit von 3.2 h nachgewiesen. Die Morphologie der Emissionsregion ist ausgedehnt und korreliert mit der Morphologie der Röntgenstrahlung. Ein differenzielles Energiespektrum des Photonenflusses wurde im Bereich zwischen 0.5 und 10 TeV rekonstruiert. Das Spektrum folgt einem Potenzgesetz $\mathrm{d}N/\mathrm{d}E \propto E^{-\Gamma}$ mit $\Gamma = 2.1 \pm 0.1_{\mathrm{stat}} \pm 0.2_{\mathrm{syst}}$. Der integrierte Photonenfluss oberhalb von 1 TeV ist $(1.9 \pm 0.3_{\mathrm{stat}} \pm 0.4_{\mathrm{syst}}) \times 10^{-11}\,\mathrm{cm}^{-2}\mathrm{s}^{-1}$, auf dem Niveau des Flusses des Krebsnebels. RX J0852.0−4622 ist daher eine der hellsten γ-Strahlungsquellen am Himmel und der zweite Supernova-Rest dessen ausgedehnte γ-Strahlungsemission nachgewiesen werden konnte.

γ-Strahlung kann in Supernova-Resten durch inverse Compton-Streuung von relativistischen Elektronen oder durch starke Wechselwirkungen von Protonen mit dem interstellaren Material erklärt werden. Mit Hilfe von Röntgenmessungen wurde der erwartete Energiefluss von inverser Compton-Streuung an der kosmischen Mikrowellenstrahlung abgeschätzt. Diese ist um einige Größenordnungen kleiner als der beobachtete Wert von $(9 \pm 1_{\mathrm{stat}} \pm 2_{\mathrm{syst}}) \times 10^{-11}\,\mathrm{erg}\,\mathrm{cm}^{-2}\,\mathrm{s}^{-1}$. Daher ist es wahrscheinlich, dass eine weitere Strahlungskomponente einen signifikanten Anteil an der γ-Strahlungsemission von RX J0852.0−4622 hat. Offene Parameter in der Interpretation als Strahlung aus Proton-Wechselwirkungen sind die Entfernung zu RX J0852.0−4622 sowie die Dichte des interstellaren Materials. In einem weiten Bereich dieser Parameter ist der Transfer von einigen Prozent der kinetischen Energie des Supernova-Restes ($\sim 10^{51}$ erg) in die Protonenbeschleunigung notwendig, um den beobachteten Energiefluss zu erklären. Daher ist es wahrscheinlich, dass RX J0852.0$-$4622 zur galaktischen kosmischen Strahlung beiträgt.

Schlagwörter:
Gammastrahlung, Supernova-Reste, RX J0852.0-4622, H.E.S.S.

Contents

List of Figures

List of Tables

“The people of Krikkit … are surrounded by a huge Dust Cloud,… , their single sun with its single world… Because of the Dust Cloud there has never been anything to see in the sky. At night it is totally blank. … They are hardly aware of the sky. It’s as if they had a blind spot that extend 180 degrees from horizon to horizon.”

(Douglas Adams, in “Life, the Universe and Everything”)

Introduction

If we step outside during a clear night we will see that the sky is scattered with points glowing in all colours and sizes — the stars. Surely, already in ancient times people must have seen this spectacular view. The sky was thought to be the heaven, a place other than Earth and inhabited by gods and other mythological figures. Still today, many constellations of stars are named after gods, demigods and legendary figures and things.

Early civilisations started to observe the movement of the celestial bodies across the sky. The first outcomes of these studies were calendars predicting the start of the seasons. For instance, the Egyptians used the star Sirius to predict the annual flooding of the Nile river and the beginning of the seeding time. Far-east astronomers observed “guest stars” brighter than any other star but appearing only for a few months. Today, some people believe that ancient artefacts, like the Sky Disc of Nebra, the Stone Henge in Cornwall, or the lines scratched into the desert near Nazca are the tools of ancient astronomy.

The periodicity of the movement of the celestial bodies across the sky let Aristotle and Ptolemy conclude, that these bodies are located on spheres circling the Earth. In the middle of the last millennium, Nicolaus Copernicus refined this theory putting the Sun into the centre of the Universe. In his world picture, the Sun is circled by the Earth, the Moon and the planets, surrounded by a sphere of stars. Galileo Galilei used one of the first optical telescopes for observing the sky. This marked a step forward for astronomical observations. Galilei discovered moons orbiting the planet Jupiter. These moons, still named Galilean satellites, are the first discovered objects which cannot be seen by the naked eye. The development of optical systems in the recent centuries led to the discovery of many different types of celestial objects, beside the stars there are nebulae and dust, arising and dying stars, and even huge formations of stars — galaxies like our own Milky Way. With the possibility to measure the distances to these objects it turned out that these objects are very far away. The light from the most distant objects needs billions of years to reach the Earth. In today’s view of the world, the

Universe might be infinitely large, has no centre, and our Sun is just one star out of myriads of others.

At the beginning of the last century it turned out that the visible light is just one small part of the entire electromagnetic spectrum. Telescopes were designed to extend the astronomic view and now the sky is observed in almost the entire spectrum. At the lowest energies the cosmic microwave background was detected, the remaining thermal radiation from one of the earliest epochs of the Universe. Radio observations led to the discovery of new types of objects, like pulsars — giant nuclei of neutrons. In infrared light, dust can be observed which forms discs around stars being the birth places of new planets. Objects of very high temperatures show up in X-rays. The "guest stars" observed by the far-east astronomers were explosions of old stars. The remnants of these explosions can be seen in X-rays. The light of very violent processes, which cannot be explained as being radiation of hot material, can be seen in high energy X-rays and γ-rays. At the highest currently observable energies the γ-rays are very sparse. Thus, large detectors are needed to observe this radiation. Astronomy at these energies developed in the recent twenty years. H.E.S.S., a system of four telescopes, uses a part of the upper atmosphere as detector volume to observe the sky at highest energies. It is currently the most sensitive instrument in its energy range, and it is dedicated to the studies of the most powerful objects in the Universe.

The cosmic rays, high energy ions hitting the Earth, are another evidence for the existence of violent processes in the Universe. Cosmic rays were discovered in 1912 and are extensively studied since then. Their origin is still unknown, among others the remnants of exploded stars — supernova remnants — are discussed to be sources of the cosmic rays.

The observations of γ-rays from supernova remnants can provide inside into the acceleration processes and could provide evidence for the production of cosmic rays. One such supernova remnants, RX J0852.0−4622, can be found in the southern sky in the constellation of Vela — the sails of the legendary ship Argo. In this work, the observations of RX J0852.0−4622 with H.E.S.S. will be laid out and the result will be discussed in terms of acceleration of cosmic rays.

About this Book

This work is organised as follows. The cosmic rays will be introduced shortly in chapter 1. A summary of previous observations at other wavelengths of the supernova remnant RX J0852.0−4622 is given in chapter 2. At the beginning of chapter 3, supernovae as the end stage of massive stars and the following evolution of their remnants are discussed. This is followed by the explanation of how particles can be accelerated in the shells of the supernova remnants. Different mechanisms lead to the production of γ-rays. These mechanisms will be explained and some estimations of the energy flux are made. The chapter concludes with the presentation of some useful relations which will be used in the analysis of the observed data. Cosmic γ-rays can be detected with H.E.S.S. The H.E.S.S. experiment is introduced in chapter 4 followed by a discussion of its performance using data of a standard candle. The observation of RX J0852.0$-$4622 and the analysis of the data is described in chapter 5. This chapter concludes with a summary of the observational results and a comparison with previous γ-ray observations. Finally, in chapter 6 the results are interpreted with respect to the acceleration of particles and the possibility of cosmic ray production. This chapter concludes with a short outlook on future works to be done.

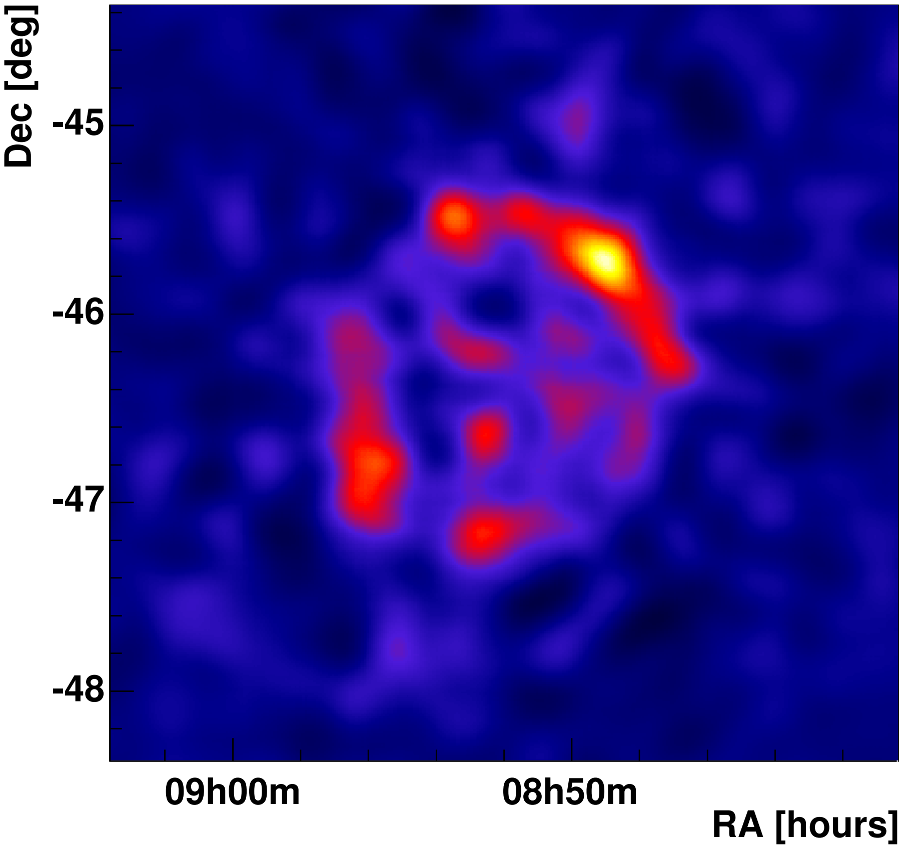

Figure 1: **The supernova remnant RX J0852.0−4622 in γ-rays.** The picture is smoothed with a Gaussian comparable with the angular resolution of H.E.S.S.

Chapter 1

Cosmic Rays

The Earth is exposed to ionising radiation from space. This radiation was discovered by Viktor Franz Hess during balloon flights in 1912 [Hes12]. He observed that electrometers discharge faster at higher altitudes. From his observations he drew the conclusion that this discharge is not provoked by radioactivity of elements at Earth but rather by radiation which enters the atmosphere from above.

Later experiments showed that the cosmic rays are composed mainly (98%) of nuclei and to a small amount (2%) of electrons [see e.g. KZ97]. The nucleonic component consists of $\approx 87\%$ of protons, $\approx 12\%$ of helium nuclei and $\approx 1\%$ of heavier nuclei.

1.1 Energy Spectrum

The energy spectrum of the cosmic rays is shown in Fig. 1.1. It extends over almost 13 decades in energy and the flux decreases from $\approx 10^4\,(\mathrm{m^2 sr\,s\,GeV})^{-1}$ at 10^8 eV down to $\approx 10^{-28}\,(\mathrm{m^2 sr\,s\,GeV})^{-1}$ at almost 10^{21} eV.

The spectrum can be divided into three different parts. The low energy part is affected by solar modulation. In this range, variations with the solar activity have been observed. In the region between 10^{10} and 10^{15} eV the flux follows a power law with a spectral index of ≈ 2.7. At an energy of 10^{15} eV the spectrum steepens. This region is called the "knee". Beyond the knee the spectrum has a spectral index of ≈ 3. Around $\approx 10^{18}$ eV the spectrum becomes flatter. This region is called the "ankle".

At around 10^{21} eV a cut-off of the cosmic ray spectrum is expected. This region is currently being studied in detail with new, large air shower experiments.

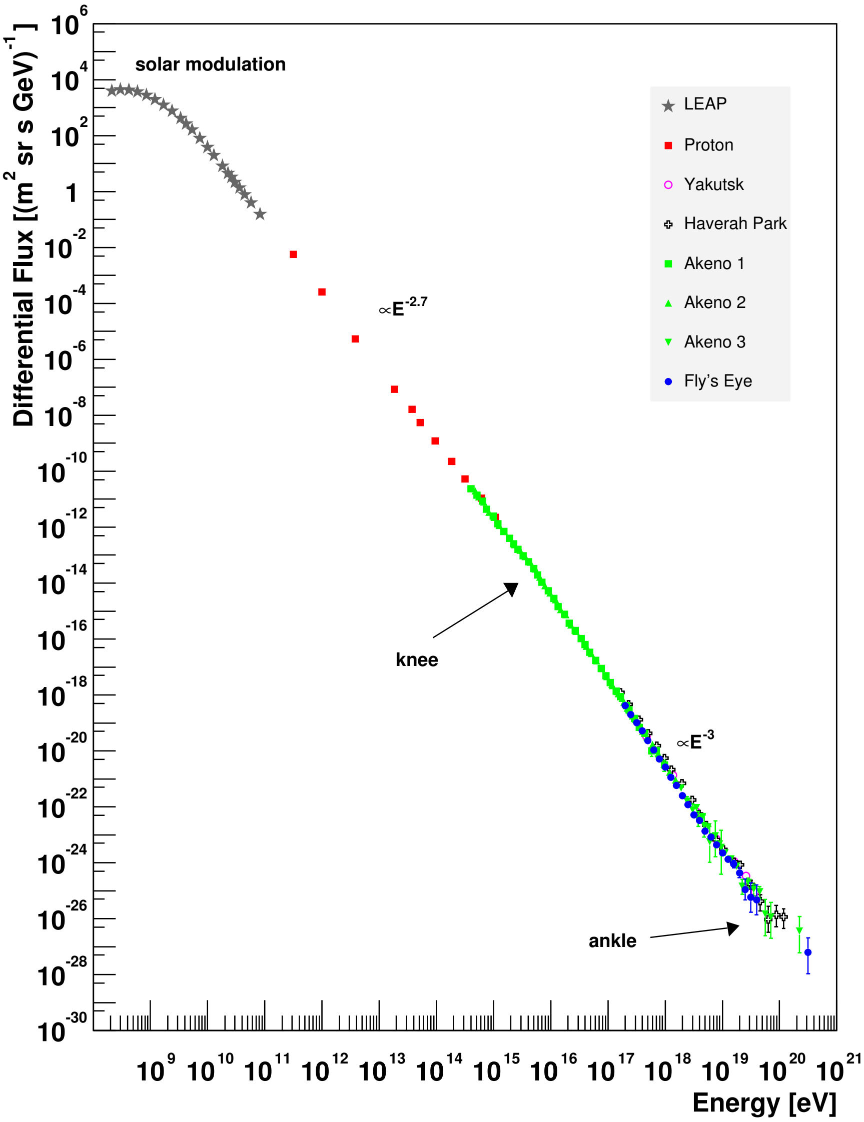

Figure 1.1: **The Spectrum of Cosmic Rays.** The compilation was made by **(author?)** [Swo97]. The individual measurements were made with the LEAP balloon experiment [SOS+91], the Proton satellite [Gri71], and the air shower arrays Yakutsk [Afa96], Haverah Park [LRW91], Akeno [NHH+84, NTM+92] and Fly's Eye [BCD+94].

1.2 Origin of the Cosmic Rays

The fact that the energy spectrum of the cosmic rays follows a power law over many decades of energy rules out that the particles originate from thermal processes. These particles must have been accelerated in cosmic accelerators to high energies, partially to energies which cannot be reached on Earth.

Up to now, the origin of the cosmic rays is unknown. Among others, candidates for cosmic accelerators are supernova remnants and pulsars as galactic sources and the jets of active galactic nuclei as extra-galactic sources.

The cosmic rays of energies up to the knee are thought to be mainly of galactic origin. The gyro-radius r_g of a high energy nucleus with atomic number Z and energy E in a magnetic field B is given by

$$r_\mathrm{g} \approx \frac{1}{Z}\left(\frac{E}{10^{15}\,\mathrm{eV}}\right)\left(\frac{B}{1\,\mu\mathrm{G}}\right)^{-1}\,\mathrm{pc}.$$

Particles with energies up to the knee are likely of galactic origin. A proton at the knee in the interstellar magnetic field ($B \approx 3\,\mu$G) has a gyro-radius of 0.3 parsec ($1\,\mathrm{pc} = 3 \times 10^{13}\,\mathrm{km}$). Thus, the magnetic field can easily confine the particle within the galaxy, which is roughly a disk with a radius of 15 kpc and a height of 300 pc.

At particle energies above 10^{15} eV the gyro-radius exceeds several parsecs and thus becomes larger than the size of galactic objects which are discussed to be cosmic accelerators. The steepening beyond the knee is discussed to represent the transition from galactic to extragalactic sources. Particles at high energies leave the galaxy more easily than low energy particles.

Particles at energies around 10^{19} eV are likely of extragalactic origin. Their gyro-radius in the interstellar magnetic field exceeds the radius of the galaxy and thus the magnetic field cannot confine these particles in the galaxy.

At around 10^{20} eV the protons have enough energy to interact with the photons of the cosmic microwave background:

$$\begin{aligned} p + \gamma \rightarrow \quad \Delta^+ \quad &\rightarrow p + \pi^0 \\ p + \gamma \rightarrow \quad \Delta^+ \quad &\rightarrow n + \pi^+. \end{aligned}$$

In these processes the protons lose energy due to pion production, and therefore no particles with higher energies are expected to be observed. This is called Greisen-Zatsepin-Kuzmin (GZK) cut-off [Gre66]. This region of the spectrum is currently controversially discussed. Recent measurements suggest the existence of a cut-off while other experiments report observations of particles with energies beyond the cut-off. It should be noted that the recent measurements are not shown in Fig. 1.1.

1.3 Supernova Remnants as Source of Cosmic Rays

Based on simple energetic considerations, **(author?)** [GS64] suggested that supernova explosions are the sources of galactic cosmic rays. From the measured flux spectrum, which is shown in Fig. 1.1, the energy density of the cosmic rays can be calculated. It is found to be $\epsilon_{\mathrm{CR}} \approx 1\,\mathrm{eV\,cm^{-3}}$ [WW89] or $1.6 \times 10^{-12}\,\mathrm{erg\,cm^{-3}}$. If one approximates the volume V of the galaxy as a cylinder with a radius of 15 kpc and a height of 300 pc one can calculate the power of the cosmic rays to be

$$L_{\mathrm{CR}} = \frac{V\epsilon_{\mathrm{CR}}}{\tau_{\mathrm{esc}}} \approx 3 \times 10^{40}\,\mathrm{erg\,s^{-1}}.$$

The time $\tau_{\mathrm{esc}} \approx 10^{7}\,\mathrm{y}$ is the mean escape time of the particles from the galaxy [see e.g. Gai90, chap. 9].

On the other hand, within our galaxy supernova explosions occur approximately every 30 years. Each supernova provides $\sim 10^{51}\,\mathrm{erg}$ of kinetic energy. Thus, supernova explosions provide a power of

$$L_{\mathrm{SN}} = \frac{10^{51}\,\mathrm{erg}}{30\,\mathrm{y}} \sim 10^{42}\,\mathrm{erg\,s^{-1}}.$$

It can immediately be seen that if supernovae would transfer a fraction of several percent to the acceleration of protons and nuclei they could deliver the entire cosmic ray power.

Chapter 2

The Supernova Remnant RX J0852.0−4622

One of the supernova remnants (SNRs) which could be a source of the galactic cosmic rays is RX J0852.0−4622[1] which was discovered in X-rays in 1998. In this chapter the detection of RX J0852.0−4622 and previous studies are presented.

2.1 Detection

RX J0852.0−4622 was discovered by **(author?)** [Asc98] in an All-Sky Survey carried out with the ROSAT X-ray satellite. The left panel of Fig. 2.1 shows a sky map of X-rays with energies between 0.1 and 2.4 keV from the Vela region of the sky. Emission of the old Vela supernova remnant can be seen clearly. The energy spectrum of the X-ray emission is dominated by thermal black-body radiation and is therefore interpreted as the emission of a hot plasma.

The right panel of Fig. 2.1 shows the same field of view but with energies restricted to above 1.3 keV. Most of the thermal radiation of the Vela SNR is suppressed. The non-thermal emission of the Vela pulsar can be seen at the centre of the picture. South-east of the pulsar (in the lower left corner) **(author?)** [Asc98] discovered a previously unknown supernova remnant. The emission is centred on (RA 8h52m3s, Dec $-46°22'$)[2], and therefore this supernova remnant was accordingly named RX J0852.0−4622.

---

[1] RX J0852.0−4622 is also known as G266.2−1.2 or "Vela Junior".

[2] All coordinates in this work are given in right ascension (RA) and declination (Dec) of epoch 2000. As the celestial sphere is viewed from inside, the right ascension counts from right to left and east is at the left hand side of the sky maps.

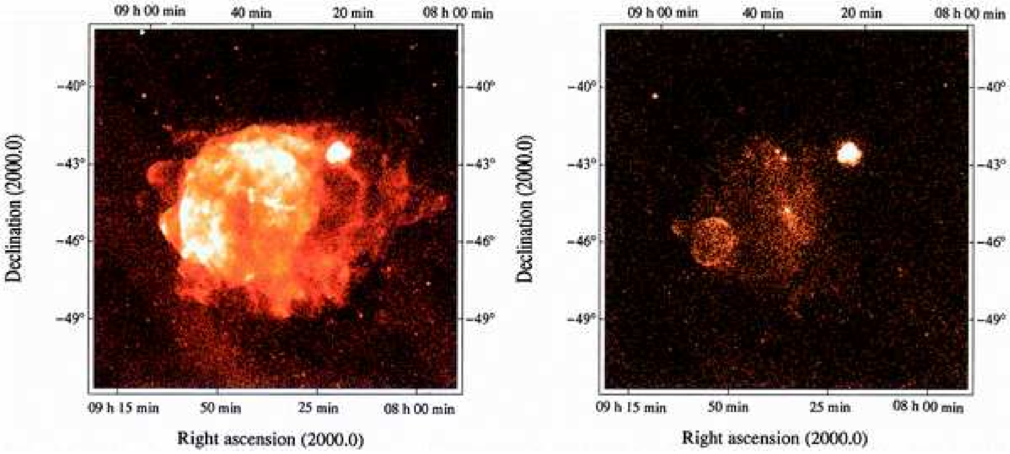

Figure 2.1: **ROSAT all-sky survey images of the Vela SNR.** The pictures show the Vela SNR as seen in X-rays by the ROSAT satellite. The left panel shows the X-ray emission in the energy range from 0.1 to 2.4 keV, the right panel X-rays with energies above 1.3 keV. The images were taken from [Asc98].

2.2 Morphology

The right panel of Fig. 2.2 shows a zoomed in map of the ROSAT data as obtained from the ROSAT data base [ROS05]. The data show a ring-like shell structure with an apparent diameter of 2°. Following the detection of RX J0852.0−4622 in X-rays it was target of radio observations and faint radio emission of the shell was detected [CRB99, DG00].

Further detailed X-ray studies of the remnant were carried out with the ASCA satellite [SHE$^+$01]. The ASCA data is shown in the left panel of Fig. 2.2. It should be noted that the ASCA observations did not cover the entire field of view. Strong emission can be seen from the northern, north-western and western parts of the shell whereof the north-western part is the brightest. In the centre of the ASCA data emission from the point-like source AX J0851.9−4617.4 can be seen.

The bright north-western region was target of detailed high-resolution observations in X-rays with the XMM-Newton [IAB$^+$05] and *Chandra* [BYH05] satellites. The picture obtained with XMM-Newton is shown in Fig. 2.3. A very bright filamentary structure defines the north-western boundary of the shell. Further inside a faint filament can be seen which seems to join the other structure at the north-eastern end. The *Chandra* data is shown in Fig. 2.4 confirming the detection of the two filaments. From the width

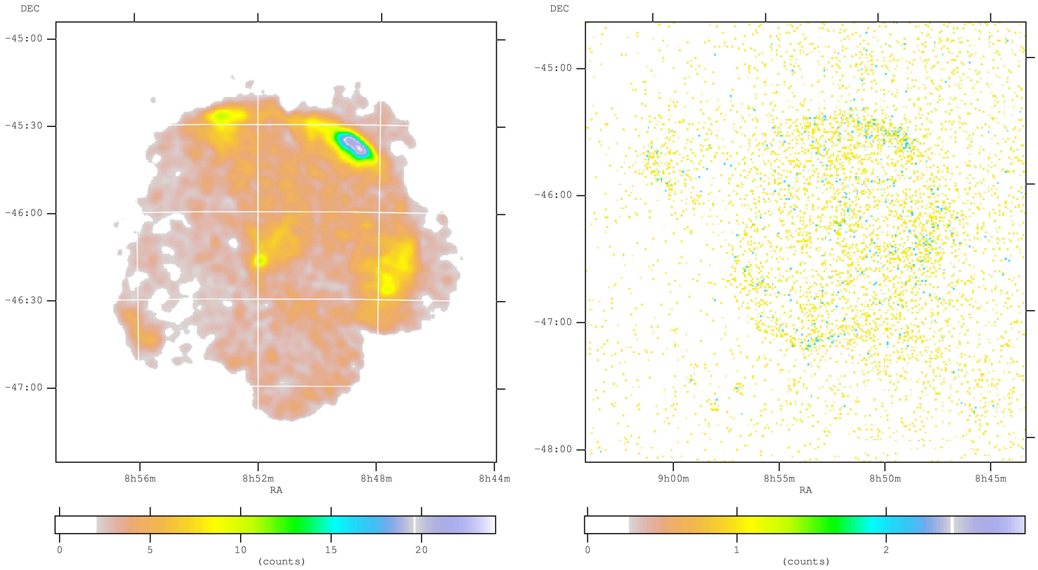

Figure 2.2: **X-ray images of RX J0852.0−4622.** Left panel: ASCA observations [SHE+01]. Note that the southern part is not completely covered by these observations. The energy range is 0.7-10 keV. Right panel: Data of the ROSAT All-Sky Survey with energies above 1.3 keV.

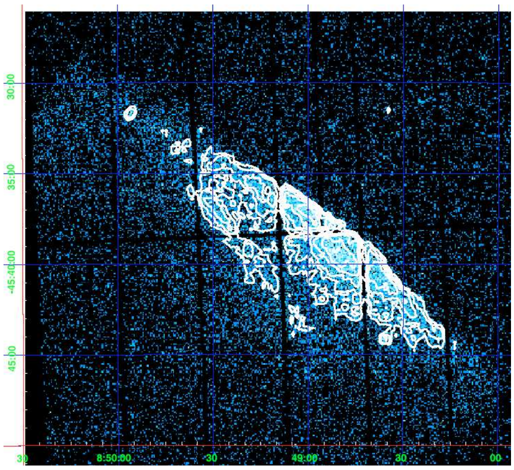

Figure 2.3: **XMM-Newton image of the NW rim.** The picture shows the north-western part of the shell in energies between 0.2 keV and 10 keV [IAB+05].

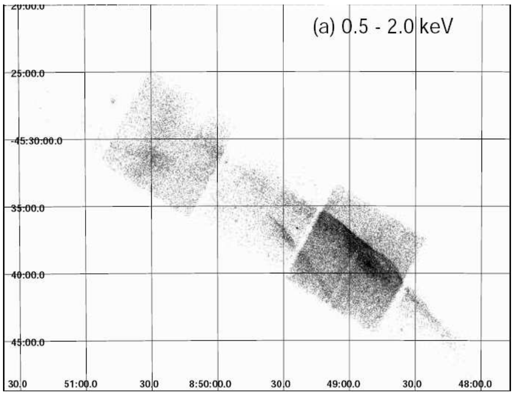

Figure 2.4: **Chandra image of the NW rim.** The picture shows the filamentary structure in the north-western part of the rim in energies between 0.5 keV and 2.0 keV [BYH05].

of these filaments **(author?)** [BYH05] derive a magnetic field in the shell of about $500\,\mu\mathrm{G}$ ($1\,\mathrm{G} = 10^{-4}\,\mathrm{T}$) .

2.3 Age of the SNR and its Distance to Earth

Observations with the COMPTEL telescope aboard the Compton Gamma Ray Observatory (CGRO) revealed ^{44}Ti decay lines [ISB^{+}98]. The titanium isotope ^{44}Ti is expected to be produced in supernovae. The relatively short live time of ^{44}Ti of about 90 years [NBC^{+}97] indicates that RX J0852.0−4622 is relatively young. The young age and the apparent large extension of the shell suggests that it is nearby. From the diameter as seen in X-rays, the measured ^{44}Ti flux and an assumed expansion velocity of $\approx 5000\,\mathrm{km\,s^{-1}}$ **(author?)** [ISB^{+}98] estimate the age and distance to be $\approx$ 680 years and $\approx$ 200 pc, respectively. This was confirmed later by **(author?)** [AIS99] who calculate the error on the age to be 100 years and set upper limits of 1100 years on the age and 500 pc on the distance.

In the north-western part of the shell an overabundance of calcium was detected [TMA^{+}00]. Arguing that the Ca is produced as decay product of the ^{44}Ti produced in the supernova explosion, **(author?)** [TMA^{+}00] calculate an age between 630 and 970 years independent of the measurement of the ^{44}Ti line emission. Recent measurements with the *Chandra* satellite suggest an age of 660^{+740}_{-240} years and a distance of 330^{+170}_{-70} pc [BYH05].

An independent and debatable estimate of the age was made using drilled antarctic ice cores. Ionising radiation of supernova explosions can produce nitrate when it impinges on the atmosphere. **(author?)** [RSZP79] identified three nitrate spikes in ice cores drilled at the South Pole station with recent supernova explosions. A fourth, unassigned nitrate spike was attributed by **(author?)** [BZ00] to the supernova explosion of RX J0852.0−4622 concluding an age of 700 years. **(author?)** [GS04] discuss recent works on the correlation of supernova explosions and nitrate abundances in ice cores concluding that their is no significant correlation.

All these measurements imply that RX J0852.0−4622 is one of the closest supernovae in recent human history and should have been observed by contemporaries. No historical records describing such an event were found [AIS99]. **(author?)** [AIS99] argue that assuming a sub-luminous supernova explosion (examples for sub-luminous supernovae are Cas A and SN 1181) the supernova would not have been bright enough to be visible during daylight. The supernova might have been missed if it occurred during the season when it is not visible during night. Additionally, the historical records [HH62] are not complete, **(author?)** [AIS99] identified three gaps whereof two are relevant for RX J0852.0−4622.

On the other hand, much larger distances are discussed which would explain the absence of historical records. Based on the relatively large absorption column in X-ray data, **(author?)** [SHE$^+$01] estimate the distance to RX J0852.0−4622 to be 1–2 kpc which would place RX J0852.0−4622 near the Vela Molecular Ridge, a cloud of molecular hydrogen.

No final conclusion on the distance to RX J0852.0−4622 can be drawn yet. The distance is a crucial ingredient in the interpretation of the γ-ray data from RX J0852.0−4622 and distances of ≈ 200 pc up to several kpc have to be considered.

2.4 Source of the X-ray Emission

The differential energy spectrum of the X-ray emission of RX J0852.0−4622 is described by a power law [Asc98, SHE$^+$01, IAB$^+$05, BYH05]. Thus, it cannot be thermal emission of a hot plasma. The emission can be interpreted as being synchrotron emission of high energy electrons. Radio emission of RX J0852.0−4622 is also discussed to be synchrotron radiation [CRB99].

Based on these measurements RX J0852.0−4622 can be regarded as an accelerator of electrons. The mechanism of accelerating charged particles in the shell of a supernova remnant and the sub-sequent synchrotron radiation will be explained in the next chapter.

2.5 Gamma-Ray Observations

Radiation of γ-rays of energies above 500 GeV coincident with the bright X-ray emission region in the north-western part of the shell was detected by the CANGAROO collaboration [KEK$^+$05]. The differential energy spectrum is relatively soft. The emission can be described as being inverse Compton radiation of electrons and positrons with an additional component of γ-rays from π^0-decays [KEK$^+$05].

The observation of RX J0852.0$-$4622 in γ-rays with the H.E.S.S. telescopes [AAB$^+$05a] will be discussed in detail in this work.

Chapter 3

Gamma Rays from Supernova Remnants

Supernova remnants are the leftovers of old exploded stars. In this chapter, the final stages of stars leading to supernova explosions are described. The remaining shells of this explosion expand into the interstellar medium. This expansion leads to the formation of shock fronts which are able to accelerate charged particles to high energies. The main emphasis is put on the production of very high energy photons which enable us to image these cosmic ray accelerators.

3.1 Supernova Explosions

Stars like our Sun initially produce energy in form of heat and radiation by fusing hydrogen to helium. The radiation pressure resists the gravitational force and prevents the star from collapsing. After about 10^7 years almost all of the hydrogen is fused. The radiation cannot resist the gravitational force anymore, and the star starts to contract. The contraction results in a rise of the temperature until the fusion of helium to carbon, oxygen and neon is initiated. This second step of fusion lasts about 10^5 years. Depending on the mass of the star, the fusion of heavier elements can be initiated in further contraction steps. Stars with masses of more than approximately 8 solar masses ($M_\odot \approx 2 \times 10^{30}\,\mathrm{kg}$) can burn their material up to the most stable element — iron. The last fusion steps are much shorter than the hydrogen and helium burning, the fusion of silicon to iron happens within a couple of days.

These massive stars in their late phase have an iron core. The core is surrounded by several shells. In the innermost shell silicon is fused to iron, in the next shell oxygen is fused to silicon and so on. In the outermost shell hydrogen is fused to helium like in the first stage of the star. As no energy can be gained from the fusion of iron, the stability of the core is kept up by the degeneracy pressure of the electrons rather than radiation. More and more iron falls onto the core until the Chandrasekhar mass limit, at which the electron degeneracy cannot resist the gravitational force anymore, is reached and the core collapses. The density and temperature rise, and protons and electrons produce neutrons and neutrinos via the inverse β-decay, $p + e^- \rightarrow n + \nu_e$.

The contraction goes on until the density in the core reaches nuclear densities, and the neutrons form a giant nucleus. The degeneracy of the neutrons now resists the gravitational force. Within a fraction of a second, the core forms a stable and compact object. This stiffening of the core results in a shock through the infalling outer layers of the star, and the outer layers are ejected. An energy of $\sim 10^{53}\,\mathrm{erg}$ ($1\,\mathrm{erg} = 10^{-7}\,\mathrm{J}$) is liberated in this explosion, and only a fraction of 1% is transformed into the kinetic energy of the ejected material. The rest of the energy is released as kinetic energy of the neutrinos. The ejected mass is heated, and heavier nuclei beyond iron can be produced in a process called explosive nucleosynthesis.

The neutron core remains as a neutron star if the neutron degeneracy can resist the gravitational force. Otherwise, the core further collapses into a singularity — a black hole.

Details of the end stage of massive stars and supernova explosions can be found in [KZ97, chap. 13.1] and [Lon94, chap. 15]. Detailed calculations of the different steps are laid out in [Pad01, chap. 4].

Supernovae of the described type are core collapse supernovae or type II supernovae. There is another important type of supernovae which occurs when a white dwarf accretes matter from a companion star. White dwarfs are stars consisting mainly of oxygen and carbon, and these stars have not sufficient mass to fuse these elements. The electron degeneracy resists the gravitational force and keeps up the stability of the star. Due to the accretion of matter from its companion, the mass of the white dwarf rises until it reaches the Chandrasekhar limit for white dwarfs, $M_{\mathrm{ch}} \approx 1.46 M_{\odot}$. The white dwarf collapses until the carbon burning is initiated. The star explodes and energy of $\sim 10^{51}\,\mathrm{erg}$ is released which mostly goes into the kinetic energy of the supernova remnant. The star is disrupted completely and no compact remnant is left. These supernovae are of type Ia. A short description of this process can be found in [Lon94, chap. 16.5.2] and [Pad01, chap. 7.8.2].

Even though these two types of supernovae are fairly different, there are some similarities between them. In both processes a stellar explosion ejects material into the interstellar space with a kinetic energy in the order of

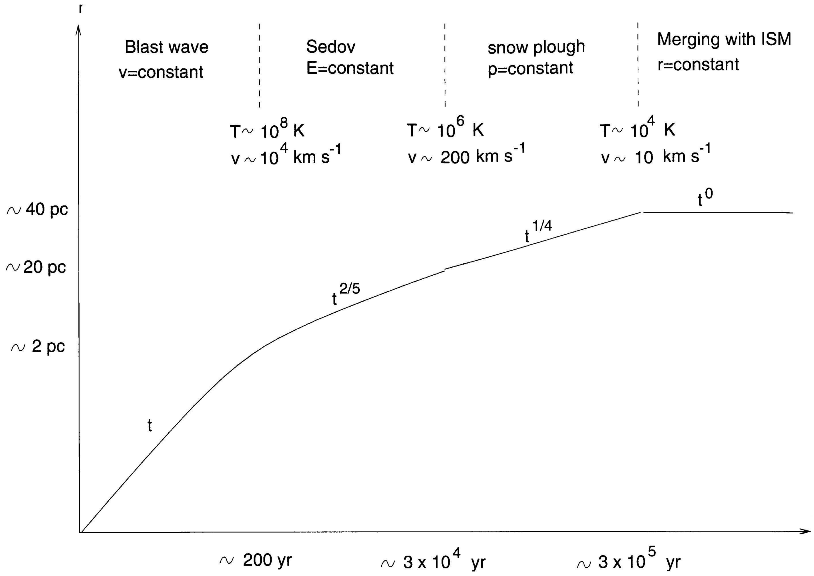

Figure 3.1: **Evolution of a supernova remnant.** The picture shows the evolution of the radius of the shell as function of the time after the supernova explosion for the four different phases. The plot is taken from [Pad01].

10^{51} erg. The material is ejected in all directions and in most cases it forms an expanding shell. These objects are called shell-type supernova remnants. In some cases the supernova remnant is filled with and powered by the outflow of a pulsar, a fast spinning neutron star. These supernova remnants, called plerions, show up as synchrotron nebulae. Further on, there are composite remnants, a composition of the latter two. In this work, only shell-type supernova remnants are important.

3.2 Evolution of Shell-Type Supernova Remnants

After the explosion of the star, the material of its outer layers is ejected and expands into the surrounding interstellar medium. A short description of the evolution of the remnant can be found in **(author?)** [Lon94, sec. 19.4]; detailed calculations are laid out in [Pad01, chap. 4.9]. The expansion of the remnant can be divided into four phases. The evolution of the radius of the shell with the time after the supernova explosion is shown for these four different phases in Fig. 3.1.

From the kinetic energy of the supernova ($E_{\mathrm{kin}} \sim 10^{51}\,\mathrm{erg}$) and the ejected mass M_{eject} one can estimate the velocity at which the mass is ejected to be

$$\begin{aligned} v_{\mathrm{eject}} &= \sqrt{\frac{2E_{\mathrm{kin}}}{M_{\mathrm{eject}}}} \\ &\approx 10^4 \left(\frac{E_{\mathrm{kin}}}{10^{51}\,\mathrm{erg}}\right)^{\frac{1}{2}} \left(\frac{M_{\mathrm{eject}}}{M_\odot}\right)^{-\frac{1}{2}} . \end{aligned}$$

In the first phase the remnant expands undecelerated, and this phase is hence called free expansion phase. The radius of the shell rises proportional with time, $r \propto t$. The velocity is much higher than the speed of sound in the interstellar medium ($\approx 10 - 100\,\mathrm{km\,s^{-1}}$) [1]. The supersonic movement of the ejected material into the interstellar medium leads to the formation of a shock front. This shock front travels through the interstellar material. The formation and the properties of a shock front are discussed in section 3.3.

This phase ends when the mass $M_{\mathrm{swept-up}}$ of the swept up material becomes equal to the ejected mass, which happens at a radius of the remnant r_{f} defined by

$$M_{\mathrm{eject}} = M_{\mathrm{swept-up}} = \frac{4\pi}{3}\rho_{\mathrm{ISM}} r_{\mathrm{f}}^3,$$

where ρ_{ISM} is the mass density of the interstellar material. Thus, the radius of the remnant at the end of the free expansion phase is

$$r_{\mathrm{f}} \approx 2 \left(\frac{M_{\mathrm{eject}}}{M_\odot}\right)^{\frac{1}{3}} \left(\frac{\rho_{\mathrm{ISM}}}{2\times 10^{-24}\,\mathrm{g\,cm^{-3}}}\right)^{-\frac{1}{3}} \mathrm{pc}$$

and the corresponding time is

$$t_{\mathrm{f}} \approx 270 \left(\frac{M_{\mathrm{eject}}}{M_\odot}\right)^{\frac{5}{6}} \left(\frac{\rho_{\mathrm{ISM}}}{2\times 10^{-24}\,\mathrm{g\,cm^{-3}}}\right)^{-\frac{1}{3}} \left(\frac{E_{\mathrm{kin}}}{10^{51}\,\mathrm{erg}}\right)^{-\frac{1}{2}} \mathrm{y}.$$

In the next phase the expansion slows down and the radius of the remnant grows only as

$$r \propto t^{\frac{2}{5}}.$$

This is the so-called Sedov solution for strong explosions [see Pad00, sec. 8.12], and this phase is called Sedov phase. The outer layers of the ejected material slow down first and the following material catches up. Thus, the density in

---

[1] It should be noted that the magnetic field must be taken into account. In case of a magnetically dominated plasma, perturbations travel at the Alfvén velocity. The speed of the supernova ejecta is certainly “super-Alvénic”.

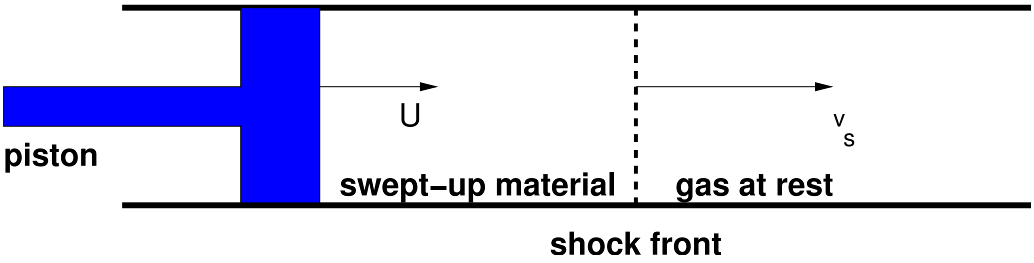

Figure 3.2: **Supersonic piston.** The piston with the supersonic velocity U creates a shock front. The shock front propagates ahead of the piston with a velocity $v_s > U$.

the outer layer increases. When the flow of material into the outer layers becomes supersonic a shock front forms on the inner edge of the compressed outer layers. This shock front heats up strongly the outer layers. This phase lasts approximately 10^4 years and the remnant reaches a radius of roughly 20 pc.

The first two phases are important for this work as a strong shock front travels through the interstellar material. The turbulent motion of the plasma near the shell creates a turbulent magnetic field. This field can reflect charged particles and confine them near the shock front. In the next sections will be shown how these particles can be accelerated.

The remnant further expands and cools down. The third phase begins when the temperature drops below 10^6 K. Heavy ions in the remnant, mainly carbon, nitrogen and oxygen, capture electrons and cool down by radiating photons. This radiative cooling dominates the energy loss of the remnant in this phase, and the phase is thus called radiative phase or snow plough phase because the shell piles up interstellar material like a snow plough.

Finally, after approximately 10^5 years, the speed of the shell becomes subsonic. The material of the remnant merges with the interstellar material and the supernova remnant loses its identity.

3.3 Shock Fronts

The ejected material of the supernova remnant expands supersonically into the interstellar material and sweeps up the ambient material. Between the swept-up material and the interstellar gas forms a shock front.

A very simple model illustrating a basic shock front is the supersonic piston which is shown in Fig. 3.2. A piston moves at the velocity U into the

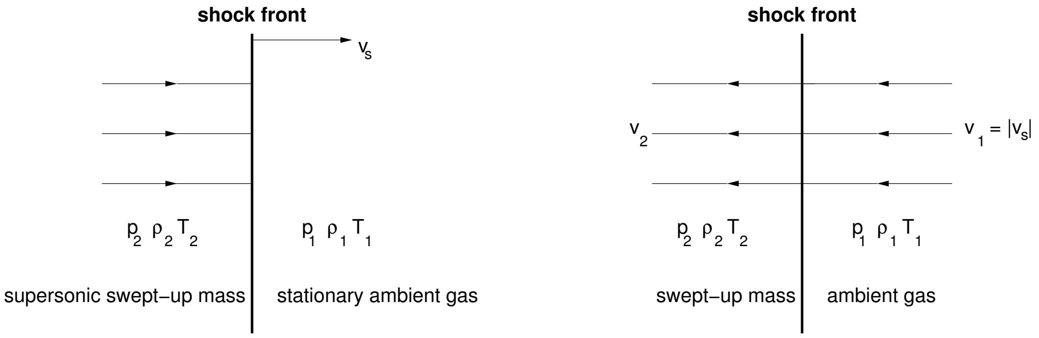

Figure 3.3: **Illustration of a shock front.** The left panel shows the system in the reference frame of the ambient gas. The shock front travels with a velocity v_s. The right panel shows the same situation in the reference frame of the moving shock.

stationary gas. The material in front of the piston is swept up. The velocity of the piston and the swept-up material is higher than the speed of sound c_s in the ambient medium, $U > c_\mathrm{s}$. Perturbations in gases move at the speed of sound, therefore the stationary gas has no information of the approaching disturbance. The swept-up material and the ambient gas which is at rest are divided by a discontinuity — the shock wave or shock front. More and more material passes through the shock front and is swept up. Thus, the shock front has to propagate with a velocity v_s which is faster than U.

Now, the basic properties of a shock wave are worked out. These calculations follow the explanations of **(author?)** [Lon92, section 10.6.1]. The ambient gas in front of the shock is at rest, having a pressure p_1, a mass density ρ_1 and a temperature T_1. Behind the shock wave is the swept-up material with pressure, mass density and temperature p_2, ρ_2 and T_2, respectively. This is illustrated in the left panel of Fig. 3.3. It is convenient to make all calculations in the reference frame of the moving shock front. This is shown in the right panel of Fig. 3.3. The shock is at rest, and it is approached by the ambient gas with a velocity of $v_1 = |v_\mathrm{s}|$. The ambient gas passes the shock front and is swept-up, and it departs the shock front with a velocity v_2.

Some useful equations can be derived from conservation laws of the material passing the shock front. First of all, the mass passing through the front is conserved and a mass flux per unit area j can be defined:

$$j = \rho_1 v_1 = \rho_2 v_2. \tag{3.1}$$

The energy flux passing through the shock front is also conserved. For plane shocks, which are perpendicular to v_1 and v_2, this relation can be written as

$$\rho_1 v_1 \left(\frac{1}{2}v_1^2 + w_1\right) = \rho_2 v_2 \left(\frac{1}{2}v_2^2 + w_2\right). \tag{3.2}$$

The enthalpy w of the gas considers the work which is done on the gas as it passes through the shock front. For a perfect gas the enthalpy is $w = \kappa p V/(\kappa - 1)$ where κ is the adiabatic coefficient and $V = \rho^{-1}$ is the specific volume. Finally, the momentum flux through the shock front is conserved. For a plane and perpendicular shock this can be written as

$$p_1 + \rho_1 v_1^2 = p_2 + \rho_2 v_2^2. \tag{3.3}$$

The equations (3.1), (3.2) and (3.3) are the shock conditions.

Using equations (3.1) and (3.3), the squared mass flux is

$$j^2 = \frac{p_2 - p_1}{V_1 - V_2}. \tag{3.4}$$

From equation (3.4) and the conservation of mass (eq. 3.1) the velocity difference can be calculated as

$$v_1 - v_2 = \sqrt{(p_2 - p_1)(V_1 - V_2)}.$$

Using the conservation of the energy flux (eq. 3.2) and the equation for the mass flux (eq. 3.4), the ratio of the specific volumes for a perfect gas is

$$\frac{V_2}{V_1} = \frac{p_1(\kappa + 1) + p_2(\kappa - 1)}{p_1(\kappa - 1) + p_2(\kappa + 1)}. \tag{3.5}$$

Now, V_2 in equation (3.4) can be eliminated and the velocity in front of the shock is found to be

$$v_1^2 = j^2 V_1^2 = \frac{V_1}{2}\left[(\kappa - 1)p_1 + (\kappa + 1)p_2\right]. \tag{3.6}$$

The ratio of the velocities is simply

$$\frac{v_1}{v_2} = \frac{\rho_2 j}{\rho_1 j} = \frac{V_1}{V_2}.$$

Using the perfect gas law, $p_1 V_1/T_1 = p_2 V_2/T_2$, the ratio of the temperatures ahead and behind the shock can be calculated using equation (3.5) as

$$\frac{T_2}{T_1} = \frac{p_2 V_2}{p_1 V_1} = \frac{p_2\left[p_1(\kappa + 1) + p_2(\kappa - 1)\right]}{p_1\left[p_1(\kappa - 1) + p_2(\kappa - 1)\right]}.$$

It is convenient to write the velocity v_1 of the gas ahead of the shock front in units of the speed of sound in the medium, which is $c_1 = \sqrt{\kappa p_1/\rho_1}$:

$$M_1 = v_1/c_1. \tag{3.7}$$

M is called the Mach number. Using equation (3.6), the Mach number can be expressed as

$$M_1^2 = \frac{v_1^2 \rho_1}{\kappa p_1} = \frac{v_1^2}{\kappa p_1 V_1} = \frac{1}{2\kappa p_1}\left[(\kappa-1)p_1 + (\kappa+1)p_2\right].$$

The ratio of the pressures is then

$$\frac{p_2}{p_1} = \frac{2\kappa M_1^2 - (\kappa-1)}{\kappa+1}$$

and the ratio of the specific volumes is

$$\frac{V_1}{V_2} = \frac{\kappa+1}{\kappa - 1 + 2/M_1^2}.$$

Assuming very strong shocks, $M_1 \gg 1$, the equations for the temperature and velocity ratios can be simplified to be

$$\begin{aligned} \frac{v_1}{v_2} &= \frac{\kappa+1}{\kappa-1}, \\ \frac{T_2}{T_1} &= \frac{2\kappa(\kappa-1)}{(\kappa+1)^2} M_1^2. \end{aligned}$$

The interstellar material consist mainly of atomic hydrogen. Therefore the ambient gas can be assumed to have the adiabatic coefficient of monatomic gases, $\kappa = 5/3$. For the velocity and temperature ratios the simple results

$$\begin{aligned} \frac{v_1}{v_2} &= 4, && (3.8) \\ \frac{T_2}{T_1} &= \frac{5}{16} M_1^2 && (3.9) \\ \frac{p_2}{p_1} &= \frac{5}{4} M_1^2 && (3.10) \end{aligned}$$

are obtained. It can be seen from equations (3.9) and (3.10) that the material, which passes through the shock front, is heated and compressed. The heating and compression depends on the squared Mach number M_1 and thus on the

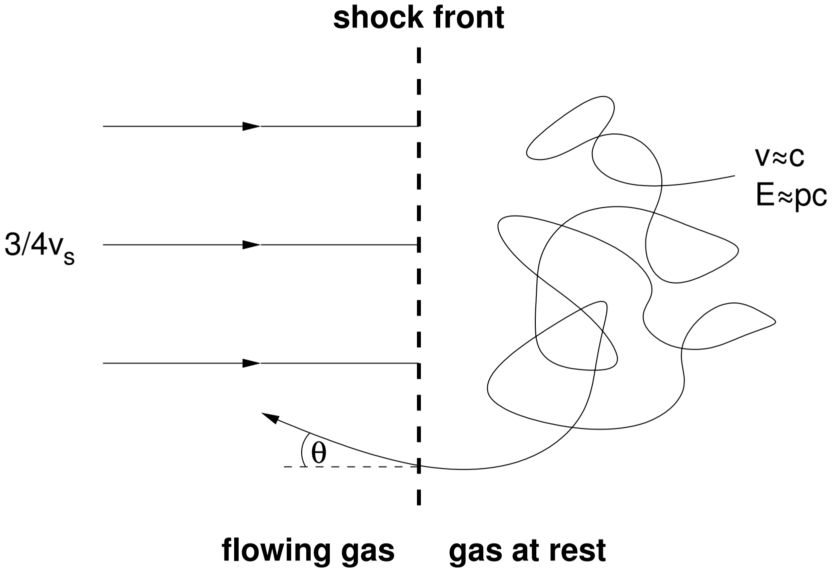

Figure 3.4: **Shock acceleration.** A particle of velocity $v \approx c$ and energy $E \approx pc$ is located in the gas at rest. It crosses the shock front into the flowing gas with velocity $3/4 v_\mathrm{s}$ and gains a Lorentz boost.

velocity of the shock front. The difference $v_1 - v_2$ between the velocities of the gas in front and behind the shock front is U, the velocity of the piston. From equation (3.8) follows that the velocity of the shock front is simply

$$v_\mathrm{s} = |v_1| = \frac{4}{3}U. \tag{3.11}$$

Interestingly, the velocity of the shock front depends only on the velocity of the piston and not on any parameter of the material, like temperature or density.

3.4 Particle Acceleration in Shock Fronts

Besides the heating and compressing of the ambient material, the shock front can also accelerate particles. Based on the characteristics of the shock front, it can be shown that the energy spectrum of the accelerated particles follow a power law with a fixed power law index. These calculations are presented in this section, following the work presented in **(author?)** [Lon94, sec. 21.4].

From equations (3.8) and (3.11) can be seen that the difference between the plasma velocities ahead and behind the shock front is 3/4 of the velocity of the shock front, v_{s}:

$$\Delta v = \frac{3}{4} v_{\mathrm{s}}.$$

A particle in the ambient gas can cross the shock front, and it enters the shocked material behind the shock front. The shocked material travels at the velocity $3/4 v_{\mathrm{s}}$. This is illustrated in Fig. 3.4. In its rest frame, the ambient gas is approached by the shocked gas with the velocity $3/4 v_{\mathrm{s}}$. When a particle crosses the shock front it gains a Lorentz boost with the velocity $3/4 v_{\mathrm{s}}$. A particle in the shocked gas can also pass the shock front into the unshocked gas. In the rest frame of the shocked gas the ambient gas appears to be approaching the shocked gas with the same velocity $3/4 v_{\mathrm{s}}$ and the particle again gains a Lorentz boost. A particle gains the same Lorentz boost in both directions of crossing the shock front.

Now the energy gain of a particle in one shock front crossing will be worked out. The particle is assumed to have a velocity near the speed of light, $v \approx c$, and an energy $E \approx pc$. It crosses the shock front at an angle θ (see Fig.3.4). The particle's energy in the rest frame at the other side of the shock front is

$$E' = \gamma \left(E + \beta c p_{||} \right)$$

where $p_{||} = p \cos\theta$ is the component of the momentum parallel to the movement of the shock front. The difference of the velocities ahead and behind the shock is non-relativistic , $\beta = 3/4 v_{\mathrm{s}} \ll 1$, and thus $\gamma = 1/\sqrt{1-\beta^2} \approx 1$. The energy gain is then simply

$$\Delta E = E' - E = \frac{3}{4} v_{\mathrm{s}} p \cos\theta.$$

Obviously, the energy gain depends on the crossing angle θ. As the particles are isotropically distributed, they can cross the shock front at any angle. The mean energy gain per crossing can be calculated from the integral over all crossing angles:

$$< \Delta E >= \int\limits_0^1 \Delta E(\cos\theta) P(\cos\theta) \mathrm{d}\cos\theta.$$

Here, $P(\cos\theta)$ is the probability that a particle crosses the shock front at an angle θ. The crossing probability depends on the rate of the particles hitting the shock front. The rate is proportional to the velocity parallel to the movement of the shock, $P(\cos\theta) \propto c \cos\theta$, and depends on the angular distribution. The particles are isotropic in the angle θ and thus the angle distribution is constant in $\mathrm{d}\cos\theta$. Finally, the crossing probability $P(\cos\theta) \propto c\cos\theta$ has to be normalised to 1:

$$\int\limits_0^1 P(\theta)\mathrm{d}\cos\theta \overset{!}{=} 1 \rightarrow P(\theta) = 2\cos\theta.$$

The mean energy gain can then be calculated to be

$$< \Delta E >= \int\limits_0^1 \frac{3}{4}v_\mathrm{s}2p\cos^2\theta\mathrm{d}\cos\theta = \frac{1}{2}v_\mathrm{s}p \approx \frac{1}{2}\frac{v_\mathrm{s}}{c}E.$$

At either side of the shock the particle is scattered and the velocity distribution becomes isotropic. The particle can again cross the shock front. Within one reflection, i.e. the particle crosses the shock front back and forth, the mean energy gain is

$$\left\langle\frac{\Delta E}{E}\right\rangle = \frac{v_\mathrm{s}}{c}.$$

The energy gain is in the first order of v_s.

Now the energy spectrum of the accelerated particles will be calculated. After k crossings, a particle with the initial energy E_0 has the energy

$$E_k = E_0\left(1+\left\langle\frac{\Delta E}{E}\right\rangle\right)^k = E_0\xi^k \tag{3.12}$$

with

$$\xi = 1 + v_\mathrm{s}/c. \tag{3.13}$$

The gas behind the shock moves away from the shock with a velocity $v_\mathrm{s}/4$. The loss rate of the particles in a region close to the shock front is

$$\left(\frac{\mathrm{d}N}{\mathrm{d}A\mathrm{d}t}\right)_\mathrm{loss} = nv_\mathrm{s}/4,$$

where n is the particle density and A the area through which the particles are lost. The rate at which the particles cross through an area A of the the shock front is

$$\left(\frac{\mathrm{d}N}{\mathrm{d}A\mathrm{d}t}\right)_\mathrm{cross} = \frac{1}{2}\int\limits_0^1 \mathrm{d}\cos\theta nc\cos\theta = \frac{cn}{4}.$$

The probability that a particle remains in the region of the shock for further crossings is

$$P = 1 - \left(\frac{\mathrm{d}N}{\mathrm{d}A\mathrm{d}t}\right)_\mathrm{loss} / \left(\frac{\mathrm{d}N}{\mathrm{d}A\mathrm{d}t}\right)_\mathrm{cross} = 1 - \frac{v_\mathrm{s}}{c}. \tag{3.14}$$

From N_0 particles, which are initially located in the volume around the shock front, N_k particles remain there after k crossings,

$$N_k = N_0 P^k. \tag{3.15}$$

From equations (3.12) and (3.15) one can calculate via

$$\frac{\ln N/N_0}{\ln E/E_0} = \frac{\ln P}{\ln \xi}$$

the energy spectrum, which is

$$\frac{\mathrm{d}N}{\mathrm{d}E} \propto E^{\left(\frac{\ln P}{\ln \xi} - 1\right)}.$$

With equations (3.13) and (3.14) and the approximation $\ln(1 \pm x) \approx \pm x$ one can immediately see that

$$\frac{\mathrm{d}N}{\mathrm{d}E} \propto E^{-2}. \tag{3.16}$$

The energy spectrum does not depend on the velocity. The assumption was made that the particle is highly relativistic, but the final energy spectrum does not depend on the exact energy distribution of the particles before the acceleration process. From very basic assumptions, a power law with a spectral index of 2 could be derived.

3.5 Diffusive Shock Acceleration

The calculations presented in the previous sections were made using solely thermodynamic arguments. The situation in the shells of supernova remnants is somewhat different. The ambient interstellar material has a very low density, and therefore a particle can hardly be confined in the shock region by scattering at the particles of the interstellar gas. Additionally, the magnetic field was neglected. In fact, the magnetic field in the shell region dominates the interaction of the particles. Thus, one has to use the speed of hydrodynamic waves, which is the Alfvén speed $c_\mathrm{A} = B/\sqrt{\mu_0 \rho}$, rather than the thermodynamic sound speed c_s in equation (3.7). This will lead to modifications of the equations (3.8–3.10).

The magnetic field is also responsible for scattering the particles at either side of the shock front. **(author?)** [Fer49] suggested an acceleration of charged cosmic particles by the reflection between moving magnetic mirrors. The energy gain is only proportional to the second–order of the mirror velocity, the process is therefore called second order Fermi acceleration.

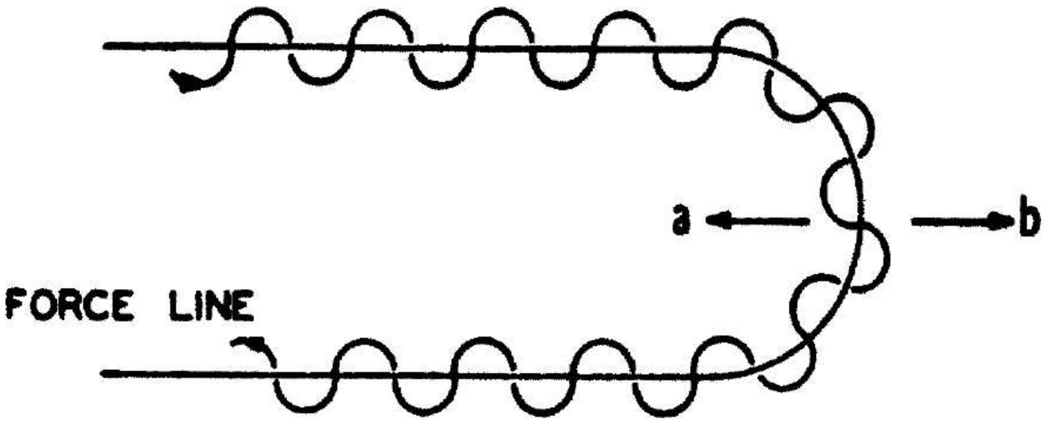

Figure 3.5: **Magnetic mirror.** A charged particle travels along a bended magnetic field line and is reflected. The picture is taken from [Fer49].

This mechanism is not sufficiently effective to explain the acceleration of cosmic rays. However, the mechanism of reflection of the charged particles at the magnetic mirrors is important for the acceleration of particles in shock fronts. Figure 3.5 from the original work of Fermi illustrates this reflection. The charged particle travels along a bended magnetic field line and changes its direction. By scattering on the turbulent magnetic field at both sides of the shock front, the velocity distribution of the particles becomes isotropic. As the energy gain in shock acceleration is proportional to the first–order of the shock front velocity (eq. 3.4), this process is also called first order Fermi acceleration. Because the particles diffuse through the shock front and are accelerated in the shock front, this process is also called Diffusive Shock Acceleration.

In the last section the assumption was made that the particles already have relativistic energies. The injection of non-relativistic particles must be considered for a proper calculation of the spectrum of the accelerated particles.

The consideration of the effect of the magnetic field, the injection of the source particles and other parameters leads to slight modifications of the spectral index. Reviews of detailed calculations of the Diffusive Shock Acceleration are given by**(author?)** [JE91] and **(author?)** [MD01].

3.6 Gamma Ray Production in Supernova Remnants

As the accelerated charged particles are deflected in the interstellar magnetic field, they do not carry any information about their origin when they arrive at Earth. A good tool to investigate the acceleration process are γ-rays which are emitted by the accelerated particles.

3.6.1 Hadron Interaction with the Interstellar Material

The interstellar space is filled with a thin gas consisting mostly of hydrogen with a number density in the order of 1 particle per cm^3. Hadrons, accelerated in the supernova remnant, can interact strongly with the nuclei of these hydrogen atoms. As the cosmic rays consist mainly of protons, only the interaction of protons will be discussed in this work. In strong, inelastic interactions of two protons new particles will be generated. The products of these reactions are primarily the lightest mesons, π^+, π^- and π^0. While charged pions decay into leptons, the neutral pions decay after a very short live time of $\approx 10^{-16}\,\mathrm{s}$ into two photons. These photons are a good tracer for the acceleration of protons in the shock front. In the following, some approximations of the hadronic interactions will be laid out. These approximations are used in the discussion in chapter 6.

The interaction rate of the proton–proton interactions is determined by the cross-section σ_{pp}. Based on Regge theory, **(author?)** [EHO$^+$04] give a parameterisation of the total inelastic cross-section:

$$\begin{aligned}\sigma_{pp}^{\mathrm{PDG}}(s) &= \Bigg[35.45 + 0.308 \times \ln^2\left(\frac{s}{(5.38\,\mathrm{GeV})^2}\right) + \\ &\qquad 42.53\left(\frac{1\,\mathrm{GeV}^2}{s}\right)^{0.458} - 33.34\left(\frac{1\,\mathrm{GeV}^2}{s}\right)^{0.545}\Bigg]\ \mathrm{mb},\end{aligned}$$

with $s = 2(E_{\mathrm{kin}} + m_p)m_p$ being the squared centre-of-mass energy. The accelerated proton has the kinetic energy E_{kin} and the proton of the interstellar medium is assumed to be at rest. The proton rest mass is given by $m_p \approx 1\,\mathrm{GeV}$. The cross-section is given in units of millibarn ($1\,\mathrm{b} = 10^{-28}\,\mathrm{m}^2$). An approximation is used by **(author?)** [AA00]:

$$\sigma_{pp}^{\mathrm{AA}}(E_{\mathrm{kin}}) \approx 30\left(0.95 + 0.06\ln\frac{E_{\mathrm{kin}}}{1\,\mathrm{GeV}}\right)\ \mathrm{mb}.$$

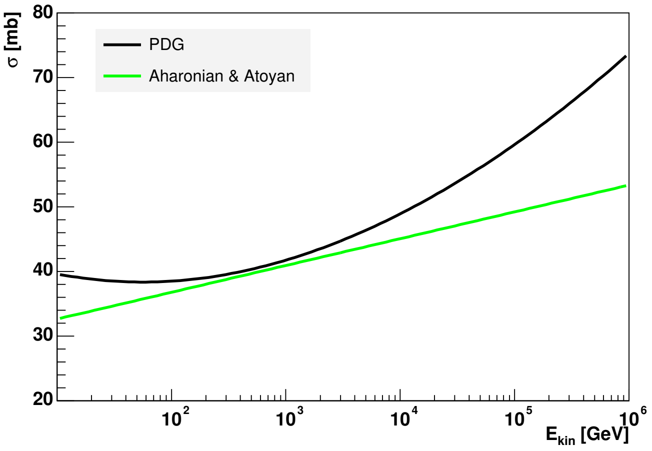

Figure 3.6: **Total $p-p$ cross-section.** Shown are the approximations of the Particle Data Group (PDG, [EHO$^+$04]) and used by **(author?)** [AA00].

Figure 3.6 shows the cross-sections for kinetic energies of the accelerated protons in the range between 10 GeV and 1000 TeV. It can be seen that the cross-section rises only gradually (approximately logarithmically) with the energy. The proton energy is unknown, therefore the cross-section will be assumed to be constant. In the region between 100 GeV and 10^5 GeV it is reasonable to assume a value of

$$\sigma_{pp} \approx 50\,\mathrm{mb}.$$

Now, the attention is drawn on the energy loss of the protons in the interstellar gas with a number density of $n \approx 1\,\mathrm{cm}^{-3}$ protons. The interaction rate of a proton population travelling almost at the speed of light is given by

$$n\sigma_{pp}c.$$

It will be assumed that, on average, protons transfer 1/2 of their energy into pions. Additionally, the assumption is made that almost all interactions result in pion production, and that 1/3 of the pions are π^0's. Thus, with a scaling factor $f \approx 1/6$ incorporating the latter assumptions, one can define a cooling time [see e.g. Aha04]

$$\tau_{\pi^0} = \frac{1}{n\sigma_{pp}cf} \approx 4 \times 10^{15} \left(\frac{n}{1\,\mathrm{cm}^{-3}}\right)^{-1} \mathrm{s}.$$

The mean energy loss of a proton with energy E in the $pp \rightarrow \pi^0 + X$ channel is $< \mathrm{d}E/\mathrm{d}t >= E/\tau_{\pi^0}$. In reactions with interstellar matter ($n \approx 1\,\mathrm{cm}^{-3}$) a proton of energy E loses, on average, a fraction 2.5×10^{-16} of its energy

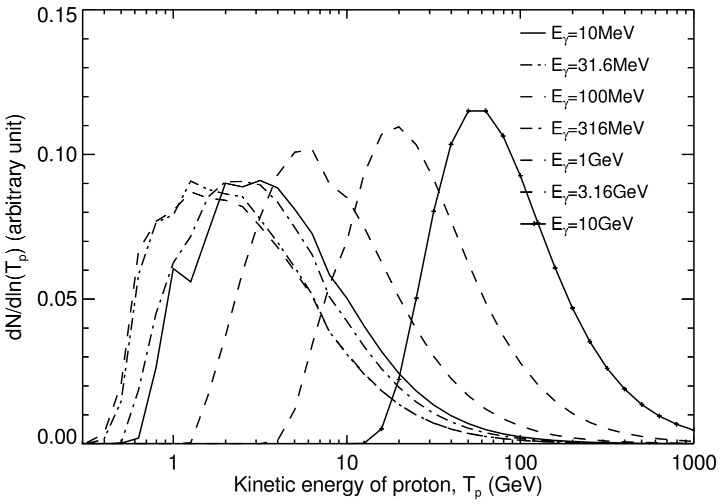

Figure 3.7: **Photon energies from $p-p$ interactions.** The plot of **(author?)** [Mor97] shows the contribution of protons of kinetic energy T_p to photons of certain energies as inferred from Monte Carlo simulations.

per second through the π^0 channel. The cooling time is independent of the energy. For an initial proton spectrum following a power law the cooling will not change the spectral index.

As already pointed out above, the π^0 almost immediately decays into two photons. The energy spectrum of the photons produced in hadronic interactions cannot be calculated in a straight-forward way. **(author?)** [Mor97] and **(author?)** [Der86] performed detailed Monte Carlo studies of the interaction $pp \to \pi^0 + X \to \gamma\gamma + X$. These simulations were compared with data measured at accelerator experiments. Figure 3.7 shows one of the results obtained by **(author?)** [Mor97]. It can be seen that a proton with a kinetic energy of 100 GeV produces mainly photons with energies of about 10 GeV. Vice versa it can be said that photons with energies of 10 GeV are produced by protons with energies between 10 GeV and 1000 GeV, but mostly by protons with energies around 100 GeV. The same ratio of ≈10:1 can be seen for other energies. For the rough interpretation carried out in this work it will be assumed that a proton of energy E loses its energy to photons of energy $0.1E$. **(author?)** [AA00] adopt a mean fraction of 0.17 of the kinetic energy of the proton to be transferred to the π^0 and thus the produced photons have a mean energy of $0.085E$.

In this work only photons of energies between ≈ 500 GeV and ≈ 10 TeV are of interest. Using the approximations laid out above, the following conclusions can be drawn concerning the photons produced in proton interactions with the interstellar material.

- γ-ray radiation in the energy range between 500 GeV and 10 TeV is produced by protons with energies between ≈ 5 TeV and ≈ 100 TeV.

- The radiation mechanism is almost independent of the proton energy. Thus, the proton spectrum remains unchanged. The energy of the radiated photons is connected linearly to the proton energy. Thus, the shape of the γ-ray energy spectrum reflects the shape of the initial proton spectrum.

- The energy loss of the protons is transferred to photons. From the total energy in protons, W_p, one can calculate the integral energy flux of photons, the luminosity L_γ. The luminosity is given by

$$\begin{aligned} L_\gamma(0.5 - 10\,\mathrm{TeV}) &= \frac{W_p(5 - 100\,\mathrm{TeV})}{\tau_{\pi^0}} \qquad (3.17) \\ &= 2.5 \times 10^{-16} \left(\frac{n}{1\,\mathrm{cm}^{-3}}\right) \times W_p(5 - 100\,\mathrm{TeV})\,\mathrm{s}^{-1}. \end{aligned}$$

  This equation will be used in the discussion in chapter 6.

3.6.2 Gamma-Ray Production by Electrons

Accelerated electrons lose their energy due to various processes. These processes are bremsstrahlung in the interstellar material, synchrotron radiation in a magnetic field and inverse Compton scattering on interstellar photon fields. At the end of this section some useful relations are presented which are used in the interpretation of the observed γ-rays.

Bremsstrahlung

Free electrons interacting with the field of a nucleus can radiate photons. This process is called bremsstrahlung. The energy loss due to bremsstrahlung can be expressed using the radiation length X_0, defined as the area density over which a high-energy particle ($E \gg 1\,\mathrm{GeV}$) loses, on average, a fraction $1-e^{-1}$ (i.e. 63.2%) of its energy:

$$\left\langle -\frac{\mathrm{d}E}{\mathrm{d}x} \right\rangle_{\mathrm{br}} = \frac{E}{X_0}.$$

The radiation length depends on some parameters of the medium, mainly the charge of the nuclei. Here, bremsstrahlung in the interstellar medium is discussed which consists mainly of hydrogen. The radiation length in atomic hydrogen is given by **(author?)** [EHO$^+$04] to be $X_0 = 63.05\,\mathrm{g\,cm^{-2}}$. The mass density of the interstellar medium is $m_p n$, where m_p is the proton mass and n the number density of the interstellar material. A particle travelling at the speed of light c sees an area density of $cm_p n$ per time unit. Thus, the energy loss per time unit due to bremsstrahlung is

$$\left\langle -\frac{\mathrm{d}E}{\mathrm{d}t} \right\rangle_{\mathrm{br}} = \frac{cm_p n}{X_0} E.$$

The cooling time is then

$$\tau_{\mathrm{br}} = \frac{X_0}{cm_p n} \approx 10^{15} \left(\frac{n}{1\,\mathrm{cm}^{-3}} \right)^{-1} \mathrm{s}, \tag{3.18}$$

which is independent of the electron energy. Therefore, the shape of an initial power law spectrum remains unchanged.

A calculation of the energy spectrum of the bremsstrahlung photons can be found in **(author?)** [Lon92, sec. 3.6]. As the energy of the bremsstrahlung photons must be less than the initial electron energy E, $E_\gamma \leq E$, the upper edge of the bremsstrahlung spectrum is connected to the maximum energy of the electrons. The mean of the bremsstrahlung spectrum is at $\approx 1/3E$, where E is the electron energy.

Synchrotron Radiation

Charged particles travelling in a magnetic field are deflected by the Lorentz force. The case of a free electron travelling with the speed v in a magnetic field B is illustrated in Fig. 3.8. The angle α between the electron trajectory and the magnetic field lines is called pitch angle. Only the transverse velocity is affected by the Lorentz force and the electron is forced on a spiral movement around the magnetic field lines. Accelerated charged particles radiate photons. The radiation due to the spiral movement of a charged particle is called synchrotron radiation.

From the electric dipole radiation of an accelerated charged particle the energy loss of this particle and the resulting electromagnetic spectrum can be calculated [Lon94, chap. 18.1]. A detailed analysis of the synchrotron radiation was carried out by **(author?)** [GS65]. Here some useful results are presented and discussed for electrons.

The energy loss due to the synchrotron radiation is

$$-\frac{\mathrm{d}E}{\mathrm{d}t} = 2\sigma_{\mathrm{T}} c U_{\mathrm{mag}} \left(\frac{v}{c} \right)^2 \gamma^2 \sin^2 \alpha$$

where

$$\sigma_{\mathrm{T}} = \frac{e^4}{6\pi\epsilon_0^2 c^4 m_e^2} = 0.665\,\mathrm{b} \tag{3.19}$$

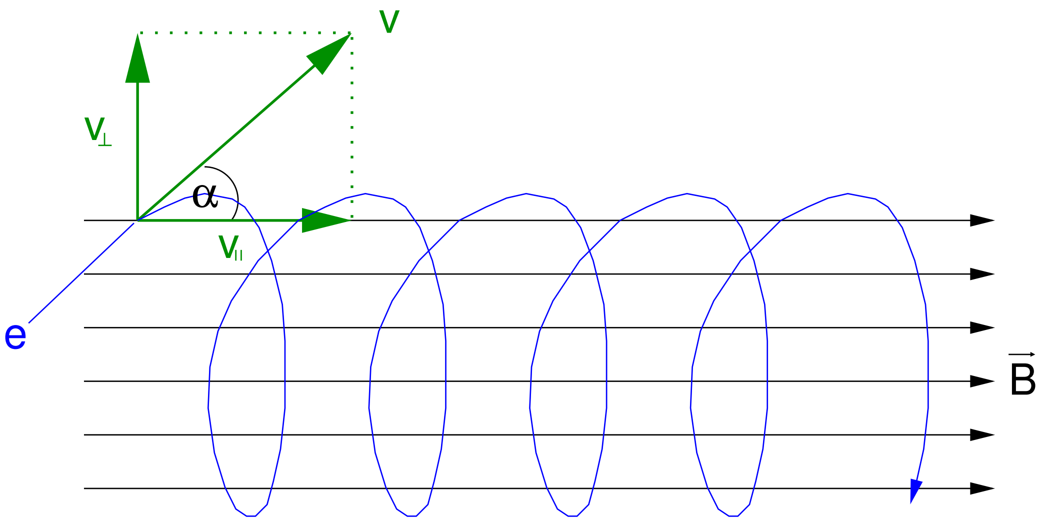

Figure 3.8: **Movement of an electron in a magnetic field.** The trajectory of an electron (blue line) in a magnetic field (black arrows) is shown. The Lorentz force causes the transverse velocity $v_\perp = v \sin\alpha$ to spin around B while the parallel velocity $v_\parallel$ remains constant.

is the Thomson cross-section, $U_{\mathrm{mag}} = B^2/(2\mu_0)$ is the energy density of the magnetic field, ϵ_0 is the permittivity of free space and μ_0 the permeability of free space. The particles move isotropically and the average over all possible pitch angles α leads to $< \sin^2\alpha >= 2/3$. Using $\beta = v/c$ the mean energy loss of the electrons is

$$\left\langle -\frac{\mathrm{d}E}{\mathrm{d}t} \right\rangle_{\mathrm{sy}} = \frac{4}{3}\sigma_{\mathrm{T}} c U_{\mathrm{mag}} \beta^2 \gamma^2. \tag{3.20}$$

Later in this work, magnetic fields in the order of $100\,\mu$G will be discussed. The energy density of the magnetic field can be calculated from the magnetic field in units of $100\,\mu$G using

$$U_{\mathrm{mag}} = \frac{B^2}{2\mu_0} = 250 \left(\frac{B}{100\,\mu\mathrm{G}}\right)^2 \mathrm{eV\,cm^{-3}}. \tag{3.21}$$

With the relations

$$\beta = \frac{pc}{E}, \tag{3.22}$$

$$\gamma = \frac{E}{m_e c^2} \tag{3.23}$$

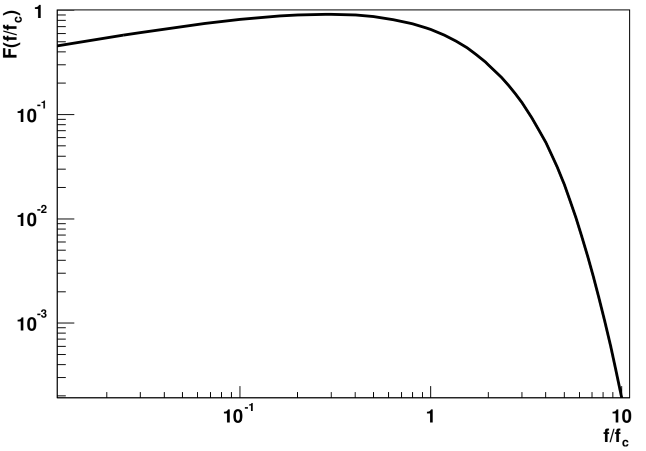

Figure 3.9: **Synchrotron spectrum.** Shown is the function $F(f/f_\mathrm{c})$ which defines the shape of the synchrotron spectrum.

the term $(\beta\gamma)^2$ can be written as

$$(\beta\gamma)^2 = \frac{p^2}{m_e^2 c^2}.$$

Due to the high kinetic energy of the electrons, the rest energy can be neglected, $E^2 = m_e^2 c^4 + p^2 c^2 \approx p^2 c^2$, resulting in

$$(\beta\gamma)^2 \approx \frac{E^2}{m_e^2 c^4}.$$

The cooling time due to synchrotron radiation can be calculated to be

$$\tau_\mathrm{sy}(E) = \frac{E}{\left\langle -\frac{\mathrm{d}E}{\mathrm{d}t} \right\rangle_\mathrm{sy}} = \frac{3 m_e^2 c^3}{4\sigma_\mathrm{T} U_\mathrm{mag} E} \approx 4 \times 10^{10} \left(\frac{B}{100\,\mu\mathrm{G}}\right)^{-2} \left(\frac{E}{1\,\mathrm{TeV}}\right)^{-1} \mathrm{s}. \tag{3.24}$$

The energy loss of the electrons depends on the magnetic field strength B and on the energy E of the electrons. The cooling is more effective at higher energies. Therefore, synchrotron radiation results in a steepening of the electron spectrum.

The power spectrum of the synchrotron radiation of an electron over the radiated frequency f is given by the equation

$$\frac{\mathrm{d}E}{\mathrm{d}t\mathrm{d}f} = \frac{\sqrt{3} e^3 B \sin\alpha}{4\pi\epsilon_0 c m_e} F\left(\frac{f}{f_\mathrm{c}}\right).$$

Here,

$$f_\mathrm{c} = \frac{3}{2}\gamma^2 \frac{eB}{2\pi m_e} \sin\alpha$$

is the characteristic frequency. The shape of the distribution is given by the function

$$F(x) = x \int_x^\infty K_{5/3}(z) \mathrm{d}z$$

where $K_{5/3}(z)$ is a modified Bessel function. Tabulated values of $F(x)$ can be found in [Lon94, Table 18.1]. The function $F(f/f_\mathrm{c})$ is shown in Fig. 3.9. It can be seen that the spectrum is very broad and has a sharp edge beyond f_c. Therefore, f_c is also called cut-off frequency.

The maximum of the frequency distribution is at $f_\mathrm{sy} = 0.29 f_\mathrm{c}$ [see e.g. GS65]:

$$f_\mathrm{sy} = 0.29 f_\mathrm{c} \approx \frac{1}{3}\sqrt{\frac{3}{2}}\gamma^2 \frac{eB}{2\pi m_e}. \tag{3.25}$$

Using this and equation (3.23) one can calculate the typical energy of the synchrotron photons:

$$E_\mathrm{sy} = h f_\mathrm{sy} = 2 \left(\frac{B}{100\,\mu\mathrm{G}}\right)\left(\frac{E}{1\,\mathrm{TeV}}\right)^2 \mathrm{eV}, \tag{3.26}$$

where E is the energy of the electron [see also AAK97, eq. (3)]. The typical energy depends on the magnetic field B and the square of the energy E of the electron. Thus, the synchrotron spectrum provides information of the product BE_max^2, where E_max^2 is the maximum energy of the electron spectrum.

An independent measurement of the product $B^2 E_\mathrm{max}$ can be gained from the width of the synchrotron emission region [see e.g. VBK05, BYH05]. Roughly, the width w of the emission region represents the distance an electron travels before it lost its energy due to synchrotron radiation. Assuming that the electron is confined in the shock region, the width depends on the shock speed v_s and the synchrotron cooling time τ_sy (eq. 3.24):

$$w \propto v_s \tau_\mathrm{sy} \propto v_s \left(\frac{B}{100\,\mu\mathrm{G}}\right)^{-2}\left(\frac{E}{1\,\mathrm{TeV}}\right)^{-1}. \tag{3.27}$$

The width of the emission region can be calculated from the observed angular width and the distance to the supernova remnant. As additional parameter the speed of the shock front is needed. It should be noted that the calculation of the magnetic field is not straight-forward as equation (3.27) suggests. It further depends on the magnetic field ahead of the shock and the compression ratio in the shock. Recently, **(author?)** [KBV05] discussed this calculation for the supernova remnant SN 1006.

Inverse Compton Scattering

The Compton scattering process is the interaction of a high energy photon with a free electron. The photon transfers energy and momentum to the electron, and the electron is boosted up to higher energies.

Free electrons of high energies, e.g. those accelerated in a shock front, can interact with low energy photons via the inverse Compton (IC) effect. Target photons in astrophysical processes are the photons of the cosmic microwave background (CMB), infrared background and star light. In this process, the high energy electron hits a photon and transfers energy and momentum to the photon. The photons can be boosted up to very high energies.

This process is determined by the Klein-Nishina cross-section [see e.g. Lon92, sec. 4.3.2]. When, in the centre of momentum frame, the energy of the photon hf is low compared to the rest energy of the electrons,

$$\epsilon = \frac{hf}{m_e c^2} \ll 1, \tag{3.28}$$

the Klein-Nishina cross-section can be approximated by the Thomson cross-section σ_T (eq. 3.19), and thus this regime is called the Thomson limit. For high energy photons, $\epsilon \gtrsim 1$, the full Klein-Nishina cross-section has to be used, which decreases with the photon energy.

For highly relativistic electrons, which will be considered here, the centre of momentum frame moves almost with the speed of the electron and the energy of the photon in the centre of momentum frame is γhf. With the relativistic factor of the electron $\gamma = E/m_e c^2$ equation (3.28) can be written as

$$\epsilon = \frac{Ehf}{m_e^2 c^4} \ll 1, \tag{3.29}$$

where E is the electron energy.

The cosmic microwave background is isotropic in the universe and its temperature is well known to be thermal radiation with a temperature of $T = 2.7\,\mathrm{K}$. Therefore, the inverse Compton scattering of electrons on this photon field can easily be calculated. The frequency f_0 of the maximum of the frequency distribution of thermal black-body radiation is, according to Wien's law, at

$$f_0 = \frac{cT}{b}$$

with $b = 2.9 \times 10^{-3}\,\mathrm{m\,K} = 1.5 \times 10^4\,\mathrm{K/eV}$ being Wien's constant and c is the speed of light. The maximum of the frequency distribution of the cosmic microwave background is

$$f_0 = 1.8 \times 10^{-4}\,\mathrm{eV}. \tag{3.30}$$

Thus, the energy at f_0 is $hf_0 = 1.1 \times 10^{-3}\,\mathrm{eV}$, and the use of the Thomson limit is justified for electron energies up to several tens of TeV.

Other photon fields, like infrared background and star light, are not isotropic, and therefore the estimation of their energy densities needs further assumptions. However, these photon energies are in the Klein-Nishina regime and therefore inverse Compton scattering on these photons is suppressed.

The calculation of the energy loss due to inverse Compton scattering can be found in **(author?)** [Lon92, sec. 4.3.3]. The energy loss is found to be

$$\left\langle -\frac{\mathrm{d}E}{\mathrm{d}t} \right\rangle_{\mathrm{IC}} = \frac{4}{3}\sigma_{\mathrm{T}} c U_{\mathrm{rad}} \beta^2 \gamma^2 .$$

This is very similar to the energy loss due to synchrotron radiation (eq. 3.20) and a cooling time

$$\tau_{\mathrm{IC}}(E) = \frac{3 m_e^2 c^3}{4 \sigma_{\mathrm{T}} U_{\mathrm{rad}} E} \tag{3.31}$$

can be calculated. The energy loss due to inverse Compton scattering depends on the energy density U_{rad} of the radiation field and on the electron energy E.

The energy density of the cosmic microwave background can be calculated to be

$$U_{\mathrm{CMB}} = 0.25\,\mathrm{eV\,cm^{-3}} \tag{3.32}$$

and the cooling time due to inverse Compton scattering on the cosmic microwave background is

$$\tau_{\mathrm{IC}}(E) \approx 4 \times 10^{13} \left(\frac{E}{\mathrm{TeV}}\right)^{-1} \mathrm{s}. \tag{3.33}$$

The spectrum of the inverse Compton photons is calculated in [Lon92, 4.3.3]. It has its maximum at

$$f_{\mathrm{max}} = 4\gamma^2 f_0 .$$

The mean of the frequency distribution is at

$$f_{\mathrm{IC}} = \frac{4}{3}\gamma^2 f_0 . \tag{3.34}$$

As only inverse Compton scattering at the cosmic microwave background is discussed, this equation can be simplified using equations (3.30) and (3.23) and the characteristic energy of the inverse Compton photons can be calculated to be

$$E_{\mathrm{IC}} = h f_{\mathrm{IC}} = \frac{4 h f_0}{3 m_e^2 c^4} E^2 \approx 6 \times \left(\frac{E}{\mathrm{TeV}}\right)^2 \mathrm{GeV}$$

where E is the energy of the electron [see also AAK97, eq. (4)].

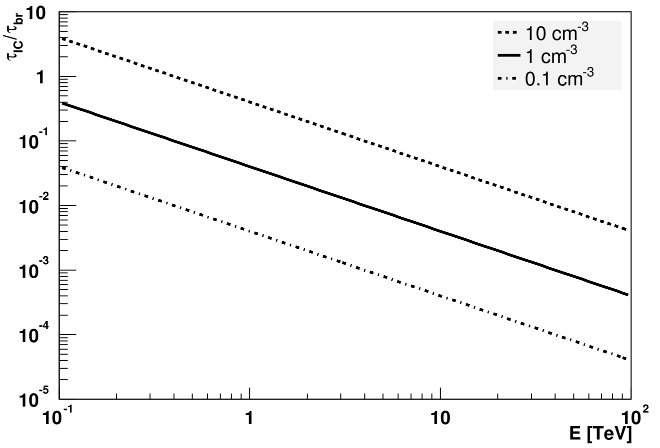

Figure 3.10: **Bremsstrahlung versus IC scattering.** The plot shows the ratio of the cooling times due to inverse Compton scattering on the cosmic microwave background and bremsstrahlung as a function of the electron's energy.

3.6.3 Comparison of the Emission Processes of Electrons

It has been shown in the last sections that accelerated electrons can produce high energy photons via three processes. In this section these processes are compared and some conclusions for the interpretation of γ-ray measurements will be drawn.

Bremsstrahlung versus IC Scattering

Let us consider an electron population which is capable of emitting bremsstrahlung photons with energies of more than 100 GeV. These electrons must have energies of at least 100 GeV. The energy losses due to bremsstrahlung and inverse Compton scattering on the cosmic microwave background can be compared using the ratio of the cooling times (equations 3.18 and 3.33):

$$\frac{\tau_{\mathrm{IC}}}{\tau_{\mathrm{br}}}(E) = 0.04 \left(\frac{E}{\mathrm{TeV}}\right)^{-1} \left(\frac{n}{1\,\mathrm{cm}^{-3}}\right). \tag{3.35}$$

Figure 3.10 shows this ratio for several densities of the interstellar medium and electron energies between 100 GeV and 100 TeV. It can be seen that this ratio declines for rising electron energies. For densities of $1\,\mathrm{cm}^{-3}$ and lower the cooling time due to inverse Compton scattering is shorter than the cooling time due to bremsstrahlung by several orders of magnitude. Only for high densities ($> 1\,\mathrm{cm}^{-3}$) and electron energies of less than 1 TeV the bremsstrahlung process is more efficient than the inverse Compton process.

In this work, energy loss due to bremsstrahlung will be neglected in the discussion of electronic scenarios.

Synchrotron Radiation versus IC Scattering

The energy losses due to synchrotron and inverse Compton radiation depend on the energy of the electrons. Further on, the energy loss due to synchrotron radiation depends on the magnetic field strength B. Based on the assumption that the observed synchrotron and inverse Compton radiation originate from the same electron population, the energy losses of both processes can be related to each other and thus the energy dependence is cancelled out. This allows conclusions on the expected inverse Compton energy flux on the basis of observed synchrotron radiation. This discussion follows the calculations of **(author?)** [AAK97].

Let us assume a population of electrons in the energy range $[E, E + \Delta E]$ with a number density of

$$\frac{\mathrm{d}N}{\mathrm{d}E} = n(E).$$

The energy distribution of these electrons is

$$W(E) = En(E).$$

The luminosity of synchrotron radiation and inverse Compton radiation can be calculated using the cooling times:

$$L_{\mathrm{sy,IC}} = \int\limits_{E}^{E+\Delta E} \frac{En(E)}{\tau_{\mathrm{sy,IC}}(E)} \mathrm{d}E.$$

Using the constant

$$C = \frac{3m_e^2c^3}{4\sigma_{\mathrm{T}}}$$

the cooling times can be written as

$$\begin{aligned} \tau_{\mathrm{sy}}(E) &= \frac{C}{U_{\mathrm{mag}}E}, \\ \tau_{\mathrm{IC}}(E) &= \frac{C}{U_{\mathrm{rad}}E}. \end{aligned}$$

The ratio of the luminosities due to synchrotron radiation and inverse Compton scattering depends only on the energy densities of the magnetic field and the photon field:

$$\frac{L_{\mathrm{IC}}}{L_{\mathrm{sy}}} = \frac{U_{\mathrm{rad}}}{U_{\mathrm{mag}}}, \tag{3.36}$$

and is independent of the electron spectrum $n(E)$. With the calculations of the energy densities for the magnetic field and the cosmic microwave background (equations 3.21 and 3.32) this ratio can be written as

$$\frac{L_{\mathrm{IC}}}{L_{\mathrm{sy}}} = 10^{-3} \left(\frac{B}{100\,\mu\mathrm{G}} \right)^{-2} . \tag{3.37}$$

The ratio depends only on the square of the magnetic field strength B.

The last equation compared the luminosities of the synchrotron and inverse Compton radiation. Now the energies of the radiated photons will be compared. For this purpose further approximations are made. Assuming that most of the radiation is emitted at the maximum of the frequency distributions, f_{sy} (eq. 3.25) for the synchrotron radiation and f_{IC} (eq. 3.34) for the inverse Compton scattering, the ratio of energies of the synchrotron photons E_{sy} and of the inverse Compton photons E_{IC} is

$$\frac{E_{\mathrm{IC}}}{E_{\mathrm{sy}}} = \sqrt{\frac{2}{3} \frac{8\pi m_e}{e}} \times \frac{f_0}{B} .$$

Only inverse Compton scattering at the cosmic microwave background is considered and with equation (3.30) the relation is simply

$$\frac{E_{\mathrm{IC}}}{E_{\mathrm{sy}}} = 3 \times 10^{9} \left(\frac{B}{100\,\mu\mathrm{G}} \right)^{-1} . \tag{3.38}$$

This relation depends only on the strength of the magnetic field B.

From equation (3.38) an important conclusion can be drawn. Synchrotron emission from supernova remnants has been observed in the energy range between 0.5 keV and 10 keV. In shock fronts of SNRs, the acceleration region of the electrons, magnetic fields between $100\,\mu$G and $500\,\mu$G are discussed [see e.g. VBK05, BYH05]. For these magnetic field strengths γ-rays with energies up to 10 TeV can be expected. This energy range can be observed with H.E.S.S.

Chapter 4

The H.E.S.S. Experiment

We have seen that supernova remnants can produce γ-rays in the very high energy (VHE, energies between 30 GeV and 30 TeV) regime. These photons do not reach the Earth's surface. Rather, they are absorbed in the atmosphere by the generation of particle showers. H.E.S.S. is an experiment designed to use the upper atmosphere as a calorimeter, allowing the reconstruction of the source direction and the energy of the arriving γ-rays.

In section 4.1 of this chapter, the generation of particle showers in the atmosphere and the Cherenkov light which is used to detect these showers will be discussed. The experimental setup of H.E.S.S. will be explained in detail in section 4.2. Using data of the Crab Nebula, the performance of H.E.S.S. and the analysis chain will be demonstrated in section 4.3.

4.1 Particle Showers in the Atmosphere

Photons and particles at very high energies have enough energy to create cascades of photons and particles (of lower energy) in the interaction with the atmosphere. Two scenarios have to be distinguished. Photons and electrons generate electromagnetic showers, while protons, neutrons and nuclei generate hadronic showers.

4.1.1 Electromagnetic Showers

Photons of energies considered here exceed twice the rest mass of electrons ($2m_e \approx 1\,\mathrm{MeV}$) by several orders of magnitude. Hence, the photon can produce an electron/positron pair within the field of a charged particle, like a nucleus in an air molecule. As long as the electrons and positrons have enough energy they predominantly loose their energy by radiating photons

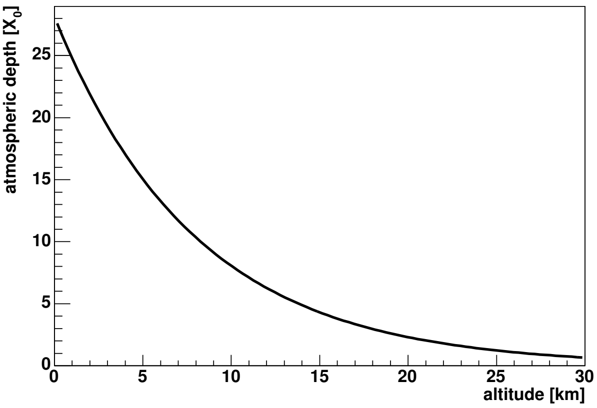

Figure 4.1: **Atmospheric depth profile.**

via the bremsstrahlung process within the field of the nuclei. If the photons produced by bremsstrahlung have enough energy they again undergo pair-production. This causes a particle multiplication and an electromagnetic shower is generated. At lower energies of the secondary particles, energy loss due to ionisation of the atmosphere becomes important. Finally, if the electrons have lost the major part of their energy they are captured by ions. The positron can annihilate with electrons producing a pair of photons.

The development of a shower strongly depends on the medium in which it is generated. In order to describe the shower characteristics independently of the medium, the quantities radiation length and Molière radius are introduced.

The radiation length X_0 is defined as the area density over which a high-energy particle ($\gg 1\,\mathrm{GeV}$) loses, on average, a fraction $1 - e^{-1}$ (i.e. 63.2%) of its energy due to bremsstrahlung. The radiation length of air is $37\,\mathrm{g\,cm^{-2}}$ [EHO+04]. It depends on the density of air and thus on the altitude above sea level, h. Using the atmospheric density profile of an atmosphere with constant temperature

$$\varrho(h) = 1.3 \times 10^{-3}\,\mathrm{g\,cm^{-3}} e^{-h/8\,\mathrm{km}}$$

one can write the atmospheric depth X in units of the radiation length for a particle travelling from infinity down to an altitude h as

$$X/X_0 = 28 e^{-h/8\,\mathrm{km}}.$$

The atmospheric depth as a function of the altitude is shown in Fig. 4.1. Let us assume a very simple shower model. The primary photon of energy E_0 produces within the first radiation length an electron/positron pair with energies of $E_0/2$ each. Within the next radiation length (the small difference between the radiation lengths for bremsstrahlung and pair-production will be neglected) the electron or positron emits a photon of energy $E_0/4$ via bremsstrahlung. In the N_X'th step $N(N_X) = 2^{N_X}$ particles are produced with energies of $E(N_X) = E_0/2^{N_X}$ each. The shower ceases when the energies of the particles drops below the critical energy ϵ_c where ionisation becomes important. The critical energy is defined as the energy at which the particle would loose its entire energy within one radiation length,

$$\left[\frac{\mathrm{d}\epsilon_\mathrm{c}}{\mathrm{d}x}\right]_\mathrm{ion} X_0 = \epsilon_\mathrm{c}.$$

In air, the critical energy is 87 MeV [Wig00]. The shower ends after N_X radiation lengths where N_X can be calculated as

$$N_X = \frac{\ln E_0/\epsilon_\mathrm{c}}{\ln 2}$$

which is for a primary photon of energy $E_0 = 1\,\mathrm{TeV}$ after $\approx 13.6\,X_0$ or, according to Fig. 4.1 at an altitude of $\approx 6\,\mathrm{km}$. The number of particles generated in total can be approximated as

$$N_\mathrm{max} = \frac{E_0}{\epsilon_\mathrm{c}}$$

which is in case of an 1 TeV photon $\approx 10^4$.

Electromagnetic showers are quite narrow. The left panel of Fig. 4.2 shows the simulation of an air shower of a primary photon with an energy of 300 GeV. The lateral extent of an electromagnetic shower is produced by multiple scattering and is described in a medium-independent way by the Molière radius, r_M. On average, 90% of the shower energy is deposited in a cylinder with the radius r_M around the shower axis. It is defined as

$$r_M = X_0 \frac{E_\mathrm{s}}{\epsilon_\mathrm{c}}$$

with the critical energy ϵ_c and the radiation length X_0. The scaling energy E_s is defined as $m_e c^2 \sqrt{4\pi/\alpha} = 21.2\,\mathrm{MeV}$, where c is the speed of light and α is the fine-structure constant. In air, the Molière radius is $r_M = 9.8\,\mathrm{g\,cm^{-2}}$ which corresponds to a shower radius of 200 m at an altitude of 8 km. Details on the development of electromagnetic showers can be found in [Wig00].

Obviously, an initial electron or positron impinging the atmosphere can produce the same electromagnetic cascade as a photon, just by starting with the bremsstrahlung process. Showers initiated by photons or electrons/positrons have a similar shower shape and can thus not be distinguished using the shape of the shower.

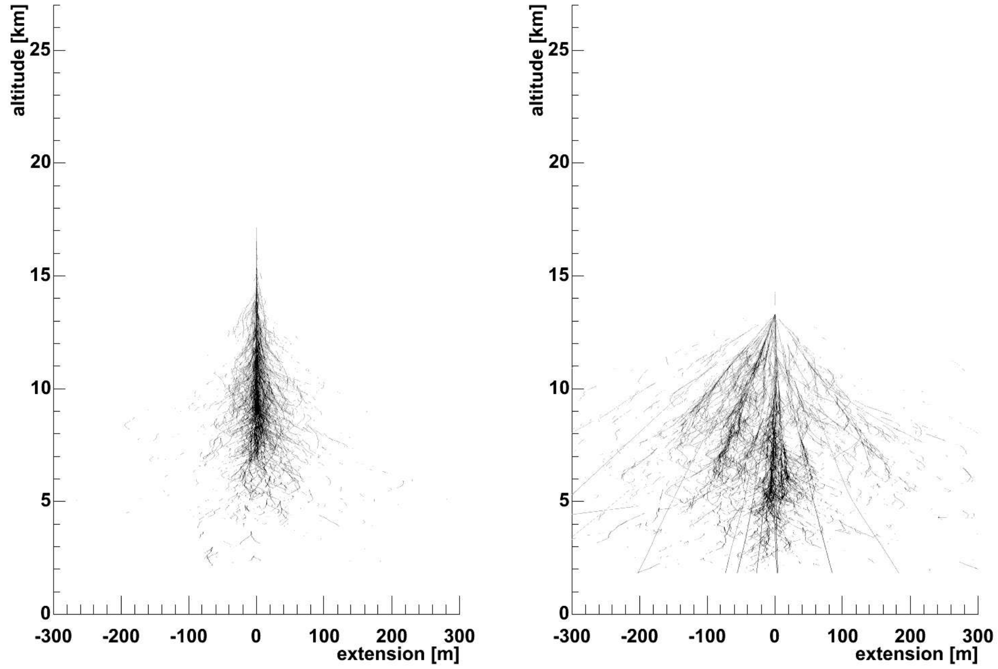

Figure 4.2: **Side View of simulated air showers.** Only secondary particles which emit Cherenkov light are shown. The air showers are generated by a 300 GeV γ-ray (left panel) and a 1 TeV proton (right panel). The pictures were taken from [Ber00].

4.1.2 Hadronic Showers

Protons and heavier ions of the cosmic radiation can also produce air showers. But additionally to electromagnetic interactions strong interactions of the ions with the nuclei of the air molecules play an important role. In these interactions further hadrons can be produced. Among them are neutral pions (π^0) which decay predominantly into two photons:

$$\pi^0 \rightarrow \gamma\gamma.$$

These photons initiate electromagnetic sub-showers. Hence a hadronic shower always contains a significant component of electromagnetic sub-showers.

The π^0 created in nucleonic interactions carry a significant transverse momentum. Thus, the electromagnetic sub-shower generated by the photons from the π^0 decay do not follow the initial direction of the incident proton and the hadronic shower is spread out. A simulation of an air shower induced by a proton of 1 TeV is pictured in the right panel of Fig. 4.2. It can be seen that the hadronic shower comprises several sub-showers and has a larger lateral extent compared to an electromagnetic shower. This will be used for discrimination between electromagnetic and hadronic showers in the analysis of γ-ray observation data.

Details on hadronic showers in general and in the Earth's atmosphere in particular can be found in [Wig00].

4.1.3 Cherenkov Light of Air-Showers

If the energy of a charged particle is sufficiently large that it travels faster than the speed of light in the medium then it emits Cherenkov radiation. The condition can be written as

$$\beta = \frac{v}{c} > \frac{1}{n},$$

where v is the speed of the particle, c the speed of light in vacuum and n the refraction index of the medium. The refraction index of air at the Earth's surface is $n_0 = 1.0003$. Particles capable of Cherenkov emission must have a velocity of $\beta > 0.9997$. Electrons and positrons emit Cherenkov light if they have an energy of at least 21 MeV. This is the case for all electrons and positrons in electromagnetic showers before they reach the critical energy and loose their energy by ionisation. In analogy to the Mach cone of an aeroplane at supersonic speed, the spherical Cherenkov light fronts generated at different positions of the flight path interfere to a cone-like wave front. This is illustrated in Fig. 4.3. Within a time unit T the particle travels a distance $\beta c T$ while the Cherenkov light travels only a distance cT/n. The opening angle Θ of the Cherenkov cone can be calculated from trigonometric considerations as

$$\cos\Theta = \frac{1}{n\beta}.$$

The maximum opening angle, which is reached if the particle's speed reaches the speed of light in vacuum, $\beta = c$, is $\cos\Theta = 1/n$. The refraction index n decreases with increasing altitude, $(n-1)$ is proportional to the density of the atmosphere:

$$n(h) = 1 + (n_0 - 1)e^{-h/8\,\mathrm{km}}.$$

With increasing altitude the refraction index and thus the opening angle of the Cherenkov cone decreases. Cherenkov light emitted at an altitude h generates an light pool at the Earth's surface at an altitude H with maximal radius

$$R_{\max}(h) = (h - H)\tan\Theta.$$

The maximum radius of the Cherenkov light pool in an altitude $H = 1.8\,\mathrm{km}$ (which is the altitude of H.E.S.S.) is plotted in Fig. 4.4. It can be seen that $R_{\max}$ reaches a maximum of 130 m and is larger than 100 m over a wide altitude range. The left panel of Fig. 4.5 shows the simulated Cherenkov light distribution of a 300 GeV photon. The picture shows a circular light pool with brightened edge. The radius of the light pool is $\approx 130\,\mathrm{m}$. The right panel shows the Cherenkov light distribution of a 1 TeV proton. The light pools of several electromagnetic sub-showers can be seen. The light is asymmetrically distributed and spread over a larger area.

As the shower develops almost at the same speed as the propagation of the Cherenkov light, the light pulse on the ground is very short. Assuming a constant refraction index n_0, the Cherenkov light generated in a height h needs a time

$$t = \frac{h n_0}{c}$$

to reach the ground. The difference of the arrival times of Cherenkov light generated in heights h_1 and h_2 is

$$\Delta t = \frac{n_0}{c}\left(h_1 - h_2\right).$$

For a shower of length $\Delta h = 6\,\mathrm{km}$ the Cherenkov light arrives within 6 ns. Hence, for the detection of the Cherenkov light a very fast camera is needed.

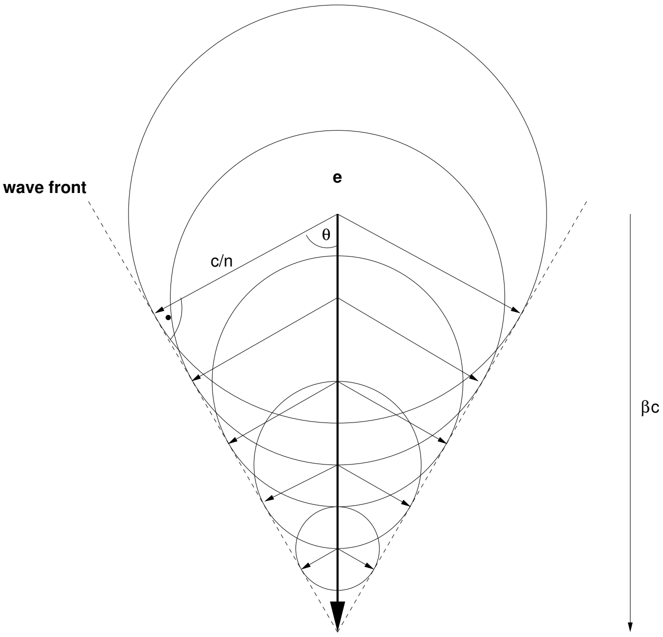

Figure 4.3: **Cherenkov cone.**

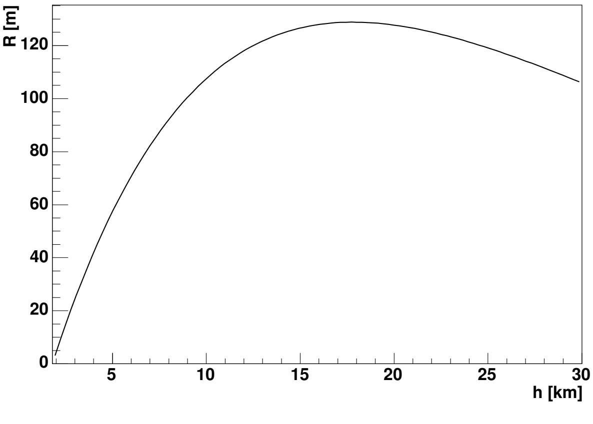

Figure 4.4: **Maximum Cherenkov radius.** R is the maximum radius of the Cherenkov light pool at the H.E.S.S. site (1800 m above sea level) for Cherenkov light emitted at an altitude h.

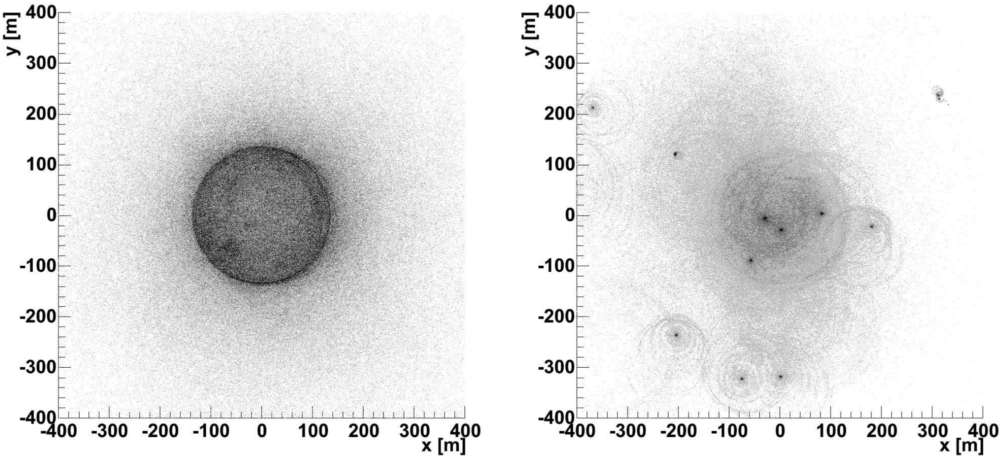

Figure 4.5: **Cherenkov light distribution on the ground of simulated air showers.** The air showers are generated by a 300 GeV γ-ray (left) and a 1 TeV proton (right). [Ber00]

Figure 4.6: **The H.E.S.S. experiment.** The photograph shows the four individual telescopes. In the foreground the telecommunication antenna, the control building and the power house can be seen.

4.2 Experimental Setup of H.E.S.S.

H.E.S.S. (High Energy Stereoscopic System) is an experiment dedicated to the observation of cosmic VHE γ-rays by the detection of the Cherenkov light of their air showers. The acronym H.E.S.S. reminds of Viktor Franz Hess, the discoverer of the cosmic rays. H.E.S.S. makes use of the stereoscopic observation of air showers, as first conducted by the HEGRA collaboration [KAA$^+$96]. H.E.S.S. was built in collaboration of 19 institutes from 8 European and African countries. It started its observations in June 2002 with the first telescope, and the full system, comprising 4 telescopes, is operational since the beginning of 2004. Figure 4.6 shows the setup of H.E.S.S. in the Khomas Highland of Namibia.

4.2.1 The Site

The H.E.S.S. experiment is located in the Khomas Highland of Namibia in southern Africa. The exact coordinates are $16^{\circ}30'00\overset{s}{.}8$ East, $23^{\circ}16'18\overset{s}{.}4$ South. The region is sparsely inhabited, and therefore no artificial light sources influence the measurements. The clear air reduces the light extinction due to aerosols in the atmosphere to a minimum. Apart from the raining season from January to March most of the nights are clear and cloudless allowing observations with high efficiency. The location on the southern hemisphere of the Earth allows the observation of the southern celestial sphere. The Galactic Centre and the inner part of the Milky Way, one of the most interesting regions, can be observed at high elevations. Together with three other Cherenkov telescope systems, CANGAROO, MAGIC and VERITAS, the entire celestial sphere can be observed in VHE γ-rays.

The four telescopes are arranged in a square with a baseline of 120 m. The spacing of the telescopes has been chosen to match the radius of the light cone of an air shower, providing the best chance of observing a shower by several telescopes.

4.2.2 Mount and Tracking

One of the H.E.S.S. telescopes is shown in Fig. 4.7. Each telescope is supported by a steel structure. The structure is designed for high mechanical rigidity to minimise the effects of bending and tilting due to the weight of the camera and the drag of the wind. The telescope is placed on a rail with a diameter of 13.6 m allowing the telescope to turn parallel to the horizon. The angle counting clock-wise from north to the telescope direction in the plane parallel to the horizon is the azimuth angle. A spherical dish of a 15 m

Figure 4.7: **A H.E.S.S. telescope.** The support structure, mirror dish and the camera can be seen. In front of the telescope is the camera hut. The white container at the back of the telescope contains the electronics. The poles are two of the four lightning protection masts.

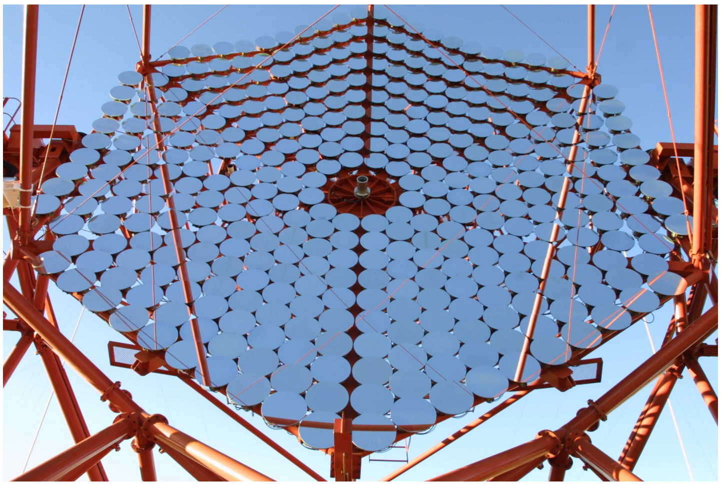

Figure 4.8: **The reflector of a H.E.S.S. telescope.** The mirror consists of 380 mirror facets mounted on a hexagonal frame. The Lid CCD is in the centre of the dish. Half way between the centre and the left edge of the dish the Sky CCD is located.

focal length can be rotated perpendicular to the horizon. The angle between the ground and the telescope direction is the altitude. The inverse of the altitude ($90° - \mathrm{alt}$) is called zenith angle. In the focus of the dish the camera is mounted on four supporting steel masts.

In order to keep the source in the centre of the camera permanent tracking is required. The telescopes are driven by friction drives acting on 15 m drive rails with a slewing speed of 100°/min. The position is sensed by shaft encoders with a digital step size of $10''$. Details of the drive system can be found in [Bol04]. The position of the source in the camera can be maintained with an accuracy of $30''$ [Gil04]. The pointing of the telescope can be controlled with an optical telescope mounted in the dish (Sky CCD) observing stars in the surrounding of the source. The positions of the stars in the Sky CCD can be used to correct mis-pointing due to wind drag at the reflector dish.

4.2.3 The Optical System

The reflector of each telescope consists of 380 mirror facets mounted in a hexagonal dish with a flat-to-flat width of 13 m. Both the mirror facets and the dish are spherical with a focal length of 15 m. A picture of the dish and the mirror facets is shown in Fig. 4.8. Mounting spherical mirrors on a spherical frame of the same focal length is the so-called Davies-Cotton layout, which was initially designed for a solar furnace used as test facility for protection equipment against thermal radiation from nuclear weapons [DC57]. This design is cost-efficient and provides an essentially point-like focus for rays parallel to the optical axis. Off-axis rays suffer from significant aberrations. The spherical design of the dish introduces a time dispersion of $\approx 5\,\mathrm{ns}$.

The individual mirror facets are made of aluminised optical glass, coated with quartz for outdoor use. For cost-reasons round mirrors with a diameter of 60 cm were preferred to hexagonal mirrors, which would cover the dish completely. The reflectivity in wavelengths between 300 and 600 nm exceeds 80%. At least 80% of the reflected light is focused into a circle in the focal plane with a diameter of 1 mrad.

The total reflecting area of $107\,\mathrm{m}^2$ is reduced by shadows of the camera and camera support structure to $\approx 95\,\mathrm{m}^2$, depending slightly on the angle of incidence. Details of the optical system of H.E.S.S. can be found in [BCC$^+$03].

The mirror facets are attached to the dish on three points, whereof two are actuators which can be used to tilt the mirrors individually. For alignment of the mirrors a CCD mounted in the centre of the dish, called the Lid CCD, observes the light of a star reflected onto the lid of the camera. After installation of the mirrors the star images are spread about 1°. The mirrors are moved individually until all images are focused in the centre of the camera lid. After alignment, 80% of the light of the star is focused into a circle with a radius of $\approx$0.4 mrad, depending on the incidence angle and the observation altitude. The alignment has been found to be stable at time scales of years [CGJ$^+$05]. The details of the mirror alignment and the performance of the reflector can be found in [CGJ$^+$03].

The mirror reflects the incoming Cherenkov light onto the camera which is located in the focus of the dish. The pointing direction of the telescope is mapped to the centre of the camera. Any displaced signal in the camera corresponds to an angular distance from the pointing direction at the celestial sphere.

4.2.4 The Cameras

The right panel of Fig. 4.9 shows one of the cameras mounted in the focus of the telescope. Each camera consist of 960 pixels and covers a field of view with a diameter of 5°. The pixels are arranged in a hexagonal shape, such that each pixel which is not located at the edge of the camera has six neighbours. Each camera is contained in a body of 2 m length and $\approx$1.6 m width and has a mass of about 900 kg. The camera body also holds the power supplies as well as the electronics for signal processing, triggering and digitisation [Ve03]. The front of each camera is covered by a lid shielding the pixels from the day light. The lid, slightly opened, can be seen in the right panel of Fig. 4.9. During day the cameras are parked in shelters, the camera huts, for rain protection.

Figure 4.9: **A H.E.S.S. camera.** The photographs show the camera from the back (left panel), the front view with opened lid (middle panel) and the camera mounted in the focus of the telescope (right panel). The pictures are taken from [Ve03].

The pixels are photomultiplier tubes (PMTs) with a quantum efficiency of about 30% and a field of view of 0.16°. The high voltage is provided by the PMT bases and is calibrated to generate a signal of 2×10^5 electrons for each photo electron (p.e.). To cover a large dynamical range, the pulse from each PMT is divided into two channels with different amplification factors. A high-gain channel for signals in the range between 1 and 100 p.e. and a low-gain channel for pulses with 10 to 1600 p.e. Groups of 16 PMTs form a drawer, which holds also the power supplies for the PMTs, two data acquisition cards for 8 PMTs each and three temperature sensors. The drawers can be easily extracted from the body and replaced. Winston cones in front of the pixels collect the light which would fall in-between the PMT windows and restrict the PMT's field of view to the angular size of the mirror. The middle panel of Fig. 4.9 shows a front view of the camera with the Winston cones in front of the PMTs.

The camera readout pipeline makes use of the ARS (Analogue Ring Sampler) chip, which was initially developed for the ANTARES experiment [FA03]. It samples the signal at 1 GHz and stores it in 128 cells while awaiting the trigger decision. Triggered events will be read out from a time window of 16 ns. The signal is digitised by an ADC (analogue-to-digital converter), usually by integrating over the entire time window, into ADC counts. The integration window of 16 ns is appropriately large to contain the time spread of the Cherenkov pulse of ≈ 6 ns and the time dispersion due to the reflector design of $\approx 5\,\mathrm{ns}$. For test purposes the signal can also be digitised cell by cell, the so-called "sample-mode".

The data acquisition system of the camera is written in C and is running on a Linux operating system. The system controls also the 95 fans, 16 temperature sensors and a GPS (Global Positioning System) card to obtain the arrival time of the events. The entire read out electronics of the camera is incorporated in the camera body. The left panel of Fig. 4.9 shows a rear view of the camera where the power supplies and readout electronics are located. The digitised events will be sent to the Central Data Acquisition (DAQ) system. After receiving the trigger signal it takes $610\,\mu\mathrm{s}$ until the data are sent to the Central DAQ. This readout time defines the dead time of the camera per event which corresponds to a maximum acquisition rate of the camera of $1.6\,\mathrm{kHz}$.

4.2.5 The Trigger

The decision which event will be read out and stored for further analysis is made by a 2-step trigger. The first step is formed on the camera level. The second step is a coincidence trigger which triggers the readout of all cameras of the array.

A pixel is triggered if the number of photo electrons exceeds a certain value, typically 4 p.e. during normal observations. The camera is sub-divided into 38 overlapping sectors comprising 64 PMTs each. The sector overlap ensures a homogeneous efficiency over the camera. A sector trigger is raised when a number of pixels, typically 3, in one sector exceeded the pixel threshold. The sector trigger reduces the night-sky-background (NSB) significantly, since air-showers form images with clusters of pixels while the NSB affects single pixels and is randomly distributed in the camera.

The readout of all cameras is triggered by a Central Trigger System (CTS) based on coincident telescope triggers [FHH$^+$04]. The telescope multiplicity is programmable, in observation mode typically a coincidence of at least two telescope triggers is required. This ensures that an air-shower is observed by at least two telescopes. Single muons, which form a major part of the background in a single telescope, are rejected almost completely since they trigger only one telescope.

The CTS is also responsible for dead-time measurement and event synchronisation. Each telescope provides with the trigger signal the current readout status, i.e. the camera is busy with the acquisition of a previous event or it is active for readout of the current event. In case of a busy camera the data of this telescope for this particular event is lost. Based on this information, the CTS can derive the dead-time. The camera data are sent

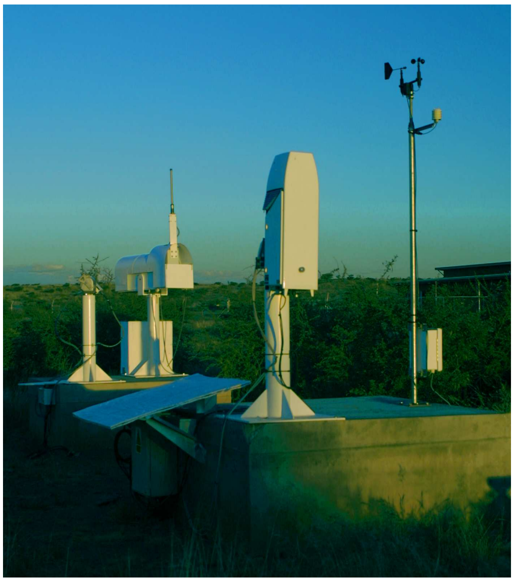

Figure 4.10: **Equipment for weather and atmospheric monitoring.** From left to right can be seen the scanning radiometer, the transmissometer, the LIDAR and the weather station.

to the central data acquisition system individually. In order to connect the different camera images to a single event, the CTS assigns a unique event number which is distributed to all cameras. When a telescope triggered but no coincidence occurred, the CTS instructs the cameras to stop the readout. This prevents the cameras from reading out single events and reduces the dead-time significantly.

4.2.6 Weather and Atmospheric Monitoring

In addition to the recording of the camera images of the air showers the atmospheric conditions need to be monitored. At the H.E.S.S. site a fully automatic weather station has been installed. It records the air temperature, relative humidity, atmospheric pressure, wind speed, wind direction and rain fall over 24 h a day. The data are displayed on-line in the control room and are stored on disk. Further equipment is used to observe the atmospheric quality and the clouds in the sky. Figure 4.10 shows a photograph of the weather station in the centre of the H.E.S.S. array.

Radiometer

Infrared radiometers are used for cloud detection. These radiometers measure the radiation in a wavelength window between 8 and 14 μm. The measured value can be compared with a blackbody spectrum and a radiative temperature can be calculated. This temperature is not the temperature of the air or

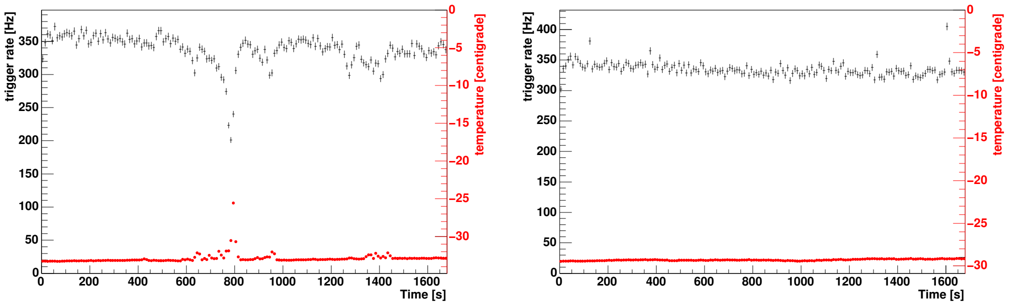

Figure 4.11: **Correlation of the trigger rate and the radiometer temperature.** The trigger rate is denoted by the black data points (left axis) the temperature by the red points (right axis). The left panel shows the data for run 18930 where clouds were passing (rising temperature). The anti-correlation between the trigger rate and radiometer temperature can be seen. The right panel shows run 18947 with clear sky and stable trigger rate.

a cloud. Clouds reflect the ambient light, and therefore they show a higher temperature than the clear sky. The radiometer readings of a clear sky may change on timescales of hours to days due to changing humidity and atmosphere temperature and is in general dependent on the zenith angle. Details on the radiometer can be found in [Le 03].

Each of the telescopes is equipped with a radiometer paraxially mounted which observes the same region of the sky as the telescope. The red data points in Fig. 4.11 shows the time-lines of the radiometer temperature of one telescope in two runs. The left panel of Fig. 4.11 shows a run where clouds passed by producing the peaks in the radiometer temperature. A run without clouds is shown in the right panel of Fig. 4.11 with a stable temperature. The black points in Fig. 4.11 denote the trigger rate showing a clear anti-correlation with the radiometer temperature. Due to the unstable cloud and trigger conditions in run 18930 (shown in the left panel of Fig. 4.11), this run is excluded from the analysis presented in chapter 5.

Another radiometer is mounted in the centre of the array on a pan-tilt unit. This radiometer can scan the whole sky during day and night providing an immediate overview of the sky for the presence of clouds and approaching weather fronts.

Ceilometer

While the radiometer provide only a measurement of the existence of clouds, the transmissivity of the atmosphere can be measured using the ceilometer. The ceilometer is a LIDAR (LIght Detection And Ranging), a device which points a laser into the atmosphere and measures the backscattered light which is connected to the amount of aerosols in the atmosphere. Measuring the time of flight of the laser pulse an atmospheric profile of the backscattered light up to a height of 7.5 km can be achieved. Details on the ceilometer can be found in [Bro05].

A correlation of the trigger rate and the amount of aerosol as measured with the LIDAR has been shown by **(author?)** [LNMS05]. It is shown that the integral γ-ray flux above 1 TeV is not affected by the aerosols in the atmosphere but a correction of the effective areas due to the absorption by aerosols might be necessary for lower energies.

4.2.7 Central Data Acquisition System

The camera images of the air shower, as well as the atmospheric conditions and other monitoring data are sent to the Central Data Acquisition System (DAQ). The subsystems provide their data at very different rates. The data of all four cameras can reach a maximum rate of ≈ 1 kHz while the weather station has a data rate of 0.1 Hz. For each subsystem the DAQ provides data receivers and reads out the data asynchronously. The data receivers collect the data which is converted on-line into a ROOT [BRB$^+$05] format ready for analysis.

A modular design of the DAQ allows to combine the subsystems into different configurations, e.g. sub-arrays of telescopes or the exclusion of certain subsystems from the data stream. Additionally, the DAQ configures and controls all subsystems. All configuration parameters needed for operation are stored in a MySQL [MyS05] data base. These parameters includes hardware configurations as the high voltages for all pixels, the trigger conditions or the celestial coordinates of sources to be observed. The experiment can be operated from a computer terminal by a shift crew of typically two persons. Figure 4.12 shows the control room during data taking. The monitors on the upper shelf show on-line data, like the weather data, trigger rates, telescope pointings and on-line event displays. This information can be used for immediate check of the status of the subsystems and the quality of the recorded data. The experiment can be controlled by the computer terminal with two screens on the desktop.

The software of the DAQ uses an object-oriented design and is programmed in C++. The communication between the processes (interprocess communication) is done using the industrial CORBA standard in the omniORB [omn05] implementation. Details on the software can be found in [BKd$^+$03, BMS01]. The system is running on a Linux farm comprising 20 PCs with double Pentium CPUs connected via a Gigabit network. A picture of the processing farm is shown in Fig. 4.13. The data is stored on two 1.6 TB RAID hard disk arrays and is shipped on tapes to Europe for calibration, data reduction and analysis.

4.2.8 Calibration

The voltage generated by a photon in a pixel is digitally stored as ADC counts. This value needs to be transformed into an intensity measured in photo electron counts. Additionally, the different efficiency of the pixels needs to be levelled out ensuring a uniform acceptance over the camera.

Each pixel provides two values, the ADC counts ADC^{HG} in the high gain channel and ADC^{LG} in the low gain channel. The intensity, measured in photo electrons, can be calculated from the ADC counts using

$$A^{\mathrm{HG}} = \frac{ADC^{\mathrm{HG}} - P^{\mathrm{HG}}}{\gamma_e^{ADC}} \times FF$$

for the high-gain channel and

$$A^{\mathrm{LG}} = \frac{ADC^{\mathrm{LG}} - P^{\mathrm{LG}}}{\gamma_e^{ADC}} \times FF \times (HG/LG)$$

for the low-gain channel. In this calculation a number of calibration parameters are needed. P is the PMT's pedestal position, measured in ADC counts in the two channels. The quantity γ_e^{ADC} is the gain of the high-gain channel. To obtain the gain in the low gain channel, γ_e^{ADC} is divided by the ratios of the amplifications in the two channels, HG/LG. Finally, FF is the flat-field coefficient which levels out the differences between the individual pixels. For calibration the pedestal positions, the high-gain γ_e^{ADC}, the gain ratios HG/LG and the flat-field coefficients FF must be provided.

The pedestal P is the mean ADC value recorded in the absence of Cherenkov light. In the dark (when the camera lids are closed) the electronics generates a narrow Gaussian ADC distribution the mean of which is the pedestal position. The pedestal position depends on the camera temperature. During observations the night sky background broadens and shifts the ADC distribution of the pedestals. The pedestal distribution can be estimated from observation data. A typical air-shower image contains only 20 pixels.

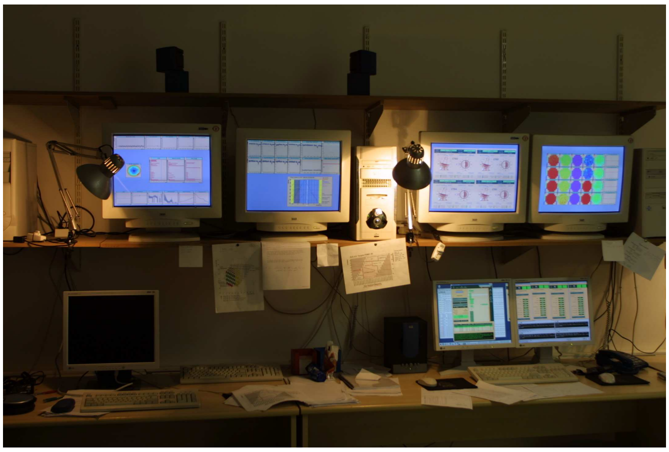

Figure 4.12: **Control room of the H.E.S.S. experiment.** The picture shows the desktop from where the experiment can be operated. On the lower right hand side are two monitors with the central DAQ user's interface. The upper monitors show information of the on-line monitoring.

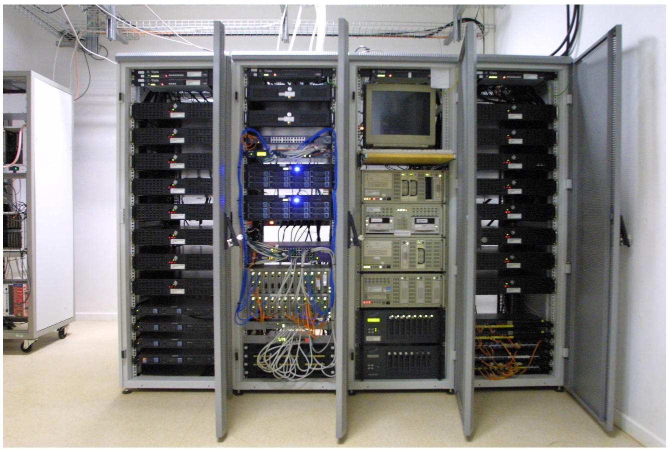

Figure 4.13: **The computer cluster.** The picture shows the racks with the computers of the data acquisition cluster. The outer racks contain the farm computers, the next to left rack contains the network switches and RAID arrays. The next to right rack contains the server, tape drives and additional hard disks.

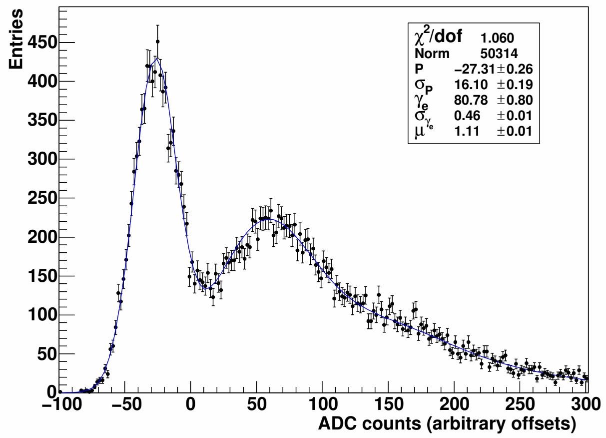

Figure 4.14: **ADC distribution of a Single Photo Electron Run.** The plot shows the distribution of ADC counts in a Single Photo Electron Run. The blue line denotes a fit to the distribution. The plot is reproduced from [AAA⁺04a].

From the pixels not illuminated by Cherenkov light the pedestal positions are extracted.

The gain in the high-gain channel, γ_e^{ADC}, is measured in dedicated "Single Photo Electron Runs". For this purpose, an LED flasher is installed inside the camera hut, roughly 2 m in front of the camera. The LED illuminates the camera with an intensity of about 1 p.e. per pixel and is pulsed at 70 Hz. From the ADC count distribution of these runs the gain can be calculated. Figure 4.14 shows the ADC distribution as measured in a Single Photo Electron Run. The peak at −27 ADC counts is the pedestal. A function which describes the pedestal with a Gaussian and assumes a Poisson distributed number of photo electrons describes the ADC distribution. A fit of this function to the data is denoted by the blue line in Fig. 4.14. From this fit the gain is calculated to be $\approx$ 80 ADC counts per p.e. for every pixel, with an RMS of $2 - 3$ counts over all pixels.

The ratio of gains in the high-gain and low-gain channel can be derived from normal observation data using the overlapping region between 10 and 100 p.e. of the two channels. The ratio HG/LG is approximately 13.5, the RMS over all pixels is 0.5.

Due to different efficiencies of the individual photo cathodes and Winston cones the pixel acceptance is not homogeneous over the camera. To correct for this differences, flat-field coefficients, FF, have to be determined. For this purpose, an LED flasher is mounted in the centre of the reflector dish [ACH⁺03]. The LED flasher produces short light pulses with a FWHM of 5 ns and illuminates the whole camera. The LEDs wavelength of 390 to 420 nm and its short pulses are well simulating a Cherenkov light pulse. The camera is externally triggered on the light pulses and the ADC count distribution is recorded. After calibration as described above the mean of all pixels in one camera is calculated. The inverse of the deviation of one pixel from the mean value is the flat-field coefficient, FF. By definition, the mean of FF is 1. The typical RMS of the FF distribution is $\approx 10\%$.

Dedicated "Single Photo Electron Runs" and "Flat-Fielding Runs" are taken every second night. The final calibration of the data is then done based on the mean parameters within one observation period of 4 weeks. A very detailed description of the H.E.S.S. calibration procedure along with a discussion of the stability of the calibration parameters can be found in **(author?)** [AAA+04a].

A raw camera image in the high gain channel prior to the calibration is shown in the left panel of Fig. 4.15. The image of the shower can hardly be seen. The middle panel shows the same event after calibration. The shower image is clearly enhanced. The rest of the camera is dominated by small fluctuations due to electronic noise and night sky background.

The camera calibration cannot provide an absolute calibration of the H.E.S.S. detector as it does not include the reflectivity of the mirrors and the absolute quantum efficiency of the PMTs. This can be either done by laboratory measurements of the individual components or using the Cherenkov light emitted by muons. Muons generated in hadronic air-showers produce a clear Cherenkov ring or arc in the cameras. From the diameter of these rings the energy of the muon can be calculated. The Cherenkov emission of muons is well understood and simulated. By comparing the measured values with the simulation an absolute calibration can be performed. This is discussed in [LBG+03].

4.2.9 Event Building

After calibration of the camera images the showers are reconstructed. First a basic image cleaning is performed. The cleaned images are parameterised using the second moments of the intensity distribution. From these image parameters the shower direction, impact position and energy can be calculated.

Image Cleaning

The fluctuations in the camera outside the actual shower image (see the middle panel of Fig. 4.15) need to be removed in order to restrict the camera image to the image of the shower. This image cleaning is based on the intensity in each pixel and the intensity in the (up to six) neighbouring pixels. All pixels with an intensity of less than 5 photo electrons (p.e.) are

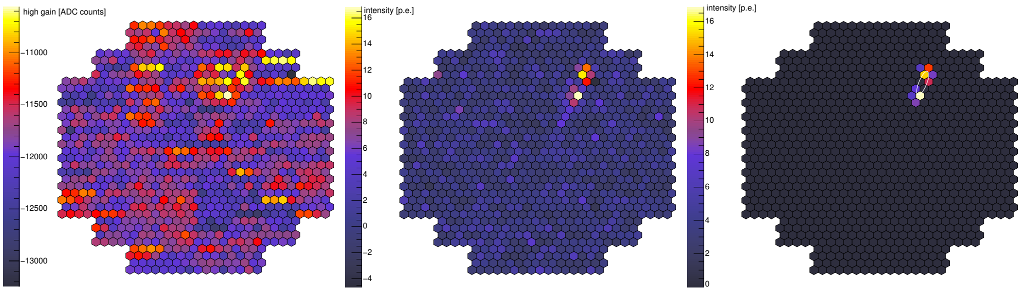

Figure 4.15: **Camera images.** The left panel shows the raw ADC counts in the high gain channel of the camera. The calibrated image is shown in the middle panel, the colour bar denotes the intensity in photo electrons. The right panel shows the image after image cleaning. In the cleaned image, the Hillas ellipse is denoted by the white line. The shower image is split into two pieces probably due to problematic pixels.

removed from the image. Pixels with an intensity of more than 10 p.e. and having a neighbour with at least 5 p.e. are kept in the cleaned image. Also those pixels with an intensity between 5 and 10 p.e. are kept if they have a neighbour with more than 10 p.e.

The right panel of Fig. 4.15 shows the camera image after image cleaning. The intensities of the excluded pixels are set to zero.

Image Parameterisation

The image of an electromagnetic air shower has an elongated, roughly elliptical shape. Therefore, it can be parameterised by an ellipse which was initially suggested by **(author?)** [Hil85]. The parameters of this ellipse are illustrated in Fig. 4.16. The position is defined by the centre of gravity or mean of the intensity distribution, (x, y). The second moments of the intensity distribution define the semi-major and semi-minor axis L and W, respectively. These quantities are the Hillas length and Hillas width, respectively. The distance of the centre of gravity to the centre of the camera is given by the local distance d. Finally, the orientation of the ellipse is parameterised with the angle α between the semi-major axis and the line connecting the centre of gravity with the centre of the camera. The Hillas ellipse of the shower image in the right panel of Fig. 4.15 is denoted by the white circle.

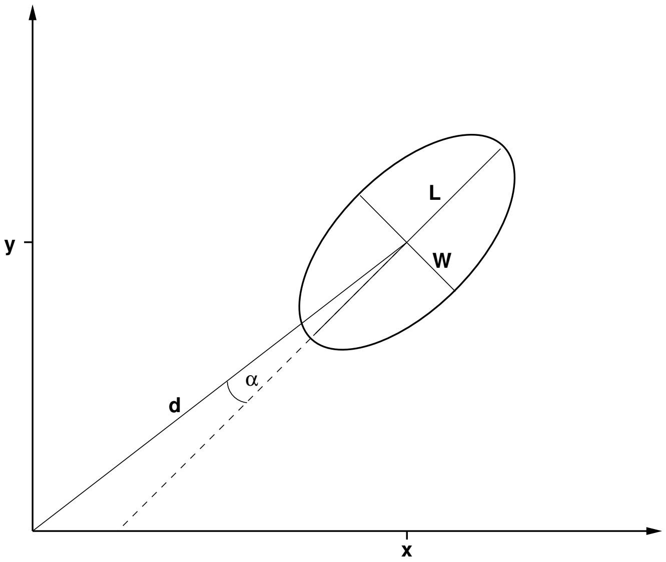

Figure 4.16: **Hillas parameters.** Definition of the Hillas parameters length L and width W of the ellipse, local distance d to the camera centre and the angle α between the orientation of the ellipse and the line connecting the centre of gravity with the camera centre.

Shower Reconstruction

The shower geometry can be described using the shower direction and the impact point. The shower direction is the extension of the shower axis to the celestial sphere. It is given in celestial coordinates and in case of a γ-ray it represents the source of the γ-ray in the sky. The impact point is the intersection of the shower axis with a plane perpendicular to the observation direction, usually the telescope plane which is in the centre of the H.E.S.S. array.

The simultaneous observation of an air shower by several cameras at different viewing angles allows the reconstruction of the source direction and impact point. Thus, only showers which were seen by at least two telescopes are reconstructed. The reconstruction is done using only the direction of a shower image with respect to the camera centre, which is defined by the major axis of the Hillas ellipse. Obviously, this will not work if the major axis is not very well defined. This is the case when a γ-ray induced shower hits the telescope and the image shows the shower from below. Images of hadron induced showers are fuzzy and consist of several electromagnetic showers. Hadron induced showers are not well parameterised by ellipses and thus the direction reconstruction is not very accurate.

For the determination of the source direction all shower images are projected into one camera plane or to the field of view in the sky. This is illustrated in the upper part of Fig. 4.17. The intersection point, mapped to the celestial sphere, denotes the source direction. If there are more than two images, the source direction will be calculated for each pair of images. Based on empirical considerations, each intersection point is weighted with

$$\rho = \frac{|\sin \Delta\beta|}{\left(\frac{1}{I_1} + \frac{1}{I_2}\right) + \left(\frac{W_1}{L_1} + \frac{W_2}{L_2}\right)}$$

where $\Delta\beta$ is the angle between the two images and the I_i are the image intensities in photo electrons, W_i the Hillas widths and L_i the Hillas lengths of the two images i. The numerator suppresses pairs of showers intersecting at small angles where the error on the intersection point is large. The first term of the denominator favours intersection points of bright intensity. The second term suppresses images with a high width over length ratio, and thus a not well defined major axis. The source position (x,y) is calculated as the weighted mean of all positions (x_i,y_i) of the N pairs,

$$(x, y) = \frac{\sum_{i=1}^{N} \rho_i (x_i, y_i)}{\sum_{i=1}^{N} \rho_i}.$$

The impact point can be calculated in an analogue way. The direction of a shower image in the camera and the telescope's pointing direction define a plane. The intersection of two such planes from different telescopes coincides with the shower axis. This is illustrated in Fig. 4.17. It should be noted that in the illustration the telescopes point to zenith and the ground can be taken as the telescope plane perpendicular to the telescopes' pointing direction. The intersection of the shower axis with the telescope plane is the impact point. For more than two images the impact point will be calculated from the weighted mean as described above with a weighting factor

$$\rho = \frac{|\sin \Delta\beta|}{\left(\frac{W_1}{L_1} + \frac{W_2}{L_2}\right)}.$$

A detailed description of the shower reconstruction algorithm can be found in [AHKV97]. A comparison of different algorithms was done by **(author?)** [HJK$^+$99].

4.2.10 Detector Simulation

For the energy estimation of the reconstructed showers and for further analysis the knowledge of the detector response is crucial. The detector response is inferred from Monte Carlo simulations.

Air showers are simulated using the CORSIKA package [HKC$^+$98]. CORSIKA can simulate photons, leptons, neutrons, mesons and light nuclei from

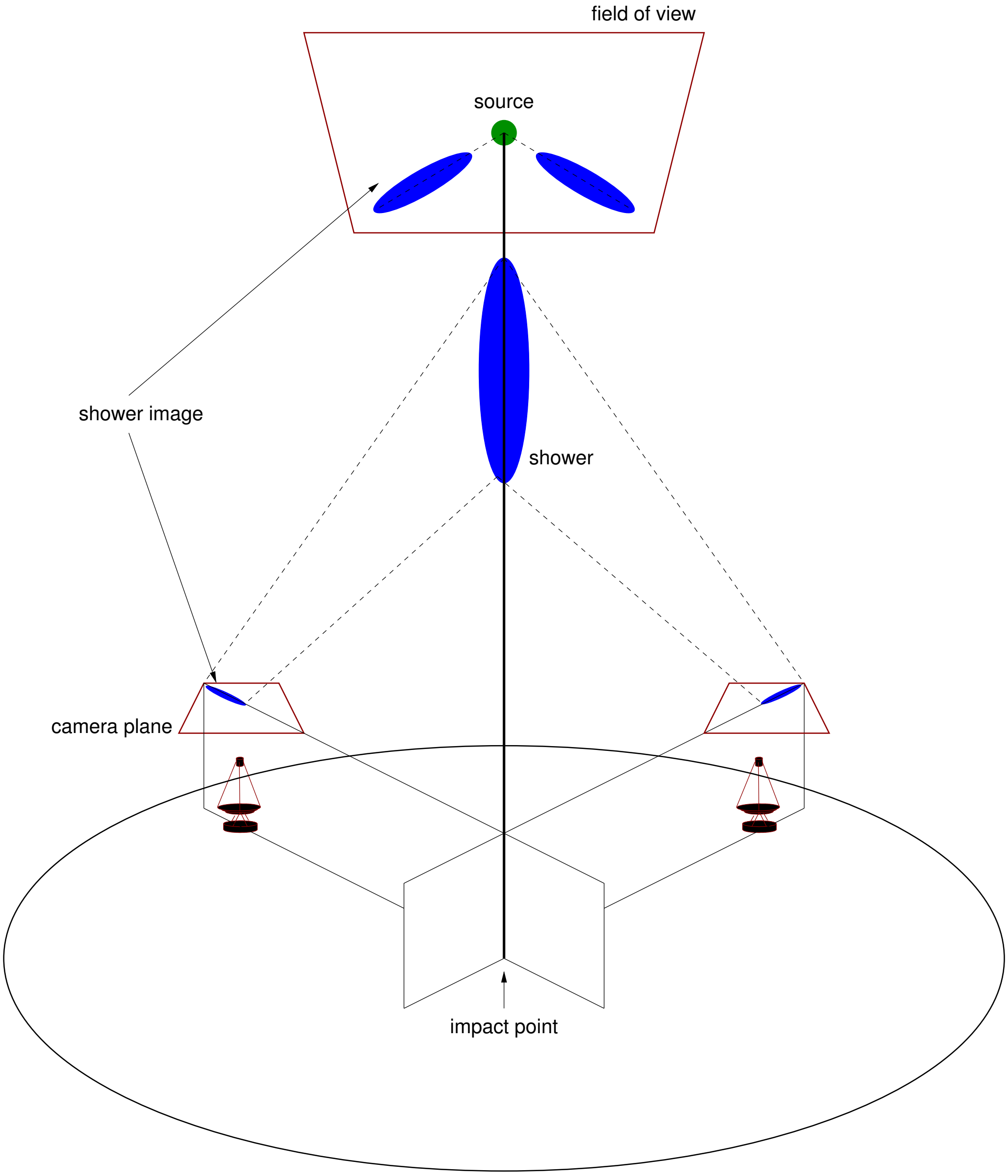

Figure 4.17: **Shower reconstruction.**

protons up to iron as primary particles with energies up to 10^{11} GeV. The package tracks the particle through the atmosphere until it undergoes the next interaction, or in case of unstable secondaries until decay. Hadronic interactions are simulated using the VENUS [Wer93] model. CORSIKA calculates the Cherenkov emission of high energy particles, and the Cherenkov light is propagated through the atmosphere. Based on MODTRAN [AKC+96] different atmospheric models, which are important for the extinction of the Cherenkov light, can be included in the simulation. The standard atmospheric model used in the analysis of H.E.S.S. data is for a desert atmosphere. For a cross-check which will be discussed in chapter 5, simulations of a maritime atmospheric model were used. The detector response to the Cherenkov light is simulated using the sim_hessarray package [Ber03], which is based on sim_telarray, a simulation package developed and used for the HEGRA Cherenkov telescopes. This package ray-traces the Cherenkov light through the optical system (mirrors, Winston cones) to the camera pixels. The reflectivity of the mirror facets were measured and are included in the simulation. The ray-tracing also allows the simulation of shadowing effects of the support structure like the camera masts. Finally, the response of the PMTs and camera electronics is simulated based on the quantum efficiency and the shape of the pulse generated by a photon. Details on the simulations can be found in [Ber03].

The simulation provides the ADC counts for each pixel which can be translated into an intensity. The event building algorithm is applied to the simulated data. The resulting data are used to provide expected shower parameters for the event selection, to calculate the effective areas of the instrument and to estimate the energy of the primary particle based on the observed shower parameters.

4.2.11 Event Selection

The experiment detects two distinct types of showers, electromagnetic showers and hadron induced showers. The bulk of the data are hadronic showers which do not carry any information of the origin of the initial hadron. Hadronic showers are considered as background and should be filtered out before analysis.

The selection of the γ-ray like showers is carried out in two steps. The first step selects images of the individual cameras prior to the shower reconstruction. A maximum cut applied on the locale distance, which is the distance between the centre of gravity of the intensity distribution in the camera and the camera centre, rejects truncated images at the border of the camera. A minimum cut on the image intensity in each camera rejects faint images which would worsen the shower reconstruction. Increasing the cut on the minimum intensity improves the angular resolution while discarding events at the low energy end of the spectrum.

To reduce the hadronic background and enhance the significance of a signal the different widths of electromagnetic and hadronic showers are used. The connection of the actual width of the shower and the measured width of the shower images is influenced by several parameters. Showers of high intensity I_i (in camera i) have a larger width than showers of low intensity. Showers observed at a large zenith angle Θ_{za} or a large impact parameter b_i, which is the distance of the impact point of the shower to telescope i, are further away from the telescope and the Cherenkov light is fainter due to the larger distance. In order to take these effects into account, the Hillas width and length are scaled with the expectation values taken from the simulations. Depending on the image intensity I, the zenith angle Θ_{za} and the impact parameter b the mean expected width $< W > (I, b, \Theta_{\mathrm{za}})$ and the RMS of the expected width $\sigma(I, b, \Theta_{\mathrm{za}})$ are calculated from the simulated data. The observed width W in each telescope is reduced by $< W >$ and scaled with σ. Finally the mean of all telescopes i is calculated, forming the parameter mean reduced scaled width

$$\mathrm{MRSW} = \frac{1}{N_{\mathrm{tel}}} \sum_{i=0}^{N_{\mathrm{tel}}} \frac{W_i - < W > (I_i, b_i, \Theta_{\mathrm{za}})}{\sigma(I_i, b_i, \Theta_{\mathrm{za}})}$$

of the shower. The same calculation is done for the Hillas parameter length, obtaining a mean reduced scaled length, MRSL. Event selection cuts are applied to the mean reduced scaled parameters. As the scaling of the parameter needs the impact distance of the shower, the event selection cut has to be applied after shower reconstruction.

In order to define a region of interest a cut on θ^2, the squared angular distance to the possible source, is performed. This cut defines a circular region around the source which is considered as on-source region.

The cuts used in this work are the standard cuts used for all H.E.S.S. analyses. They were optimised a priori on maximum significance of the signal per $\sqrt{\mathrm{h}}$ using simulated γ-ray data and a background observed at regions of the sky were no γ-ray sources are known. Details on these cuts can be found in [AAB$^+$05b].

In this work the cut configuration referred to as “hard cuts” in [AAB$^+$05b] is used in order to gain a maximum of background rejection. These cuts were optimised for a weak source with a hard spectral index. The simulated source had a flux of 1% of the flux of the Crab Nebula. The Crab Nebula is the standard candle in VHE astronomy and is used for calibration. The

locale distance [m]	[0, 0.525]
intensity [p.e.]	> 200
MRSW	[-2.0, 0.7]
MRSL	[-2.0, 2.0]
θ^2 [deg]^2	≤ 0.01

Table 4.1: **Event selection cuts.** Shown are the cuts which were applied to the parameters mean reduced scaled width and length, MRSW and MRSL, local distance, the intensity of the image in each camera and the squared radial distance to the source θ^2.

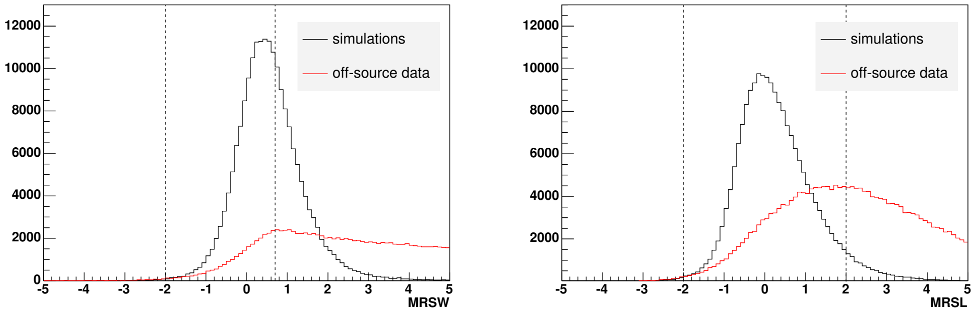

Figure 4.18: **Mean reduced scaled parameters.** Shown are the parameters MRSW (left panel) and MRSL (right panel) for off-source data (red) and γ-ray simulations (black). The applied cuts are denoted by the dashed lines.

differential energy spectrum of the simulated source follows a power law with a spectral index of 2.0. The cuts require a high minimum intensity of the shower images of 200 photo electrons (p.e.) compared to the standard cut of 80 p.e. This cut is meant to reduce the number of background events and to give a narrower point-spread-function (PSF). These advantages are at the expense of a higher energy threshold. The cut parameters are summarised in Table 4.1.

The cut on the mean reduced scaled width (MRSW) is by far the most powerful in the background rejection. Distributions of MRSW are shown in the left panel of Fig. 4.18 for one off-source run, which observed a region in the sky where no γ-ray sources are known, and for γ-ray simulations. Applying the selection cuts on MRSW $[-2.0, 0.7]$ 6% of the off-source events and 40% of the simulated γ-rays were selected.

The distributions of MRSL are shown in the right panel of Fig. 4.18. Applying the selection cuts on the MRSL parameter $[-2.0, 2.0]$ 24% of the off-source events and 61% of the γ-ray simulations were selected.

Applying all cuts 14% of all simulated γ-rays and only 0.11% of the off-source events are accepted.

4.2.12 Energy Estimation

After reconstruction of the showers and selection of the γ-ray like events the energy of the shower can be calculated. The energy of the initial γ-ray is connected with the Cherenkov light emission of the shower. Therefore, the intensities of the shower images are a good parameter for the energy estimation. But this connection is affected by further observation parameters in analogy to what was discussed in the last section. If the shower is further away from the experiment, which is the case for high zenith angle observations or a large impact parameter of the shower, the Cherenkov light is affected by extinction in the atmosphere. The energy of an observed shower is estimated from the energy of simulated showers. The true energies E_{true} of the showers in the simulations are collected in tables depending on the image intensity I in a particular camera and the impact parameter b of the shower to the telescope. The reconstructed energy E_{reco} of a shower is the mean of the true energy E_{true} over all cameras having data:

$$E_{\mathrm{reco}} = \frac{1}{N_{\mathrm{tel}}} \sum_{i=0}^{N_{\mathrm{tel}}} E_{\mathrm{true}}(I_i, b_i).$$

The energy resolution was obtained from the comparison of the energies reconstructed for simulated γ-rays with their true (simulated) energy. The distributions of the relative errors

$$\frac{\Delta E}{E} = \frac{E_{\mathrm{reco}} - E_{\mathrm{true}}}{E_{\mathrm{true}}}$$

after applying event selection cuts are shown in Fig. 4.19. Only those events with a reconstructed energy above the energy threshold were considered. The RMS of this distribution of 21% is considered as the energy resolution.

4.2.13 Effective Areas

In order to calculate a flux of γ-rays per area the effective area of the experiment is needed. The effective area is defined as the area perpendicular to the telescope axis in which the experiment is sensitive to detect γ-rays. It reflects the detection efficiency of the entire experimental setup.

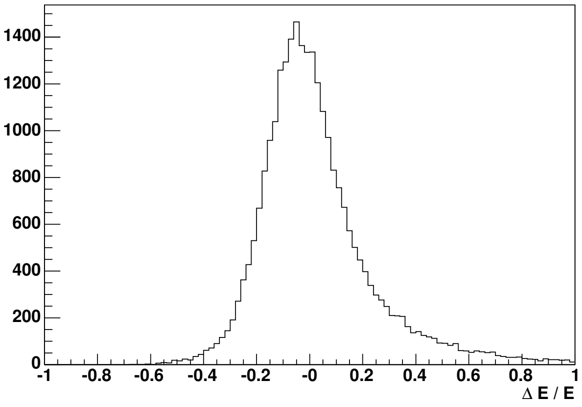

Figure 4.19: **Energy resolution.** The pictures show the relative error on the energy reconstruction as obtained from γ-ray simulations after applying event selection cuts. The width of the distribution is the energy resolution.

In satellites and detectors at collider experiments the detector material has a fixed volume and the sensitive area can be calculated in a straightforward way. The detector material of Cherenkov telescopes, the atmosphere, is a natural resource and does not limit the sensitive area. The sensitive area depends only on the sensitivity of the telescopes to detect showers which are further away from the telescopes. The intensity of the Cherenkov light emitted by a shower is connected to the energy of the primary particle. The Cherenkov light of a high energy shower can be detected at a larger distance while the light of a low energy shower at that distance may be already absorbed in the atmosphere. The effective area also depends on the zenith angle of the observations. At large zenith angles the Cherenkov light has to pass a larger distance through the atmosphere and therefore low energy showers cannot be detected. On the other hand, due to the larger distance the Cherenkov cone has a larger diameter and thus the effective area is increased. The effective areas also depend on the offset of the source to the camera centre. The images of showers with a large offset may be truncated by the edge of the camera and the efficiency is reduced compared to the camera centre. Finally, the effective areas take into account the efficiency of the applied event selection cuts as discussed in section 4.2.11.

The effective areas can be determined only from simulations of the detector response. The effective area can be calculated from the number of showers N_{sim} simulated in an area A_{sim} using

$$A_{\mathrm{eff}} = A_{\mathrm{sim}} \cdot \frac{N_{\mathrm{sel}}}{N_{\mathrm{sim}}}$$

where N_{sel} is the number of simulated events which were selected by the event selection cuts. It is important to choose A_{sim} larger enough to ensure that

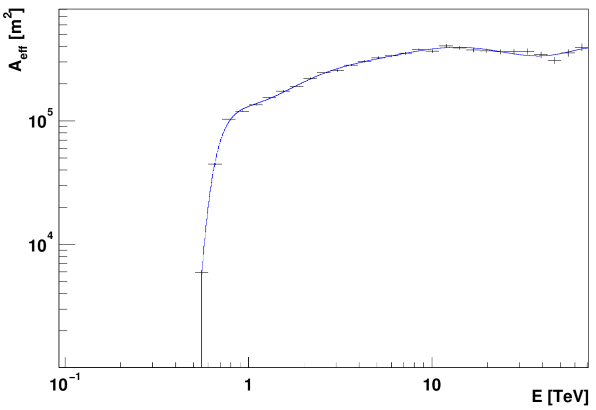

Figure 4.20: **Effective areas.** The histogram shows the effective areas for γ-rays observed at a zenith angle of 45° and an offset of 0.5° after applying all event selection cuts. The blue parameterisation is used to determine the effective area for a particular event.

no shower outside A_{sim} can be detected.

The effective area as a function of the reconstructed energy is shown in Fig. 4.20 for a zenith angle of 45° and an offset of the source direction of the γ-ray to the centre of the camera of 0.5°. The large zenith angle of 45° was chosen for comparison with observations of the Crab Nebula, which is presented in section 4.3. The effective area increases steeply in the region between 500 GeV and 800 GeV. Between 800 GeV and 10 TeV the distribution rises gradually and levels out beyond 10 TeV. For the configuration shown in Fig. 4.20 the effective area reaches a maximum of $0.4\,\text{km}^2$ at an energy of 10 TeV.

For the interpolation of the effective area between the data points shown in Fig. 4.20 the distribution is approximated with a fit of the empirical function

$$A_{\text{eff}}(E) = p_0 \cdot \exp(p_1 E) + p_2 E^4 + p_3 E^3 + p_4 E^2 + p_5 E + p_6$$

to the distribution. The fit is denoted by the blue line in Fig. 4.20. The number of photons per area in an energy bin $[E, E + \Delta E]$ can be calculated by the sum of all events i in this range weighted with the inverse of $A_{\text{eff}}(E)$:

$$N(E, E + \Delta E) = \sum_{E_i \in [E, E+\Delta E]} \frac{1}{A_{\text{eff}}(E_i)}.$$

4.2.14 Energy Threshold

Most of the energy spectra observed in VHE astronomy follow a power law. In the low energy range high fluxes are expected but the effective areas are low. For higher energies the telescopes have a high effective area but the

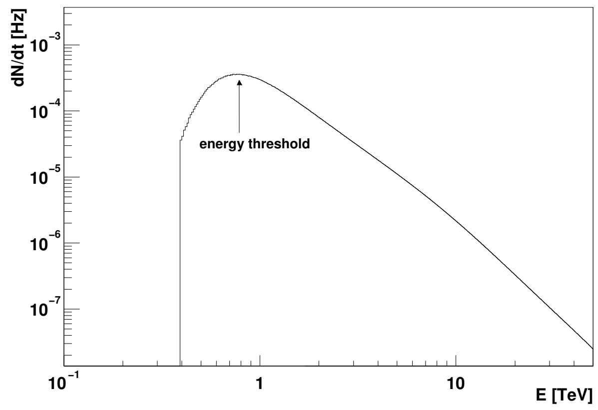

Figure 4.21: **Differential γ-ray rate.** The histogram shows the expected γ-ray rate from the Crab Nebula after applying event selection cuts. The size of each bin is $\Delta E = 8\,\mathrm{GeV}$. The energy threshold is indicated by an arrow.

expected flux is low. In order to describe this quantitatively, the differential γ-ray rate is investigated.

Assuming a flux of γ-rays which follows a power law

$$\varphi(E) = \frac{\mathrm{d}\Phi}{\mathrm{d}E} = \varphi_{1\,\mathrm{TeV}} \cdot \left(\frac{E}{1\,\mathrm{TeV}}\right)^{-\Gamma}$$

with parameters comparable to the spectrum of the Crab Nebula, $\varphi_{1\,\mathrm{TeV}} = 2.9 \times 10^{-11}\,\mathrm{TeV}^{-1}\mathrm{cm}^{-2}\mathrm{s}^{-1}$ and $\Gamma = 2.7$. The γ-ray rate expected in the energy range $[E, E + \Delta E]$ can be calculated as

$$\begin{aligned}\frac{\mathrm{d}N}{\mathrm{d}t}(E, \Delta E) &= \int_{E}^{E+\Delta E} A_{\mathrm{eff}}(E)\varphi_{1\,\mathrm{TeV}} \left(\frac{E}{1\,\mathrm{TeV}}\right)^{-\Gamma} \mathrm{d}E \\ &\approx A_{\mathrm{eff}}(E)\varphi_{1\,\mathrm{TeV}} \left(\frac{E}{1\,\mathrm{TeV}}\right)^{-\Gamma} \Delta E.\end{aligned}$$

The distribution is shown in Fig. 4.21 for a zenith angle of 45° and a camera offset of 0.5°. It can be seen that the distribution reaches a maximum at 790 GeV, which is defined as the energy threshold. The threshold is relatively large compared to the design of H.E.S.S. which should detect γ-rays above 100 GeV. The relatively large zenith angle results in an increased threshold. Additionally, hard image size cuts are applied, which require camera images with intensities of at least 200 p.e. This cut already rejects low energy events during the event selection and further increases the energy threshold. Events below the energy threshold can be detected and reconstructed, but due to the low efficiency in this region the errors on the flux are relatively large. For the calculation of a significance of the detection all events will be considered but only events above the threshold are used for the spectral analysis.

4.2.15 Angular Resolution

The accuracy or resolution of the reconstructed shower direction is an important point in the analysis. A good resolution improves the determination of the source coordinates of point sources and it gives the minimal size of features of extended sources which can be resolved.

The angular resolution can be inferred from the simulation of the detector response to a point source. Figure 4.22 shows the distribution of the squared angular distance θ^2 of the reconstructed shower direction from the simulated direction after applying event selection cuts. This distribution, called the point-spread function (PSF), can be approximated with a double Gaussian function [AAB⁺05b], where one Gaussian denotes the peak and the second Gaussian describes the long tail of the distribution:

$$f_{\mathrm{PSF}}(\theta^2) = A\left(\exp\left(\frac{-\theta^2}{2\sigma_1^2}\right) + A_{\mathrm{rel}}\exp\left(\frac{-\theta^2}{2\sigma_2^2}\right)\right). \tag{4.1}$$

Here, σ_1 and σ_2 denote the standard deviations of the two Gaussians, A_{rel} is the ratio of the amplitudes of the two Gaussians and A is a normalisation factor. This function was fit to the simulated data, the fit parameters are summarised in Table 4.2. The fit is only of reasonable quality.

The angular resolution is in the order of 0.1°. It should be noted that the angular resolution depends on the photon energy. In the simulations used here the differential photon flux follows a power law with spectral index 2.0. The parameters of the PSF could deviate from the values presented here for significantly different photon spectra.

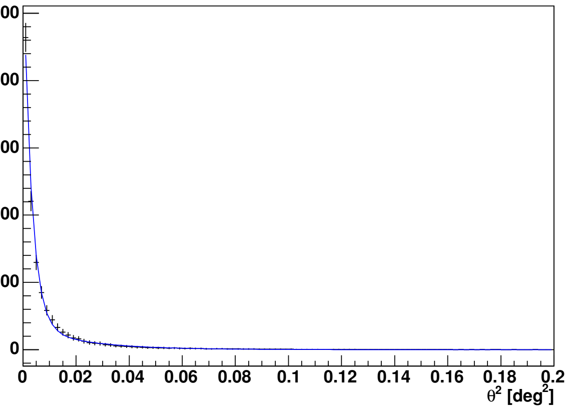

Figure 4.22: **Angular distribution of simulated γ-ray events.** The events were simulated for a point-like source at a zenith angle of 45° and an offset to the camera centre of 0.5° and event selection cuts are applied. The blue line represents the PSF.

A	37 ± 9
σ_1	$0.103° \pm 0.007°$
A_{rel}	15 ± 4
σ_2	$0.039° \pm 0.002°$
resolution (68%)	0.09°

Table 4.2: **Fit parameters of the Point Spread Function after event selection.** The resolution is the radius of a circle around a point source containing 68% of the events.

4.3 Verifying the Analysis Technique

A sample analysis of the standard candle in γ-ray astronomy — the Crab Nebula — will be presented in this section. The Crab Nebula consists of a pulsar within a plerionic supernova remnant. It is an ideal standard candle because of its bright and steady emission. It was detected by all experiments observing in the VHE energy range, therefore a variety of reference data exist. The purpose of the analysis presented here is to verify the analysis chain used in this work and to present the performance of the H.E.S.S. experiment.

4.3.1 Data Set

The data presented here is a subset of Crab observations taken since 2003. A complete analysis of this data and a discussion of the detector performance can be found in **(author?)** [AAB$^+$05b]. Here only the data taken with the full 4-telescope array are used (data set IV in [AAB$^+$05b]). The data were taken in November and December of 2004 and consist of 17 runs with a typical duration of 28 min. The observations were performed in wobble mode, with a deviation of the source position from the telescope axis of ±0.5° in declination or ±0.54° in right ascension (in the following called low offset runs), or ±1.6° in right ascension (large offset runs). The dead-time corrected exposure time (live time) is 6.8 h. The data were taken at zenith angles between 44° and 55° with a mean of 48°.

Only those data passing quality checks were considered for analysis. The quality criteria require a stable tracking, a minimum of problematic pixels in each camera and a constant trigger rate. The standard H.E.S.S. calibration, event selection and reconstruction techniques as described in sections 4.2.8, 4.2.9 and 4.2.11 were applied.

A list of the used runs along with typical run parameters is given in Table A.1.

4.3.2 Background Estimation

As the γ-ray emission of the Crab Nebula is point-like the background can be estimated from the same field of view. Circular regions of 0.9° diameter were chosen for both on-source and background (off-source) regions. In case of the small offset runs, the background has been estimated in each run from a region mirrored at the camera centre. The on-source regions and the positions of the off-source regions are shown in the left panel of Fig. 4.23. The two background regions west of the Crab Nebula belong to different runs with a slightly different offset. The large offset runs allow the use of 9 off-source

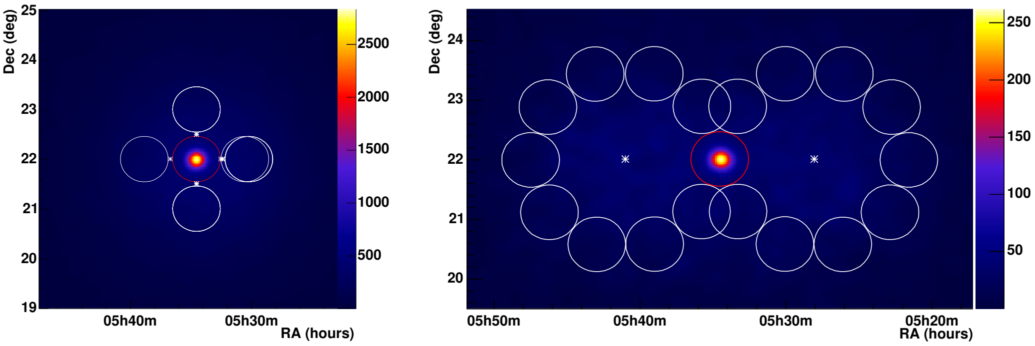

Figure 4.23: **Crab off-source regions.** The picture shows the sky maps of the γ-ray like events obtained in the small offset runs (left panel) and large offset runs (right panel). The on-source regions are marked with red circles. The off-source regions are marked with white circles. The observation positions are denoted by asterisks. The sky maps are smoothed and thus the colour bars denote arbitrary counts.

regions. The off-source regions were arranged in a circle around the camera centre such that they have the same offset to the camera centre as the on-source region and no correction for the camera acceptance is necessary. The right panel of Fig. 4.23 shows the on-source region and off-source regions for the large offset runs. The seemingly overlapping background regions north and south of the source are in fact independent as they belong to different runs.

The number of excess events in all runs can be calculated from the number of on-source events, $N_{\mathrm{on},i}$, the number of off-source events, $N_{\mathrm{off},i}$ and the number of background regions, $N_{\mathrm{bg},i}$, in each run i:

$$N_{\mathrm{ex}} = \sum_i N_{\mathrm{on},i} - \sum_i \frac{N_{\mathrm{off},i}}{N_{\mathrm{bg},i}}.$$

The excess can also be calculated from the total number of detected on-source and off-source events, $N_{\mathrm{on}} = \sum_i N_{\mathrm{on},i}$ and $N_{\mathrm{off}} = \sum_i N_{\mathrm{off},i}$ respectively. This is required for the calculation of the significance according to **(author?)** [LM83]. The excess calculated from N_{on} and N_{off} is

$$N_{\mathrm{ex}} = N_{\mathrm{on}} - \alpha N_{\mathrm{off}}.$$

with a scaling factor

$$\alpha = \frac{\sum_i N_{\mathrm{off},i}/N_{\mathrm{bg},i}}{\sum_i N_{\mathrm{off},i}}. \tag{4.2}$$

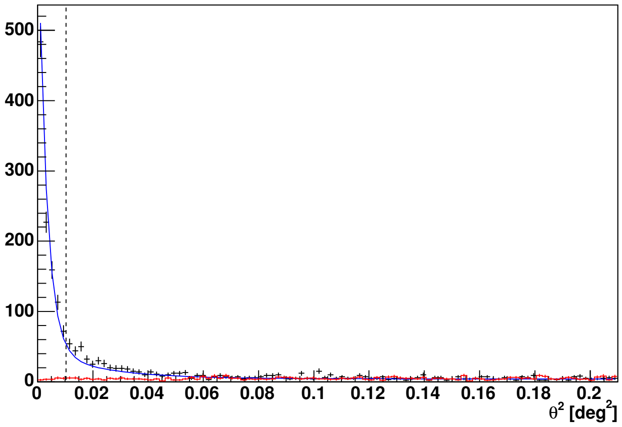

Figure 4.24: **Angular distribution of γ-rays from the Crab Nebula.** The black data points denote the on-source events, the red histogram denotes the scaled off-source events. The event selection has been applied. The blue line is the result of a fit of the PSF (including a constant term for the background) where only the parameter A was varied freely. The dashed line represents the applied θ^2 cut of $0.01\,\mathrm{deg}^2$.

4.3.3 Signal and Sensitivity

The angular distribution of the γ-ray like events from the direction of the Crab Nebula is shown in the θ^2-plot in Fig. 4.24. The angle θ is the distance between the γ-ray and the nominal source position (RA 5h34min32s, Dec $22°0'52''$) which was obtained from radio observations [HT99]. The background was estimated from the off-source regions and scaled according to equation (4.2). The applied θ^2 cut is denoted by a dashed line. This cut represents a circular region around the nominal source position with a radius of 0.1°. Within this region a clear excess of γ-rays of 1020 ± 30 events is obtained. The statistical significance of the signal, calculated using the likelihood ratio method of **(author?)** [LM83, eq. 17], is $40\,\sigma$. Using the cuts applied here, H.E.S.S. can detect sources with a flux similar to that of the Crab Nebula with a significance of $5\,\sigma$ within 6 minutes. All results are summarised in Table 4.3.

The blue line in Fig. 4.24 is the result of fits of the PSF (eq. 4.1) with an additional constant term for the background where only the parameter A was varied freely. The fit is of good quality ($\chi^2/\mathrm{ndf} = 119.7/99$), indicating that it is reasonable to consider the Crab Nebula as a point-source for H.E.S.S.

number of on-source events	1036
number of off-source events	26
off-source scaling factor α	0.69
number off excess events	1020 ± 30
significance	$40\,\sigma$
live time [s]	24757
γ-ray rate [min^{-1}]	2.5 ± 0.1
significance gain	$15.3\,\sigma/\sqrt{\mathrm{h}}$
RA	$5\mathrm{h}34\mathrm{m}30.^{\mathrm{s}}8 \pm 0.^{\mathrm{s}}4$
Dec	$22^\circ 0'(33 \pm 6)''$
energy threshold	$0.79\,\mathrm{TeV}$
$\varphi_{1\,\mathrm{TeV}}$ [$10^{-11}\,\mathrm{TeV}^{-1}\mathrm{cm}^{-2}\mathrm{s}^{-1}$]	3.5 ± 0.2
Γ	2.81 ± 0.05
$\Phi(E > 1\,\mathrm{TeV})$ [$10^{-11}\,\mathrm{cm}^{-2}\mathrm{s}^{-1}$]	1.9 ± 0.1
χ^2/ndf	9.0/12

Table 4.3: **Results of the Crab observations.**

4.3.4 Position Reconstruction

The previous section showed that an excess of γ-rays at the nominal position of the Crab Nebula can be obtained. For the analysis of unknown sources and the morphology of extended sources it is important that the correct position of the source can be reconstructed. Figure 4.25 shows a sky map of the excess in the direction of the Crab Nebula. The sky map was obtained by subtracting the normalised off-source events from the on-source events. From this sky map the position of the γ-ray excess is calculated.

The squared angular distance to the source is

$$\theta^2(\mathrm{RA}, \mathrm{Dec}) = (\mathrm{RA} - \langle\mathrm{RA}\rangle)^2 \cdot \cos^2(\mathrm{Dec}) + (\mathrm{Dec} - \langle\mathrm{Dec}\rangle)^2$$

where RA and Dec are the coordinates of a bin and <RA> and <Dec> denote the position of the source in right-ascension and declination. The correction factor cos(Dec) calculates the angle parallel to the right-ascension axis. One can write the PSF (eq. 4.1) in two dimensions as

$$f(\mathrm{RA}, \mathrm{Dec}) = A_0 \left(\exp\left(\frac{-\theta^2}{2\sigma_1^2} \right) + A_{\mathrm{rel}} \exp\left(\frac{-\theta^2}{2\sigma_2^2} \right) \right).$$

The position of the source can be obtained by a fit of $f(\mathrm{RA}, \mathrm{Dec})$ to the

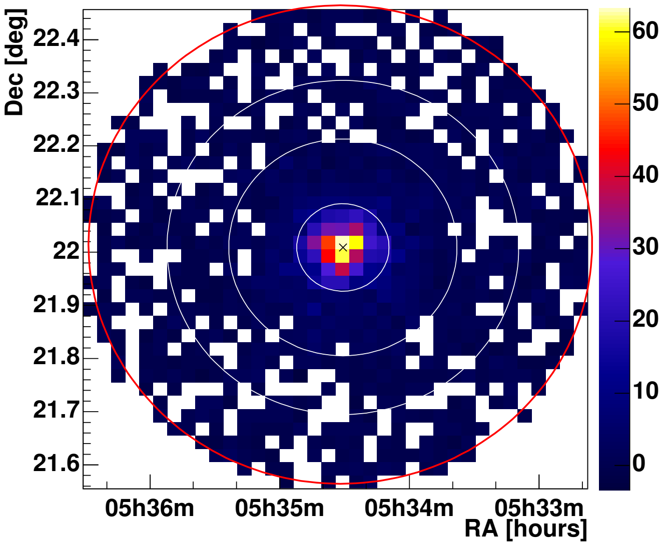

Figure 4.25: **Excess Map of the Crab data.** The colour bars denote numbers of excess events. The white contours denote circles containing 68.3%, 95.5% and 99.7% of the events of the point spread function fit. The best fit position of the sources is denoted by the cross. The red circle denotes the on-source region as in Fig. 4.23.

sky map shown in Fig. 4.25. In the fit the parameters σ_1, σ_2, A_0[1] and A_{rel} were fixed to those values obtained from simulations (Table 4.2). Since due to the low statistics not all bins are filled (white bins within the red circle in Fig. 4.25), a likelihood minimisation was chosen. The obtained position is marked with a cross, the result is shown in Table 4.3. The systematic error of the mechanical pointing is 30″ [Gil03, Gil04]. The obtained result is compared the result of **(author?)** [Gil04] based on H.E.S.S. data and the measurement by the HEGRA collaboration [AAB+04] in Fig. 4.26. The position of the Crab Nebula can be reconstructed with good accuracy.

4.3.5 Differential Energy Spectrum

The differential energy spectrum of γ-rays from the Crab Nebula is shown in Fig. 4.27. The solid line denotes the result of a fit of a power law

$$\frac{\mathrm{d}\Phi}{\mathrm{d}E} = \varphi_{1\,\mathrm{TeV}} \cdot \left(\frac{E}{1\,\mathrm{TeV}}\right)^{-\Gamma}$$

to the data with the flux normalisation at 1 TeV, $\varphi_{1\,\mathrm{TeV}}$ and the spectral index Γ. The fit is of very good quality and the resulting parameters are

---

[1] Note that the parameters A for the 1-dimensional PSF and A_0 for the 2-dimensional PSF differ by a factor of $A_0/A = 0.099$. This factor is due to the different areas covered by the θ^2 bins and the sky bins.

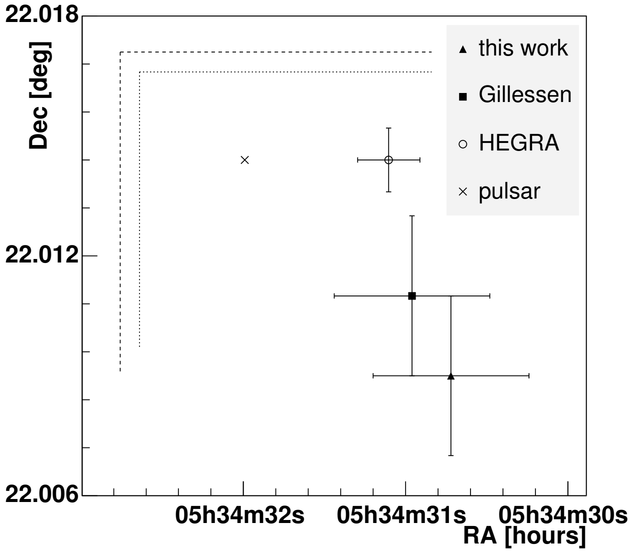

Figure 4.26: **Reconstructed positions of the Crab Nebula.** Shown are the best fit positions obtained in this work, a previous measurement using H.E.S.S. data [Gil04] and the position as published by HEGRA [AAB⁺04]. The nominal position of the pulsar [HT99, from radio measurements] is denoted by the cross. The error bars are $1\,\sigma$ statistical errors, the systematic uncertainties are denoted by the dashed (H.E.S.S.) and dotted (HEGRA) lines.

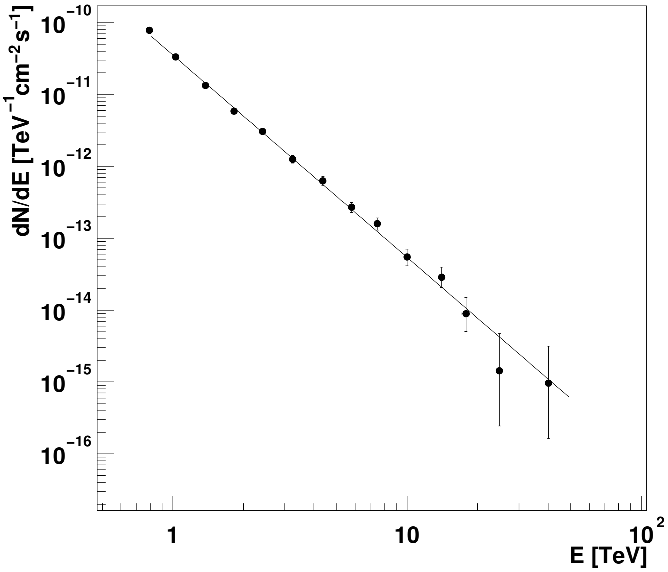

Figure 4.27: **Differential energy spectrum of the Crab Nebula.** The solid line is the result of a power-law fit.

summarised in Table 4.3. From these parameters the integral flux above 1 TeV, defined as

$$\Phi(E > 1\,\mathrm{TeV}) = \int\limits_{1\,\mathrm{TeV}}^{\infty} \varphi_{1\,\mathrm{TeV}} \cdot \left(\frac{E}{1\,\mathrm{TeV}}\right)^{-\Gamma} \mathrm{d}E, \tag{4.3}$$

can be calculated to be $(1.9 \pm 0.1) \times 10^{-11}\,\mathrm{cm}^{-2}\mathrm{s}^{-1}$. The results are in a very good agreement with preliminary results obtained with the same configuration by **(author?)** [AAB+05b]. The systematic uncertainties of the obtained spectral parameters are 0.1 for the spectral index Γ and 20% on the fluxes [AAB+05b].

Figure 4.28 shows the flux normalisations and spectral indices of different measurements in comparison. The H.E.S.S. data was obtained from the southern hemisphere, while the other experiments are on the northern hemisphere. Therefore, H.E.S.S. observations were carried out at a larger zenith angle resulting in a higher energy threshold. Additionally, a hard image size cut was used in the analysis of the H.E.S.S. data which further increases the energy threshold. The slightly larger spectral index obtained by H.E.S.S. could arise from the higher energy threshold if the spectrum of the Crab Nebula would become steeper at higher energies. The current data gives a hint for a steepening of the spectrum at higher energies which is currently under investigation [MBv05, AAB+05b].

4.3.6 Conclusion

It has been shown that H.E.S.S. can detect the Crab Nebula with high significance. The energy spectrum in the range between 780 GeV and 40 TeV and the position in the sky can be reconstructed. Sources with a photon flux in the order of the flux from the Crab Nebula can be detected with a significance of $5\,\sigma$ within 6 minutes. The direction of a single γ-ray can be reconstructed with an angular resolution of 0.09°, and the energy of the γ-rays can be calculated with an accuracy of $\approx 20\%$. H.E.S.S. is thus an ideal instrument for the observation of γ-ray sources.

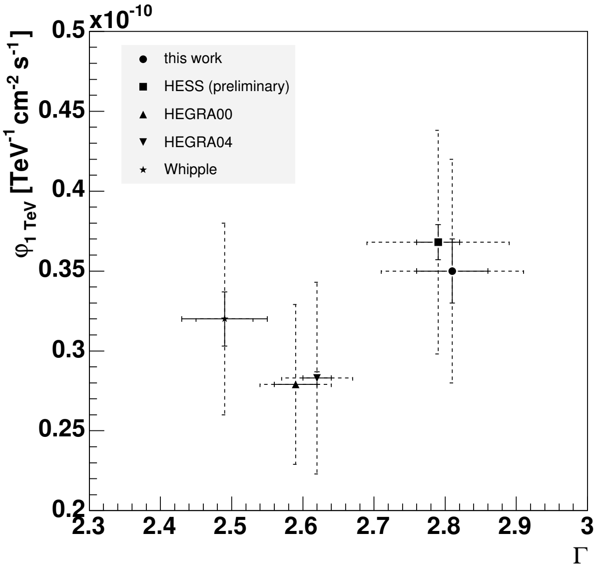

Figure 4.28: **Comparison of the Crab spectra.** Shown are the flux normalisation $\varphi_{1\,\mathrm{TeV}}$ and the spectral index Γ obtained in this work, preliminary H.E.S.S. results by **(author?)** [AAB$^+$05b] and the previous results by HEGRA [AAB$^+$00, AAB$^+$04] and Whipple [HAB$^+$98]. The solid bars denote $1\,\sigma$ statistical errors, the dashed bars denote the systematic uncertainties.

Chapter 5

Observations of RX J0852.0−4622

We have seen that H.E.S.S. is an ideal instrument for the observation of γ-ray sources. The shell-type supernova remnant RX J0852.0−4622 as a source of synchrotron emission is a candidate for γ-ray emission and the acceleration of cosmic rays. In this chapter the observation of RX J0852.0−4622 with H.E.S.S. and the analysis of this data are presented. The existence of γ-ray emission will be proved for the entire remnant, and a differential photon energy spectrum will be reconstructed for the entire remnant. The morphology of the γ-ray emission will be compared with X-ray measurements. Additionally, dedicated parts of the remnant will be analysed — the CANGAROO emission region and the compact central source. The systematic uncertainties of the measurement will be discussed in detail. A short discussion of the observations concludes this chapter.

5.1 Data Set

5.1.1 On-Source Data

RX J0852.0−4622 has been observed with the H.E.S.S. telescopes for 4.5 h in February 2004. In total, 9 runs have been taken in wobble mode, with observation positions deviating ±0.5° in declination from the nominal source position (RA 8h$52^{\mathrm{m}}.0$, Dec $-46°22'$ [Asc98]). One run did not pass the run quality selection due to passing clouds (the trigger rate and radiometer temperature of this run are shown in the left panel of Fig. 4.11 and discussed in section 4.2.6). The remaining 8 runs which were used in the analysis have a total, dead time corrected exposure time (live time) of 3.16 h. Data with

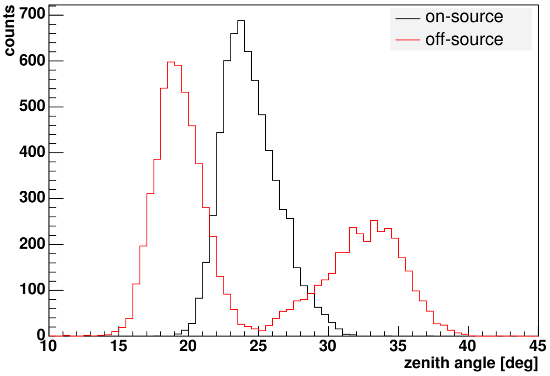

Figure 5.1: **Zenith angle distribution of on-source and off-source data.**

1.95 h of live time (62% of the total live time) were taken at the wobble position Dec +0.5°, 1.21 h (38% of the total live time) at the wobble position Dec −0.5°. Technical problems with the newly installed telescope CT1 did not allow to use the data of this telescope. Therefore, the showers were reconstructed using the data of the three remaining telescopes only. The zenith angle distribution of the data is shown in Fig. 5.1. The distribution is very narrow and thus all runs have a comparable energy threshold. The mean of the distribution is 24.5° which is smaller than the zenith angle of 45° discussed in chapter 4. A summary of the parameters of the individual runs is given in Table A.2.

5.1.2 Off-Source Data

Due to the large extension of RX J0852.0−4622 of 2°, it is not possible to estimate the background from the same field of view. The background level has to be estimated from observations of sky regions without γ-ray sources. In the initial observation period, no dedicated off-source runs have been taken for RX J0852.0−4622. For the determination of the background off-source runs taken for the supernova remnant RX J1713.7−3946 were used.

RX J1713.7−3946 was observed with H.E.S.S. between April and June 2004 including dedicated off-source runs at two different positions. The observation positions off the off-source runs are (RA 16h43m33$^{\mathrm{s}}$.59, Dec −39°45′44″, pos 1) and (RA 17h43m33$^{\mathrm{s}}$.59, Dec −39°45′44″, pos 2). A sample of off-source runs with good weather quality and a mean zenith angle comparable to the on-source data of RX J0852.0−4622 were chosen, a summary of the runs can be found in Table A.3. The total live time of the off-source runs is 4.71 h. The zenith angle distribution is shown in Fig. 5.1. The mean value of 24.6° corresponds to the mean value of the on-source data. The

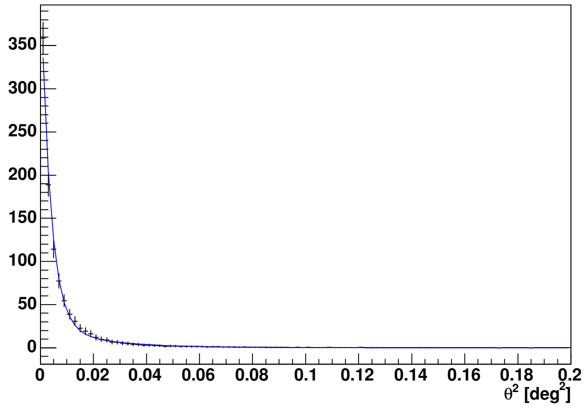

Figure 5.2: **Radial distribution of simulated γ-ray events.** The events were simulated for a point-like source at a zenith angle of 20° and an offset to the camera centre of 0.5°. The blue line represents the PSF.

distribution has two maxima at lower and higher zenith angles than those of the on-source data. Systematic uncertainties arising from this fact will be estimated in section 5.8.2.

5.2 Analysis

For the analysis of the data, the calibration, image cleaning and event reconstruction methods discussed in chapter 4 were applied. There are some differences between the observations of RX J0852.0−4622 and the Crab Nebula. The zenith angle of the observations of RX J0852.0−4622 is lower and one telescope needed to be excluded from the analysis. Additionally, the large extension of RX J0852.0−4622 does not allow to estimate the background from the on-source runs.

5.2.1 Angular Resolution

Figure 5.2 shows the angular distribution of simulated events for a point source at a zenith angle of 20° after applying event selection cuts. The point spread function (eq. 4.1) was fit to the distribution. The obtained parameters are summarised in Table 5.1. The angular resolution, the radius of a circle containing 68% of all events, is 0.09°, comparable to the angular resolution of the Crab observations.

The use of an integration radius of 0.1° in the correlated sky maps is based on the optimisation of the θ^2 cut on maximal significance per $\sqrt{\mathrm{h}}$ for a point source and is in the order of the angular resolution of the instrument.

A	30 ± 10
σ_1	$0.10^\circ \pm 0.01^\circ$
A_{rel}	15 ± 7
σ_2	$0.043^\circ \pm 0.003^\circ$
resolution (68%)	0.09°

Table 5.1: **Fit parameters of the Point Spread Function.** The resolution is the radius of a circle containing 68% of the events.

5.2.2 Energy Threshold

Due to the smaller zenith angle of the RX J0852.0−4622 observations compared to the Crab observations a lower energy threshold is expected. Figure 5.3 shows the differential γ-ray rate expected from a point source of the strength of the Crab Nebula at a zenith angle of 20°. The energy threshold is 350 GeV which is is lower than the threshold for Crab observations of 790 GeV and allows a spectral analysis of RX J0852.0−4622 over a wider energy range.

5.2.3 Background Estimation

A sky map of the on-source data after applying event selection cuts is shown in Fig. 5.4. The sky map is shown in correlated bins, at each bin position the events in a circular region with a radius of 0.1° are integrated, the size of the integration region is denoted by the white circle. The integration radius is obtained from the optimisation of the angular cut on point source simulations. The acceptance of the cameras drops off toward the edge of the cameras. Therefore, the distribution of the events is not uniform. High statistics of events around the observation positions can be seen in Fig. 5.4. The observation positions are marked with crosses. A ring-like structure near the centre of Fig. 5.4 can be seen, but the data are dominated by the background making a background subtraction necessary.

In the bottom row of Fig. 5.5 the sky maps of the off-source data at the different observation positions after applying event selection cuts are shown. From these sky maps the background level at the on-source observation position was estimated.

When estimating the background from off-source data, several things have to be taken into account. The off-source data were taken at different sky positions than the on-source data and the on-source data is a superposition of two wobble offsets. The off-source data (shown in the bottom row of Fig 5.5) must be moved such that the observation position (denoted by the crosses) matches one of the observation positions of the on-source data (top of

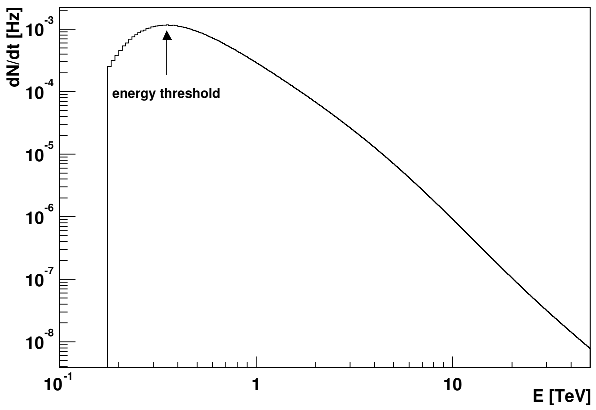

Figure 5.3: **RX J0852.0−4622 energy threshold.** The histogram shows the γ-ray rate expected from a point source with the spectral index of the Crab Nebula to be obtained at a zenith angle of 20° and an offset to the camera centre of 0.5°. The energy threshold is indicated by the arrow.

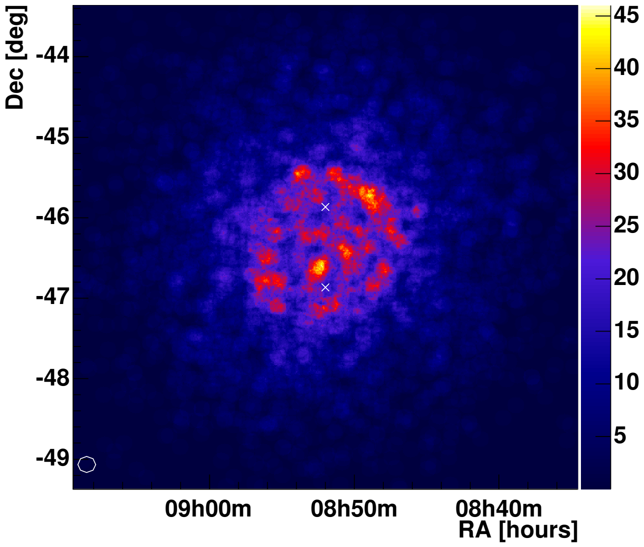

Figure 5.4: **Sky map of RX J0852.0−4622 on-source data.** This picture shows the VHE γ rays from the direction of RX J0852.0−4622 (on-source data). The bins are correlated, integrating the events in a circle with radius 0.1° which is denoted by the white circle. The observation positions are marked with crosses. The colour bar denotes the number of counts.

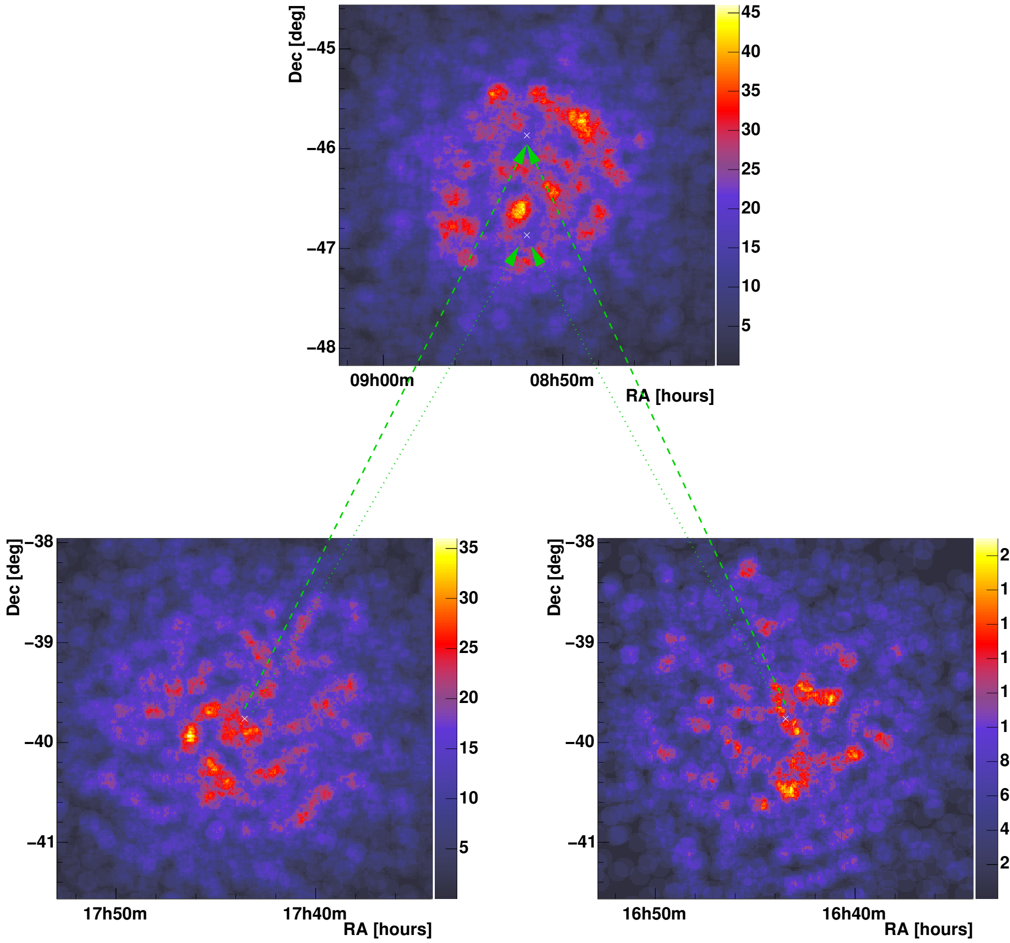

Figure 5.5: **Background construction.** Sky Maps of the on-source data (top) and off-source data (bottom) after applying event selection cuts are shown. The crosses denote the observation positions. The arrows indicate the construction of the background. 62% of the off-source events are assigned to the wobble $+0.5°$ position (dashed arrow) and 38% to the wobble $-0.5°$ position (dotted arrow).

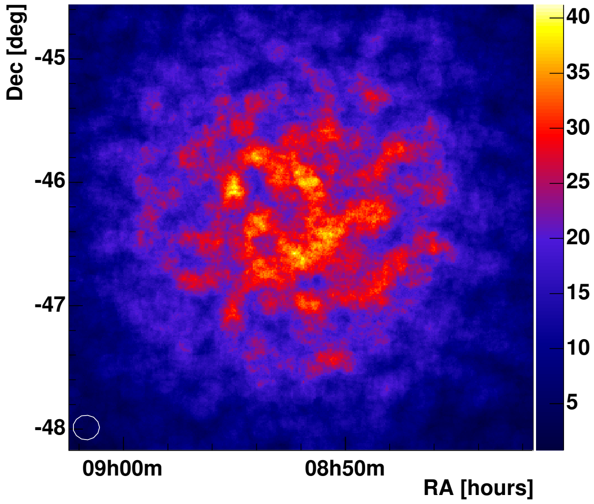

Figure 5.6: **Sky map of RX J0852.0−4622 background data.** The background was obtained using the method illustrated in Fig. 5.5. The bins are correlated (0.1°, white circle), the colour bar denotes the number of counts.

Fig. 5.5). In order to consider the different offsets of the on-source data with the appropriate live time, each off-source event has been counted twice, with a weight $w = 0.62$ at the wobble $+0.5°$ position (dashed arrow in Fig 5.5) and a weight $w = 0.38$ at the wobble $-0.5°$ position (dotted arrow in Fig 5.5). The error on the $N_{\text{off}} = \sum_{i=1}^{N} w_i$ off-source counts in a certain sky bin has been calculated to be

$$\Delta N_{\text{off}} = \sqrt{\sum_{i=1}^{N} w_i} = \sqrt{N_{\text{off}}}$$

to avoid underestimation of the error by counting the events twice. A sky map of the resulting background is shown in Fig. 5.6. The coordinates of the background events are at the position of RX J0852.0−4622 and the off-source data cover the two wobble observation positions.

The background estimation for the spectrum determination was made differently. Each event was counted only once with a weight $w = 1$. A fraction of 62% of all off-source events were assigned to the wobble $+0.5°$ position and 38% of all events to the wobble $-0.5°$ position.

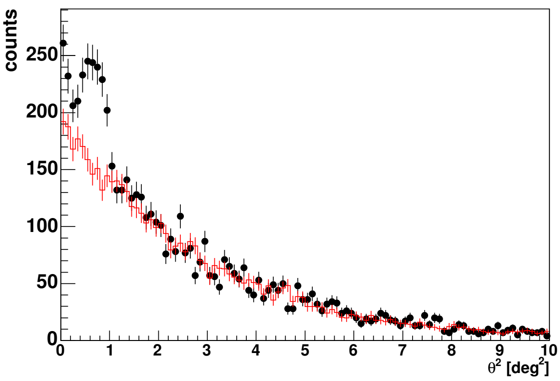

Figure 5.7: **Radial distribution of the RX J0852.0−4622 data.** The on-source data is shown as data points. The histogram denotes the off-source data normalised according to the live time. The angle θ is the angular distance of the γ-ray direction from the centre of the supernova remnant.

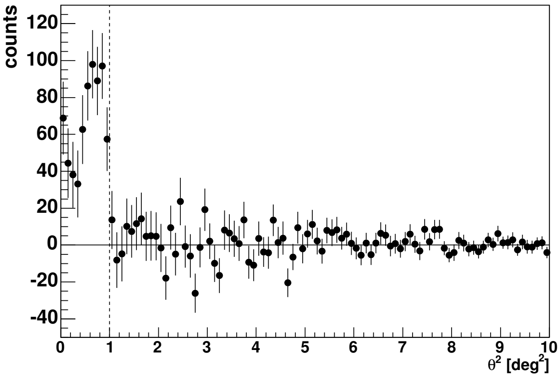

Figure 5.8: **Radial Distribution of the RX J0852.0−4622 excess.** The plot shows the distribution of the excess of γ-rays as function of the angular distance from the direction of the centre of the SNR. The applied θ^2 cut ($\theta^2 < 1\,\mathrm{deg}^2$) is denoted by the dashed line.

5.3 Results for the Entire SNR

5.3.1 Detection of the Signal

Figure 5.7 shows the on- and off-source counts as a function of θ^2, where θ is the angular distance of the events from the centre of the SNR at (RA 8h52$.^{\rm m}$0, Dec $-46°22'$). The good agreement of on- and off-source data in the region outside the SNR ($\theta^2 > 1\text{deg}^2$) justifies the use of the chosen background. The distributions are not flat as the instrument's acceptance drops toward the edge of the field of view. In the region $\theta^2 \leq 1\text{deg}^2$ a clear excess of events can be seen. The radial distribution of the excess, obtained by subtracting the live-time normalised background from the on-source events, is pictured in Fig. 5.8. According to the extension of the SNR as seen in X-rays, a circular region with a radius of 1° represented by a cut $\theta^2 \leq 1\text{deg}^2$ was chosen. Within this region 2302 on-source events and 2425 off-source events were found. The scaling factor α is the ratio of the live times τ of the on-source data and off-source data, $\alpha = \tau_{\rm on}/\tau_{\rm off}$. The excess can be calculated using

$$N_{\rm ex} = N_{\rm on} - \alpha \cdot N_{\rm off},$$

$$\Delta N_{\rm ex} = \sqrt{N_{\rm on} + \alpha^2 \cdot N_{\rm off}}$$

to be 670 ± 60 events. The statistical significance of the signal according to **(author?)** [LM83, eq. 17] is $11.9\,\sigma$. The obtained values are summarised in Table 5.2.

5.3.2 Spectrum

From the excess of γ-rays a differential photon flux spectrum was obtained which is shown in Fig. 5.9. The individual data points for the different bins are summarised in Table 5.3. The energy given for each bin is the mean energy of all events in this bin. The error on the energy is one standard deviation, obtained by dividing the RMS by the square root of the number of events in this bin. The last data point does not have enough statistics to calculate a flux. An upper limit with 99.9% confidence level (C.L.) was calculated using the unified approach for small signals of **(author?)** [FC98].

The spectrum can be described by a power law

$$\varphi(E) = \frac{\mathrm{d}\Phi}{\mathrm{d}E} = \varphi_{1\,\mathrm{TeV}} \cdot \left(\frac{E}{1\,\mathrm{TeV}}\right)^{-\Gamma}.$$

The obtained results from a χ^2 minimisation fit, without taking the upper limit into account, are summarised in Table 5.2. The integral flux above

number of on-source events	2302
number of off-source events	2425
off-source scaling factor α	0.671
number off excess events	670 ± 60
significance	$11.9\,\sigma$
live time (on) [s]	11368
γ-ray rate [min^{-1}]	3.5 ± 0.3
significance gain	$6.7\,\sigma/\sqrt{\mathrm{h}}$
energy threshold	0.35 TeV
$\varphi_{1\,\mathrm{TeV}}$ [$10^{-11}\,\mathrm{TeV}^{-1}\mathrm{cm}^{-2}\mathrm{s}^{-1}$]	2.1 ± 0.2
Γ	2.1 ± 0.1
$\Phi(E > 1\,\mathrm{TeV})$ [$10^{-11}\,\mathrm{cm}^{-2}\mathrm{s}^{-1}$]	1.9 ± 0.2
χ^2/ndf	4.3/4

Table 5.2: **Results for the entire SNR RX J0852.0−4622.**

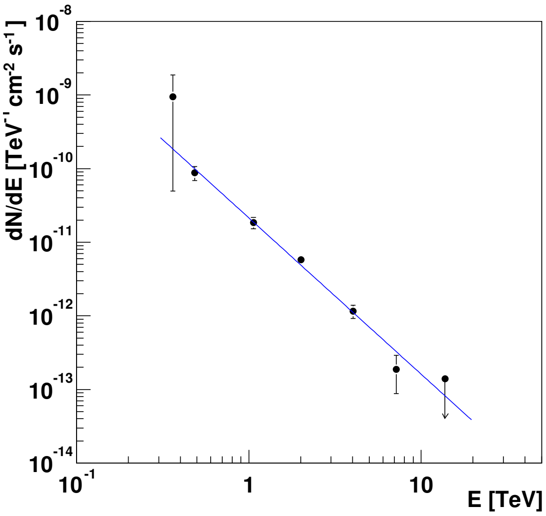

Figure 5.9: **Differential photon flux spectrum of RX J0852.0−4622.** The error bars denote $\pm 1\,\sigma$ statistical errors. The arrow denotes an upper limit (99.9% C.L.). The line is the result of a power law fit to the data with $\chi^2/\mathrm{ndf} = 4.3/4$. The upper limit was not included in the fit.

E [TeV]	φ [$10^{-12}\mathrm{TeV}^{-1}\mathrm{cm}^{-2}\mathrm{s}^{-1}$]
0.3622 ± 0.0007	$(9.5^{+9.3}_{-9.0})\,10^{-10}$
0.484 ± 0.003	$(8.8 \pm 0.2)\,10^{-11}$
1.063 ± 0.009	$(1.8 \pm 0.3)\,10^{-11}$
2.01 ± 0.02	$(5.8 \pm 0.8)\,10^{-12}$
4.02 ± 0.06	$(1.2 \pm 0.2)\,10^{-12}$
7.2 ± 0.2	$(2 \pm 1)\,10^{-13}$
13.8 ± 0.6	$< 1.4\,10^{-13}$ (99.9% C.L.)

Table 5.3: **Data points of the differential photon flux spectrum of the entire SNR RX J0852.0−4622.**

1 TeV was calculated from the fit parameters according to equation (4.3), and it is at the level of the flux of the Crab Nebula at these energies.

5.4 Morphology

The spatial distribution of the excess of γ-rays from the direction of RX J0852.0−4622 is shown in sky maps in Fig. 5.10. The area of the bins in the left panel is approximately that of a circle with a radius of 0.1° corresponding to the angular resolution of the instrument. This picture shows the excess in independent bins but with low resolution. The right panel of Fig. 5.10 shows the distribution of the excess with much finer detail. This sky map was obtained by integrating the excess in a circle with a radius of 0.1° around the centre of each bin. The integration area is denoted by the white circle. The radius of the circle was derived from the optimisation of the event selection cuts on point-like sources and is in the order of the angular resolution. The individual bins are correlated. The transformation of the celestial sphere to the sky maps is not area-preserving. Thus, the sky bins and integration circles do not have equal areas over the field of view. A discussion of this effect can be found in section 5.8.5.

A significance map of the sky region is shown in Fig. 5.11. Similar to the excess sky map in the right panel of Fig. 5.10, the significance was calculated from the on-source and off-source counts within a circle with 0.1° radius around each bin. The large circles in Fig. 5.11 are the integration regions for the analysis of the entire remnant (section 5.3, solid circle), the CANGAROO emission region (section 5.5, dashed circle) and the compact central source (section 5.6, dotted circle).

The γ-ray emission of RX J0852.0−4622 is a ring-like structure with a radius of $\approx 1°$. Significant emission can be seen from the northern, north-western, western and southern part of the shell. The north-western part of

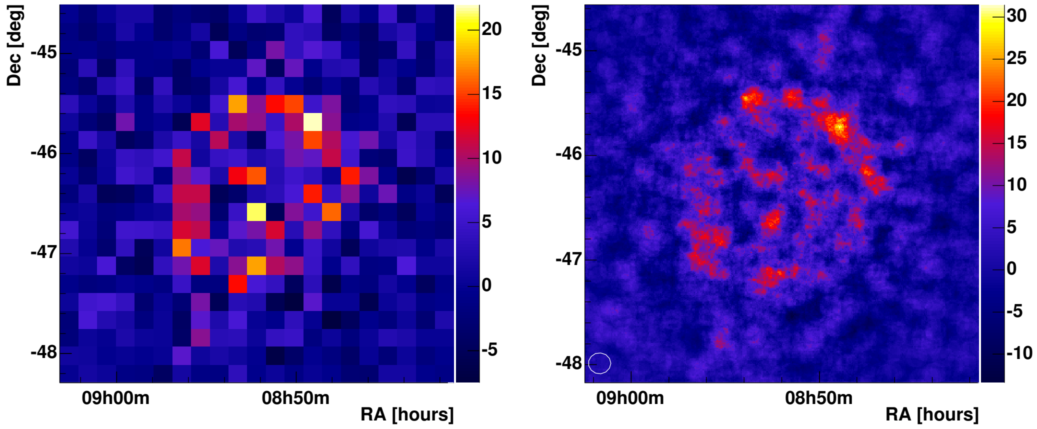

Figure 5.10: **Excess map of RX J0852.0−4622.** The colour bars denote excess counts. Left panel: The sky map is subdivided into bins of 0.18° × 0.18°. Right panel: For each bin the excess in a circle with a radius of 0.1° is integrated. Therefore, the bins are correlated. The integration region is denoted by the white circle.

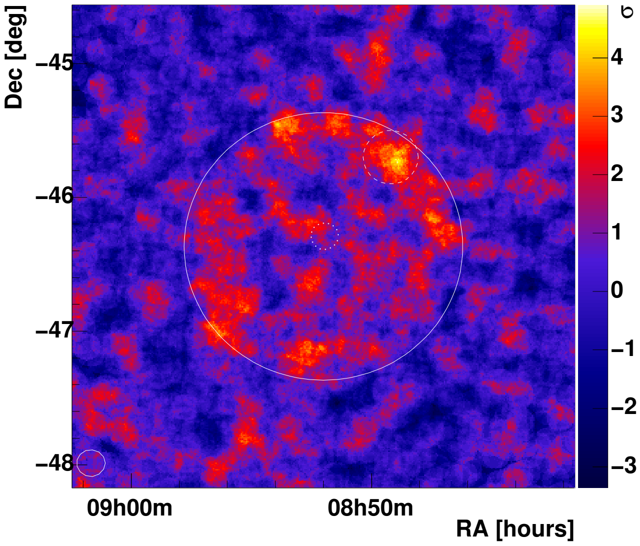

Figure 5.11: **Significance map of RX J0852.0−4622.** The significance (colour bar) is calculated from the on- and off-source events integrated in a circle of 0.1° radius as it was done for Fig. 5.10 (right panel). The integration area is denoted by the white circle in the lower left corner. The large circles denote he integration regions for the entire SNR (solid line), the CANGAROO emission region (dashed line) and AX J0851.9−4617.4 (dotted line).

the shell is the brightest emission region.

5.4.1 Correlation with X-ray Data

As the X-ray and γ-ray emission may be originating from the same population of parent particles, the correlation of the emission regions was analysed. Two X-ray measurements were chosen for a correlation analysis. The ROSAT data was taken in an All-Sky-Survey [VAB$^+$99] but with the advantage of a complete coverage of the SNR and acceptance corrected data with the disadvantage of low statistics. The ASCA satellite observed RX J0852.0−4622 with very high statistics but did not cover the entire remnant [SHE$^+$01]. Figure 5.12 shows correlated sky maps of the H.E.S.S. excess overlaid with contours of the ROSAT and ASCA measurements. All data were integrated in circles with a radius of 0.1° corresponding to the resolution of the γ-ray measurement. It can be seen that the γ-ray emission is correlated with the emission in X-rays. It should be noted that the ROSAT measurement is contaminated with emission from the Vela SNR (west of RX J0852.0−4622) and of RCW 37 (east of RX J0852.0−4622) which were not detected in this data set.

For a quantitative analysis the sky maps (in a field of view of 3° × 3°) of γ-rays and X-rays were subdivided into 100 bins of 0.3° × 0.3° size. The correlation coefficient, defined as

$$\varrho = \frac{\sum_{i=1}^{N}(\gamma_i - \overline{\gamma})(X_i - \overline{X})}{\sqrt{\sum_{i=1}^{N}(\gamma_i - \overline{\gamma})^2 \sum_{i=1}^{N}(X_i - \overline{X})^2}}, \tag{5.1}$$

was calculated from γ_i and X_i, the numbers of γ-ray counts and X-ray counts in bin i, respectively. $\overline{\gamma}$ and $\overline{X}$ are the mean values of the γ-ray and X-ray counts. Assuming Gaussian error propagation of $\sigma_{\gamma,i} = \sqrt{N_{\mathrm{on},i} + \alpha^2 N_{\mathrm{off,i}}}$ on the γ-ray counts and $\sigma_{X,i} = \sqrt{X_i}$ on the X-ray counts in bin i, the error on the correlation coefficient can be calculated using

$$\sigma(\varrho) = \sqrt{\sum_{i=1}^{N} \left[\left(\frac{\partial \varrho}{\partial \gamma_i} \sigma_{\gamma,i} \right)^2 + \left(\frac{\partial \varrho}{\partial X_i} \sigma_{X,i} \right)^2 \right]}$$

(see also [SL05]). For highly correlated or anti-correlated data, the confidence interval $\varrho \pm \sigma(\varrho)$ could leave the allowed region between −1 and 1. Asymmetric errors which ensure that the confidence interval is always within the allowed region ($-1 \leq \varrho \leq +1$) can be calculated using the Gaussian shape of the distribution $\zeta = \mathrm{atanh}(\varrho)$. The function atanh maps the interval $-1 \leq \varrho \leq +1$ into the interval $-\infty \leq \zeta \leq +\infty$. The symmetric errors

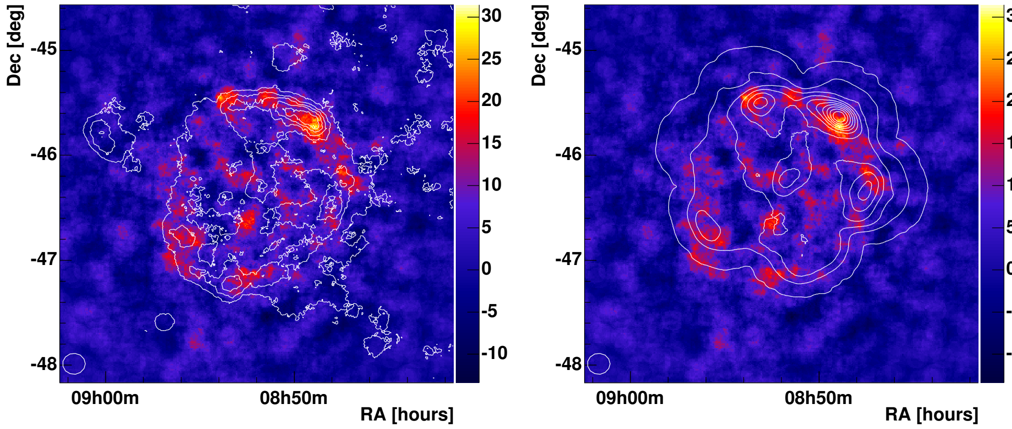

Figure 5.12: **Excess maps of γ-rays and X-rays.** The sky maps show the γ-ray excess counts in correlated bins (0.1°, white circle in the lower left corner of each plot). The colour bar denotes excess counts. The overlaid contour lines are X-ray counts in correlated sky bins. Left panel: The contour lines denote 20, 40, 60, 80, 100 and 120 X-ray counts from the ROSAT All-Sky Survey. Right panel: The contour lines denote 0 to 25000 counts in steps of 2500 counts of the ASCA measurement. The lowest contour line frames the ASCA observation region which does not cover the entire field of view.

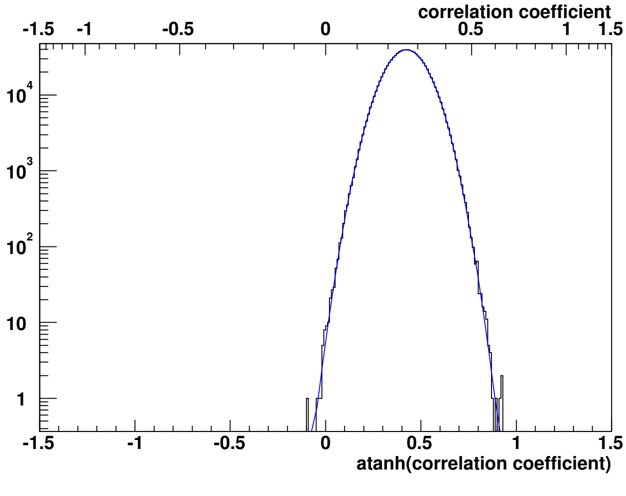

Figure 5.13: **Simulation of correlation coefficients.** In total 10^6 data sets, having 100 data points in each set, with a true correlation coefficient of 0.65 were simulated. The blue line represents the fit of a Gaussian function to the distribution atanh(ϱ).

on ζ are

$$\sigma(\zeta) = \pm\frac{\sigma(\varrho)}{1-\varrho^2}. \tag{5.2}$$

The symmetric confidence interval $\zeta \pm \sigma(\zeta)$ can be translated back using the tanh function. The asymmetric errors on ϱ are

$$\sigma_+(\varrho) = \tanh\left(\operatorname{atanh}(\varrho) + \frac{\sigma(\varrho)}{1-\varrho^2}\right) - \varrho$$

and

$$\sigma_-(\varrho) = \varrho - \tanh\left(\operatorname{atanh}(\varrho) - \frac{\sigma(\varrho)}{1-\varrho^2}\right).$$

The calculations of the correlation coefficient and its asymmetric errors were verified in a simulation. Data sets with 100 data points each (corresponding to the 100 bins in the analysis) were simulated. The data points (n_γ,n_X) have a true correlation coefficient of 0.65. Each data point was smeared out to simulate Gaussian errors of $\pm\sqrt{n_\gamma}$ and $\pm\sqrt{n_\mathrm{X}}$ on the γ-ray counts n_γ and X-ray counts n_X, respectively. Figure 5.13 shows the distribution of the calculated correlation coefficients in a simulation of 10^6 data sets. It can be seen that the correlation coefficients follow a Gaussian distribution in atanh(ϱ). The width of the distribution is the error $\sigma(\zeta)$ (eq. 5.2). It can be seen that most of the calculated correlation coefficients underestimate the true correlation coefficient, a result of the smearing due to statistical fluctuations. Therefore, it is likely that the true correlation of the γ-rays and X-rays will be higher than calculated.

Correlation with ROSAT Data

The ROSAT data are from the ROSAT All-Sky Survey taken with the PSPC detector in scanning mode [VAB+99]. It was extracted from the data base [ROS05] restricting the energies to above 1.3 keV in analogy to the initial detection of **(author?)** [Asc98]. The data are contaminated with low energy emission of the Vela SNR. The emission from RCW 37 is outside the field of view chosen for this correlation analysis.

In the upper panels of Fig. 5.14 the sky maps of γ-ray and X-ray counts are shown, covering a field of view of 3° × 3° and subdivided into 100 bins of 0.3° × 0.3° size. The lower panel of Fig. 5.14 shows the γ-ray and X-ray counts in each bin in a correlation plot. A correlation coefficient of $0.65^{+0.06}_{-0.07}$ was obtained indicating that the distributions of γ-ray and X-ray counts are highly correlated.

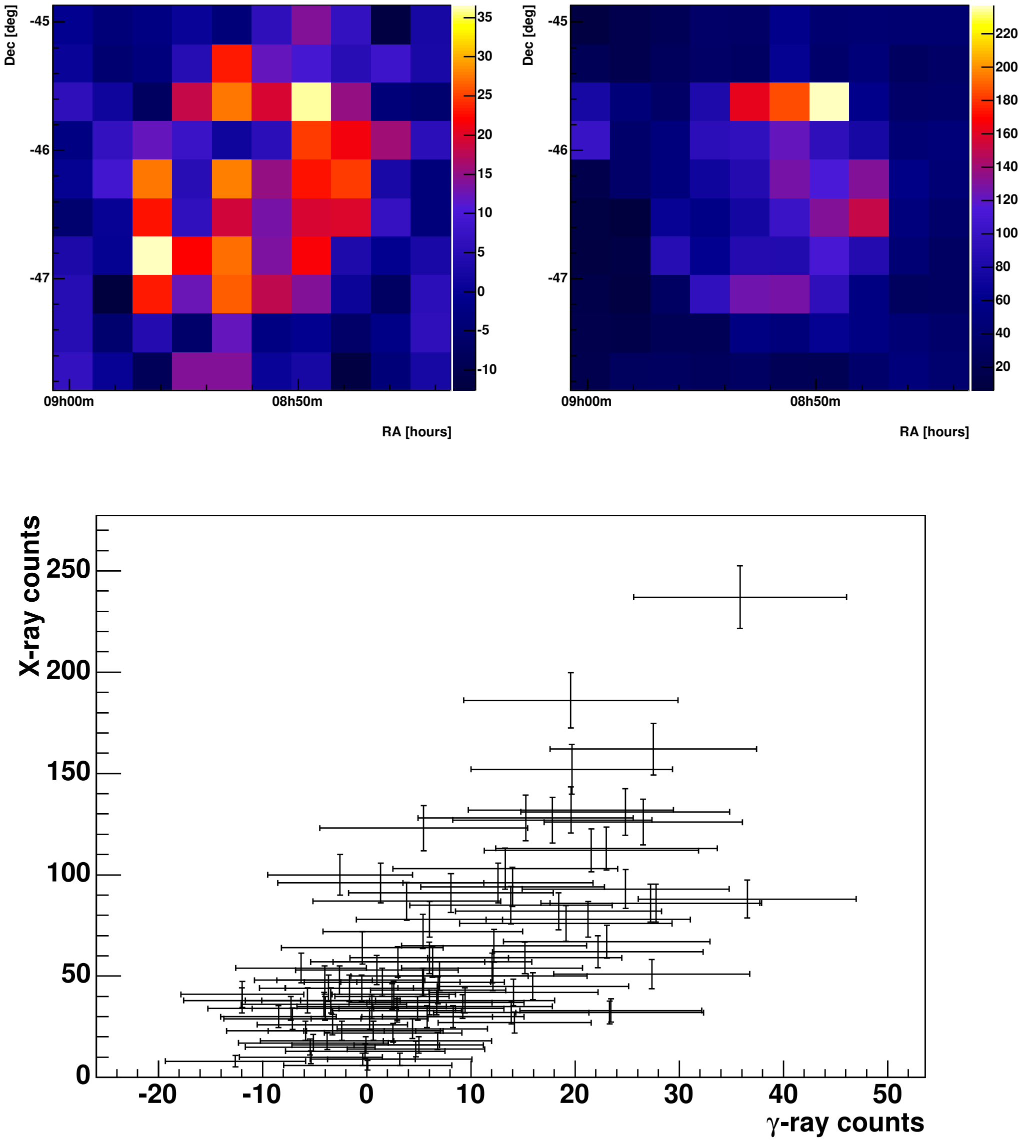

Figure 5.14: **Correlation with ROSAT data.** Shown are the sky maps of the H.E.S.S. data (upper left panel) and ROSAT data (upper right panel). The bins have a size of 0.3° × 0.3°. Lower Panel: Correlation plot of X-ray counts vs. γ-ray counts.

Correlation with ASCA Data

X-ray observations of RX J0852.0−4622 were carried out with the GIS detectors of the ASCA satellite. Data at seven distinct pointing positions with a duration of $\approx 17\,\mathrm{ks}$ at each position were taken which do not cover the complete SNR [SHE$^+$01]. The lowest contour line in the right panel of Fig. 5.12 denotes the observation region.

The correlation coefficient was calculated in the same way as for the ROSAT data. The upper panels of Fig. 5.15 show the sky maps of the γ-ray and ASCA X-ray measurement. Only those 58 bins having X-ray data were considered for the correlation analysis. The lower panel of Fig. 5.15 shows the correlation plot of γ-ray and X-ray counts. A correlation coefficient of $0.61^{+0.08}_{-0.10}$ was obtained. This value is in good agreement with the correlation coefficient obtained with the ROSAT data. The high correlation between γ-ray and X-ray counts can be confirmed using the ASCA data.

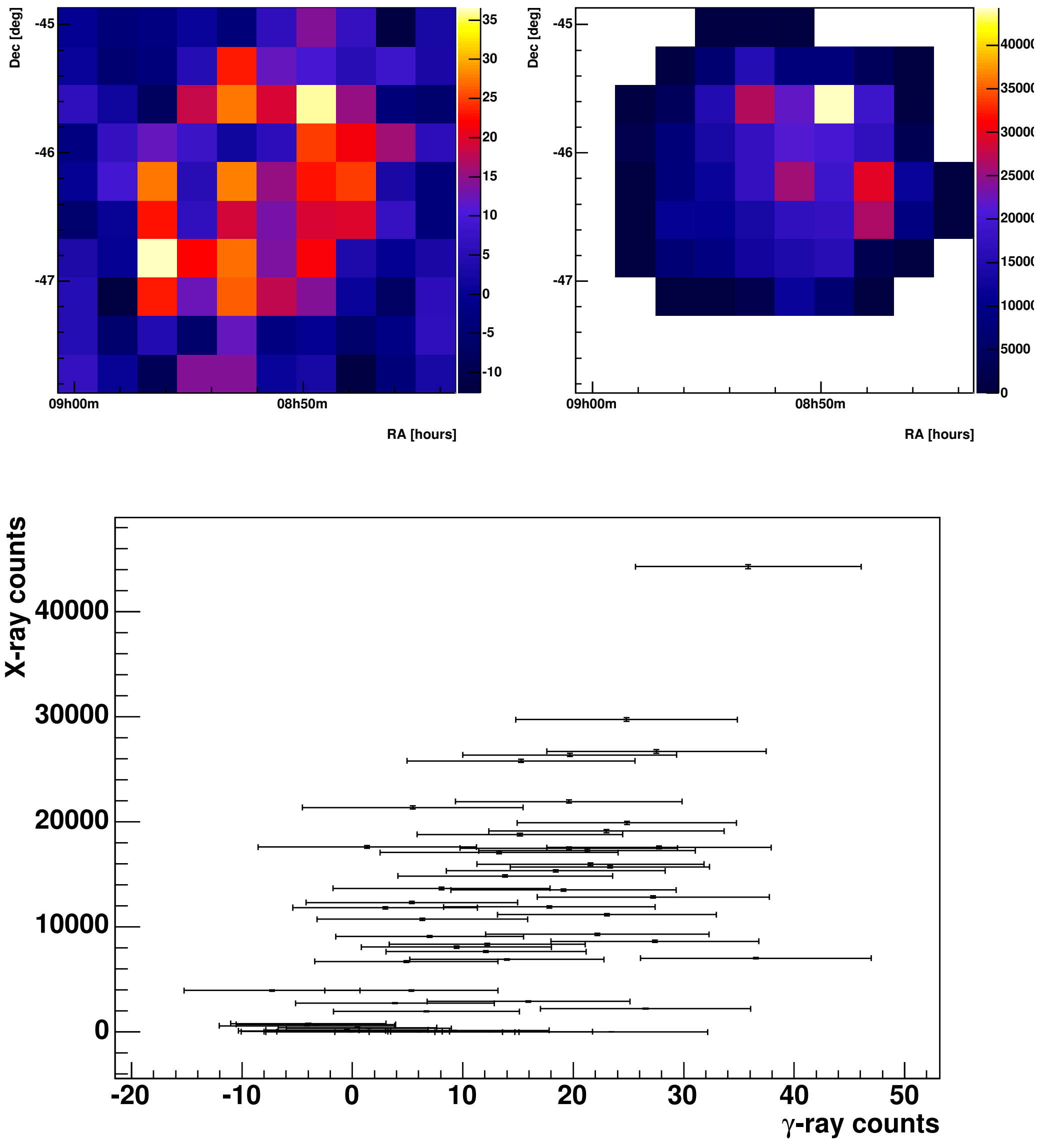

Figure 5.15: **Correlation with ASCA data.** Shown are the sky maps of the H.E.S.S. data (upper left panel) and ASCA data (upper right panel). The bins have a size of 0.3° × 0.3°. Lower Panel: Correlation plot of X-ray counts vs. γ-ray counts.

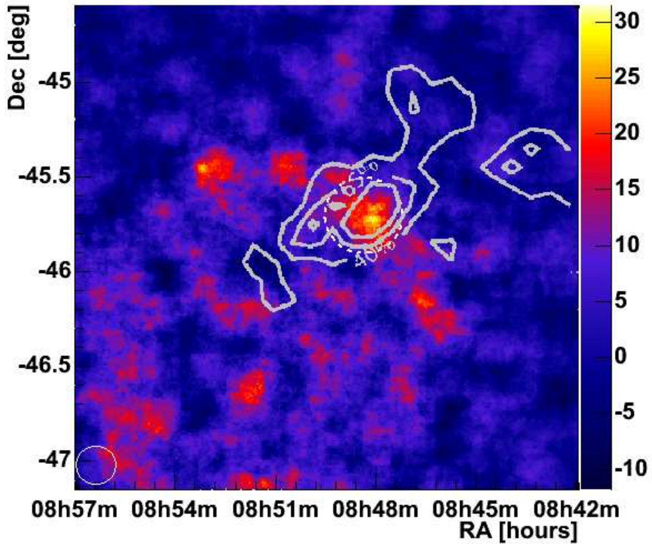

Figure 5.16: **CANGAROO emission region.** On top of the correlated H.E.S.S. excess map the significance region of the CANGAROO measurement is shown (grey contour line, [KEK$^+$05]) as well as the integration region for the H.E.S.S. data used in this work (dashed circle). The white circle in the lower left corner denotes the integration region of the sky bins.

5.5 The CANGAROO Emission Region

While H.E.S.S. observed γ-ray emission from the entire remnant, CANGAROO detected γ-rays from only a part of the remnant [KEK$^+$05] which is shown in Fig. 5.16. To compare the H.E.S.S. results with CANGAROO, a circular region around (RA 8h49m0s, Dec 45°39′) with a radius of 0.2° was chosen, which encloses the region of highest significance of the CANGAROO measurement. This region is denoted by the dashed circle in Fig. 5.16. An excess of 60 ± 10 γ-rays with a significance of $4.9\,\sigma$ was found. The number of on- and off-source counts are summarised in Table 5.4. The differential photon flux spectrum is shown in Fig. 5.17, the data points are summarised in Table 5.5. The data are well described by a power law. The spectral parameters obtained from a fit are summarised in Table 5.4. The spectral index is in good agreement with the measurement for the entire SNR. The integral flux above 1 TeV is at the level of 11% of the flux of the entire remnant.

5.6 The Compact Central Source

To search for emission from the compact central source candidate a circular region with a radius of 0.1°, corresponding to the cut optimised for the search for point sources, around AX J0851.9−4617.4 was chosen. An excess of 9 ± 6

number of on-source events	117
number of off-source events	87
off-source scaling factor α	0.671
number off excess events	60 ± 10
significance	$4.9\,\sigma$
live time (on) [s]	11368
γ-ray rate [min^{-1}]	0.32 ± 0.05
significance gain	$2.8\,\sigma/\sqrt{\mathrm{h}}$
energy threshold	0.35 TeV
$\varphi_{1\,\mathrm{TeV}}$ [$10^{-12}\,\mathrm{TeV}^{-1}\mathrm{cm}^{-2}\mathrm{s}^{-1}$]	2.6 ± 0.6
Γ	2.3 ± 0.3
$\Phi(E > 1\,\mathrm{TeV})$ [$10^{-12}\,\mathrm{cm}^{-2}\mathrm{s}^{-1}$]	2.0 ± 0.5
χ^2/ndf	0.56/4

Table 5.4: **Results for the CANGAROO emission region.**

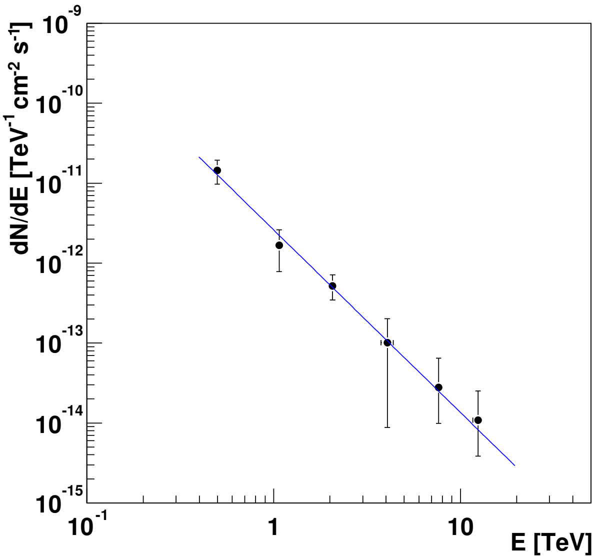

Figure 5.17: **Differential photon flux spectrum for the CANGAROO emission region.** The error bars are $\pm 1\,\sigma$ statistical errors. The blue line represents the result of a fit of a power law to the data with $\chi^2/\mathrm{ndf} = 0.56/4$.

E [TeV]	φ $[10^{-12}\mathrm{TeV}^{-1}\mathrm{cm}^{-2}\mathrm{s}^{-1}]$
0.50 ± 0.02	$(1.4 \pm 0.5)\,10^{-11}$
1.07 ± 0.04	$(1.7 \pm 0.9)\,10^{-12}$
2.1 ± 0.1	$(5.2 \pm 0.2)\,10^{-13}$
4.1 ± 0.3	$(1.0^{+1.0}_{-0.9})\,10^{-13}$
7.6 ± 0.3	$(2.8^{+3.7}_{-1.8})\,10^{-14}$
12.4 ± 0.8	$(1.1^{+1.4}_{-0.7})\,10^{-14}$

Table 5.5: **Data points of the differential photon flux spectrum of the CANGAROO emission region.**

number of on-source events	26
number of off-source events	26
off-source scaling factor α	0.671
number off excess events	9 ± 6
significance	$1.4\,\sigma$
live time (on) [s]	11368
γ-ray rate $[\mathrm{min}^{-1}]$	0.05 ± 0.03
significance gain	$0.8\,\sigma/\sqrt{\mathrm{h}}$

Table 5.6: **Results for AX J0851.9−4617.4.**

events was found, which is not statistically significant ($1.4\,\sigma$). The results are summarised in Table 5.6.

From the observed events upper limits on the integral flux are calculated according to [FC98]. The upper limits are shown in Table 5.7. In order to confirm the measured γ-ray rate with $5\,\sigma$ significance a total observation time of 39 h would be needed.

5.7 Cross Check using Alternative Background Data

For a cross check a second data set has been chosen to estimate the background. This data set belongs to observations of the Vela pulsar (PSR

energy threshold	integral flux $[\mathrm{cm}^{-2}\mathrm{s}^{-1}]$
$> 500\,\mathrm{GeV}$	$< 1.9 \times 10^{-12}$
$> 750\,\mathrm{GeV}$	$< 1.3 \times 10^{-12}$
$> 1\,\mathrm{TeV}$	$< 1.1 \times 10^{-12}$
$> 2\,\mathrm{TeV}$	$< 2.8 \times 10^{-13}$

Table 5.7: **Upper limits (99.9% C.L.) of the AX J0851.9−4617.4 emission.**

B0833−45) with an observation position at (RA 8h35m21s, Dec $-44°40'30''$). The Vela pulsar is located in a similar region of the sky like RX J0852.0−4622 and the data were taken in the same period. While these properties make the data set ideal for background estimation, the emission of γ-rays from the Vela pulsar wind nebula [KMH05] contaminates the estimated background. A sky map of the background after applying event selection cuts and transformed to the position of RX J0852.0−4622 is shown in Fig. 5.18, the contaminated region is marked with the dashed circle. The mean zenith angle of this data set of 27.3° is slightly larger than that of the on-source observations. A summary of the runs can be found in Table A.4. The total live time of these runs is 2.87 h.

The contamination of the background affects the region 1° – 2° south of the observation position. This background can be used only for on-source data where this region is outside the SNR, which are the runs with a wobble offset of −0.5° (3 runs with a live time of 1.2 h).

Figure 5.19 shows the radial distribution of the excess of γ-rays obtained by subtracting the background from the wobble −0.5° runs on RX J0852.0−4622. A negative excess in the contaminated region can be seen. An excess of 240 ± 30 events with a significance of $7.4\,\sigma$ has been found. Even though the significance is lower than calculated in section 5.3.1, which is due to the lower numbers of on- and off-source counts, the existence of γ-ray emission can be confirmed using this alternative background data set.

A sky map of the excess is shown in Fig. 5.20. The contaminated region is marked with a circle, a clear negative excess in this region can be seen. The γ-ray emission is predominantly from the western and north-western part of the remnant. Apart from the low statistics in this data set, the distribution of the excess roughly confirms the morphology shown in Fig. 5.10.

The differential photon flux spectrum is shown in Fig. 5.21. The results of a power law fit are summarised in Table 5.8. The parameters obtained here are, within statistical errors, in good agreement with the results using the standard background data set. From the difference of the results obtained here and the result presented in Table 5.2 systematic uncertainties can be estimated. The uncertainties are conservatively $0.2\,\mathrm{min}^{-1}$ (6%) on the γ-ray rate, $0.3 \times 10^{-11}\,\mathrm{TeV}^{-1}\mathrm{cm}^{-2}\mathrm{s}^{-1}$ (14%) on the flux normalisation, 0.2 on the spectral index and $0.1 \times 10^{-11}\,\mathrm{cm}^{-2}\mathrm{s}^{-1}$ (5%) on the integral flux. Further systematic uncertainties are discussed in the next section.

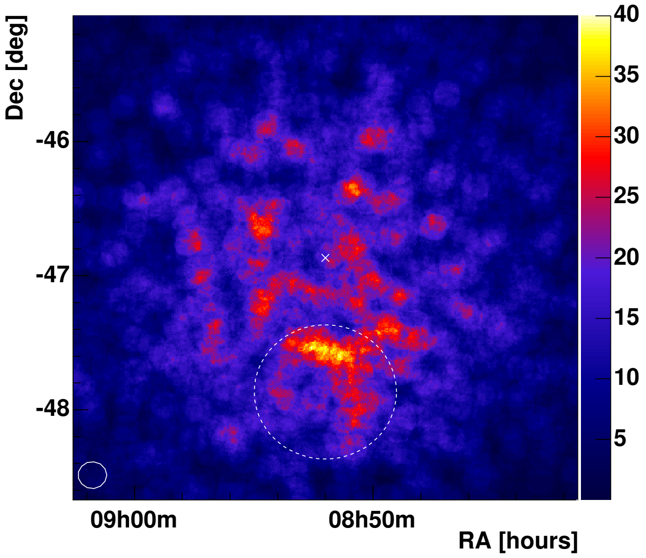

Figure 5.18: **Sky map of the alternative background.** The data are shown in correlated bins (0.1°, white circle in the lower left corner). The dashed circle denotes the region contaminated by possible emission of a γ-ray source. The observation position is marked with a cross. The colour bar denotes number of counts.

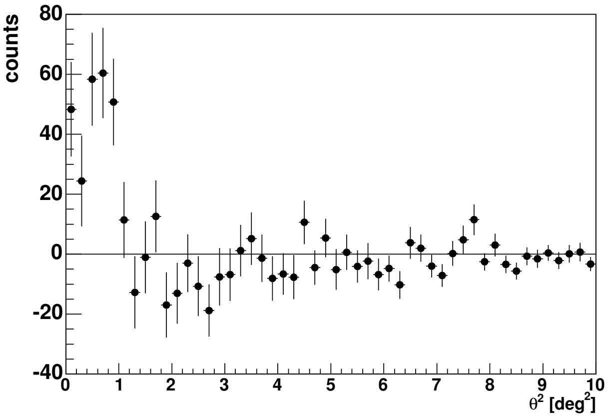

Figure 5.19: **RX J0852.0−4622 excess obtained with the alternative background.** The background in the region $1\,\mathrm{deg}^2 \leq \theta^2 \leq 4\,\mathrm{deg}^2$ is contaminated by possible γ-ray emission resulting in a negative excess.

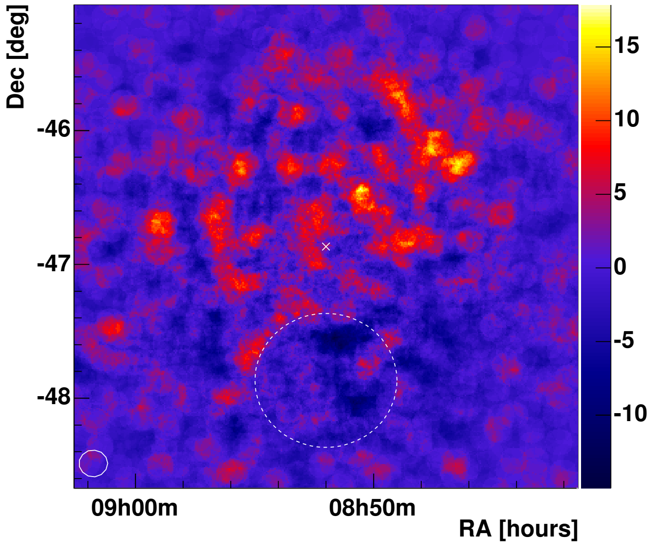

Figure 5.20: **Excess sky map obtained with the alternative background.** The excess is shown in correlated bins (0.1°, white circle in the lower left corner). The region contaminated by γ-ray emission of a possible source in the background data set is marked with the dashed circle. The cross denotes the observation position.

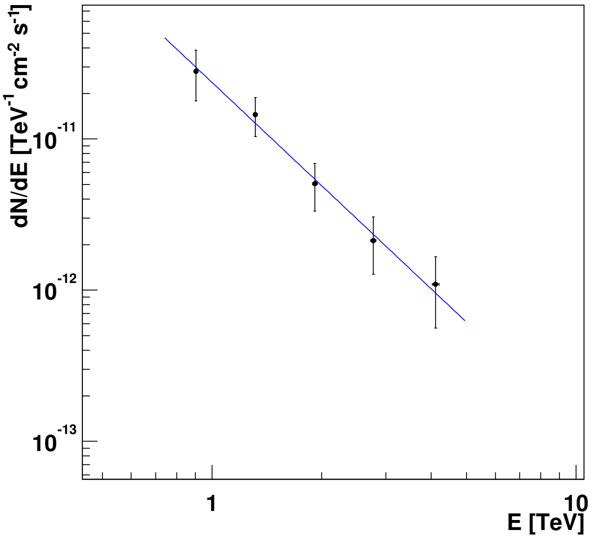

Figure 5.21: **Differential photon flux spectrum obtained with the alternative background.** The error bars denote $\pm 1\,\sigma$ statistical errors. The line is the result of a power law fit to the data with $\chi^2/\mathrm{ndf} = 0.4/4$.

number of on-source events	883
number of off-source events	1526
off-source scaling factor α	0.420
number off excess events	240 ± 30
significance	$7.4\,\sigma$
live time (on) [s]	4342
γ-ray rate [min^{-1}]	3.3 ± 0.4
significance gain	$6.7\,\sigma/\sqrt{\mathrm{h}}$
energy threshold	$0.35\,\mathrm{TeV}$
$\varphi_{1\,\mathrm{TeV}}$ [$10^{-11}\,\mathrm{TeV}^{-1}\mathrm{cm}^{-2}\mathrm{s}^{-1}$]	2.4 ± 0.6
Γ	2.3 ± 0.4
$\Phi(E > 1\,\mathrm{TeV})$ [$10^{-11}\,\mathrm{cm}^{-2}\mathrm{s}^{-1}$]	1.8 ± 0.5
χ^2/ndf	0.4/3

Table 5.8: **Results of the RX J0852.0−4622 observations obtained with the alternative background.**

5.8 Systematic Studies

The measured flux depends on the chosen on-source region and the background estimation. The spectral parameters are calculated from a fit to a binned spectrum, the chosen binning turned out to have an impact on the spectral parameters. In order to validate the atmospheric conditions used in the simulations a cross-check with an alternative atmospheric model was performed. The sky maps shown in this work are not area conserving, the resulting uncertainty is discussed. At the end of this section the systematic uncertainties on the flux and the spectral parameters are summarised.

5.8.1 Selection of Emission Region

The region which was analysed as emission region of the entire SNR was chosen a priori to be a circle with a radius of 1°, based on X-ray observations. This may not be the exact γ-ray emission region. The analysis was remade for circular regions of 0.95° ($\theta^2 = 0.9\,\mathrm{deg}^2$) and 1.05° ($\theta^2 = 1.1\,\mathrm{deg}^2$). The results for these cuts are summarised in Table 5.9. The larger cut yields similar results to those obtained with the a priori cut (Table 5.2), although with less significance. No further excess can be gained using a larger area. The rate using the lower cut is significantly lower, obviously cutting into the emission region. The a priori chosen cut describes the emission region appropriately.

	$\theta^2 \leq 0.9\,\mathrm{deg}^2$	$\theta^2 \leq 1.1\,\mathrm{deg}^2$
number of on-source events	1890	2601
number of off-source events	2033	2863
off-source scaling factor α	0.671	0.671
number off excess events	530 ± 50	680 ± 60
significance	$10.2\,\sigma$	$11.1\,\sigma$
live time (on) [s]	11368	11368
γ-ray rate [min^{-1}]	2.8 ± 0.3	3.6 ± 0.3
significance gain	$5.7\,\sigma/\sqrt{\mathrm{h}}$	$6.2\,\sigma/\sqrt{\mathrm{h}}$

Table 5.9: **Variation of the angular cut.**

5.8.2 Variation of the Background

The zenith angle (ZA) distribution of the background data does not match the zenith angle distribution of the on-source data set. It can be seen in Fig. 5.1 that the background data comprise two sets with zenith angles around 19° and around 32°. To estimate the influence of the zenith angle, the background data set has been divided into these two sets, in the following on called low ZA set and high ZA set, respectively. After normalisation according to the live time 1770 off-source events in the low ZA set and 1450 off-source events in the high ZA set were found. Figure 5.22 shows these data points as a function of the zenith angle. From the linear interpolation

$$f(\mathrm{ZA}) = -(24 \pm 4) \times (\mathrm{ZA}/1^\circ) + (2200 \pm 120)$$

the number of off-source events at a zenith angle of 24.5° (the mean zenith angle of the on-source data) can be estimated to be 1650 ± 30 events. In the estimation of the error, the correlation between the two parameters of the linear function has been taken into account. From this number of off-source events the excess can be calculated to be 650 ± 30 at a rate of $3.4 \pm 0.2\,\mathrm{min}^{-1}$ which is in good agreement with the results summarised in Table 5.2. The difference between the γ-ray rates obtained here and presented in Table 5.2 is $0.1\,\mathrm{min}^{-1}$ (3%).

5.8.3 Variation of the Binning in the Spectral Fit

The spectral parameters were obtained by a fit to binned data. To estimate the systematic uncertainty arising from different binning, the analysis has been remade with varying bin numbers. More bins provide more data points for the fit but with higher errors due to lower statistics in each

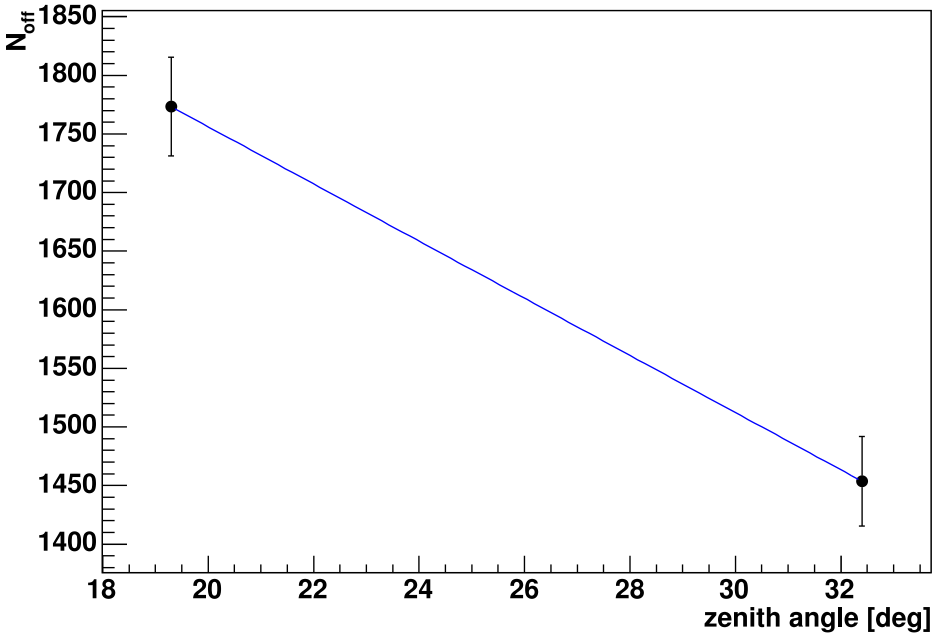

Figure 5.22: **Zenith angle variations.** The plot shows the normalised off-source counts as a function of the zenith angle. The blue line represents a linear interpolation.

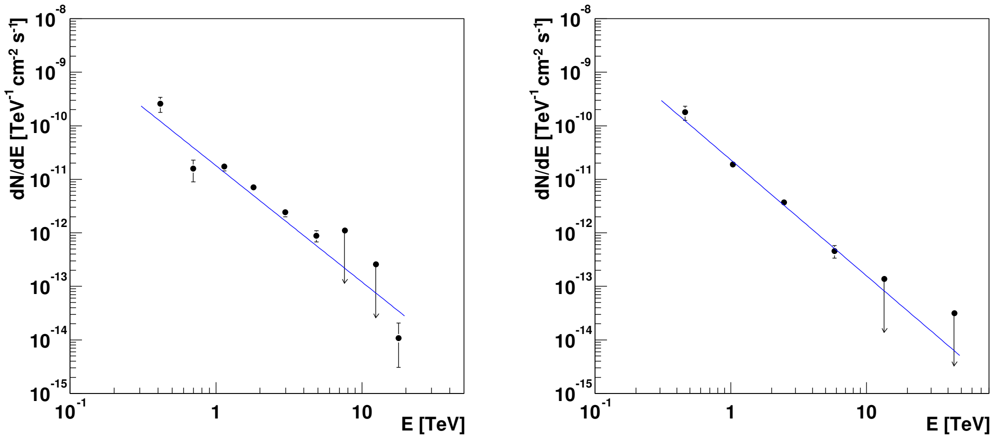

Figure 5.23: **Systematic studies of the spectral parameters.** The figures show the spectrum shown in Fig. 5.9 with different numbers of bins (left panel 9 bins, right panel 6 bins). The error bars denote $\pm 1\,\sigma$ statistical errors, the arrows represent 99.9% C.L. upper limits. The lines are the results of power law fits to the data with $\chi^2/\mathrm{ndf} = 30.2/5$ (left panel) and 2.9/2 (right panel). The upper limits were not included in the fits.

bin. On the other hand, less bins reduce the errors in each bin but providing less data points for the fit. The bin size is always larger than the energy resolution of $\approx 20\%$. Two cases of different binnings are shown in Fig. 5.23. It can be seen that in case of less bins (right panel) the data is better described by the fit. For 5 different binnings (including that shown in Fig. 5.9) the flux normalisation varied between $1.2 \times 10^{-11}\,\mathrm{TeV}^{-1}\mathrm{cm}^{-2}\mathrm{s}^{-1}$ and $2.4 \times 10^{-11}\,\mathrm{TeV}^{-1}\mathrm{cm}^{-2}\mathrm{s}^{-1}$ with an RMS of $0.4 \times 10^{-11}\,\mathrm{TeV}^{-1}\mathrm{cm}^{-2}\mathrm{s}^{-1}$ or 25% with respect to the mean. The spectral index varied between 2.0 and 2.3 with an RMS of 0.1. The integral flux above 1 TeV varied between $1.1\times10^{-11}\,\mathrm{cm}^{-2}\mathrm{s}^{-1}$ and $1.9\times10^{-11}\,\mathrm{cm}^{-2}\mathrm{s}^{-1}$ with a RMS of $0.3\times10^{-11}\,\mathrm{cm}^{-2}\mathrm{s}^{-1}$ or 20% with respect to the mean value. These systematic uncertainties will be included in the estimation of the final systematic uncertainties in section 5.8.6.

5.8.4 Alternative Simulations

The analysis presented in this work was carried out using simulations of Cherenkov light propagating through an atmosphere typical for deserts. This atmospheric model is used in the standard analysis of all H.E.S.S. data. The observations of RX J0852.0−4622 were carried out during the raining

number of on-source events	2235
number of off-source events	2379
off-source scaling factor α	0.671
number off excess events	640 ± 60
significance	$11.4\,\sigma$
live time (on) [s]	11368
γ-ray rate [min^{-1}]	3.4 ± 0.3
significance gain	$6.4\,\sigma/\sqrt{\mathrm{h}}$
energy threshold	0.36 TeV
$\varphi_{1\,\mathrm{TeV}}$ [$10^{-11}\,\mathrm{TeV}^{-1}\mathrm{cm}^{-2}\mathrm{s}^{-1}$]	2.2 ± 0.2
Γ	2.2 ± 0.1
$\Phi(E > 1\,\mathrm{TeV})$ [$10^{-11}\,\mathrm{cm}^{-2}\mathrm{s}^{-1}$]	1.8 ± 0.2
χ^2/ndf	6.4/4

Table 5.10: **Results for RX J0852.0−4622 obtained with alternative simulations.**

season in Namibia and a desert atmosphere might not be appropriate. In an atmosphere with higher humidity a larger absorption of the Cherenkov light is expected. In order to investigate the effect of the atmospheric conditions an alternative analysis has been carried out using γ-ray simulations for a maritime atmosphere. The simulations affect the lookup tables for the scaled parameters used in the event selection and the reconstructed energy. The applied cuts are those of the hard configuration which are summarised in Table 4.1.

Figure 5.24 shows the radial distribution of the excess obtained with alternative simulations. An excess of 640 ± 60 γ-rays with a significance of $11.4\,\sigma$ was obtained. The spatial distribution of the excess is shown in a correlated sky map in Fig. 5.25 reproducing the morphology obtained with the standard simulations. The differential photon flux spectrum shown in Fig. 5.26 is fit with a power law. The obtained results are summarised in Table 5.10 and agree within statistical errors with the results obtained with the standard simulations. The uncertainties with respect to the standard analysis (Table 5.2) are $0.1\,\mathrm{min}^{-1}$ (3%) on the γ-ray rate, $0.1 \times 10^{-11}\,\mathrm{TeV}^{-1}\mathrm{cm}^{-2}\mathrm{s}^{-1}$ (5%) on the flux normalisation, 0.1 on the spectral index and $0.1 \times 10^{-11}\,\mathrm{cm}^{-2}\mathrm{s}^{-1}$ (5%) on the integral flux.

5.8.5 Systematic Error in the Sky Maps

All sky maps presented here are in a Cartesian transformation of right ascension and declination. The bins in these sky maps have the same size Δ_{Dec} and Δ_{RA} along declination and right ascension. This transformation is not

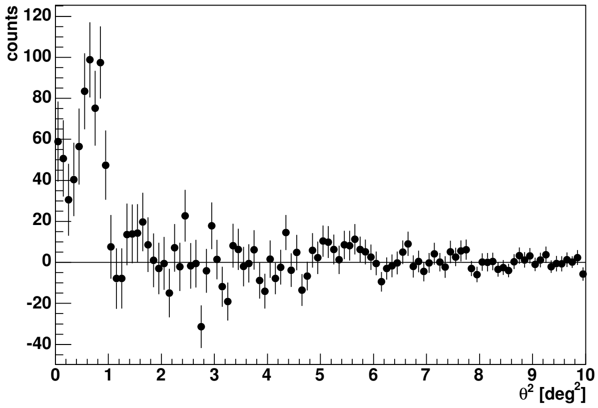

Figure 5.24: **Radial distribution of the excess obtained with alternative simulations.** The plot shows the radial distribution of the excess of γ-rays as function of the angular distance from the direction of the centre of the SNR.

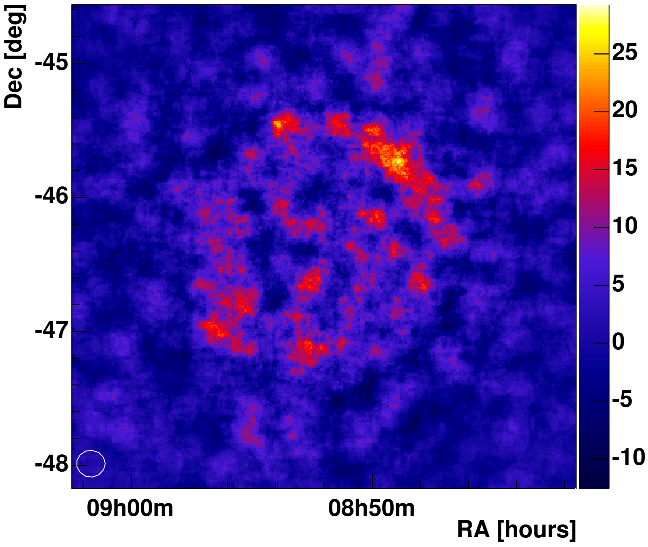

Figure 5.25: **Excess sky map obtained with alternative simulations.** The data are shown in correlated bins (0.1°, white circle). The colour bar denotes the number of excess counts.

γ-ray rate	6%
$\varphi_{1\,\mathrm{TeV}}$	24%
$\Phi(E > 1\,\mathrm{TeV})$	21%
Γ	0.2

Table 5.11: **Systematic uncertainties.**

area-preserving. The area of each bin is

$$A_{\mathrm{bin}} = \Delta_{\mathrm{Dec}} \times \Delta_{\mathrm{RA}} \cdot \cos(\mathrm{Dec}_{\mathrm{bin}}).$$

The size of the bins has been chosen such that the area of the bins at the declination of the centre of the sky map is correct. The ratio of the area of a sky bin to a sky bin at the centre of the sky map is

$$\frac{A_{\mathrm{bin}}}{A_{\mathrm{centre}}} = \frac{\cos \mathrm{Dec}_{\mathrm{bin}}}{\cos \mathrm{Dec}_{\mathrm{centre}}}. \tag{5.3}$$

A graph showing this dependence is pictured in Fig. 5.27. From this effect arises a systematic error in the generation of the correlated sky map. The integration of the events in a circle with a radius of 0.1° is done on a binned sky map. The area of the circle is only correct for bins at the same declination as the centre of the sky map. For bins with higher or lower declination equation (5.3) must be applied. The systematic error of the integration area within the sky maps shown here is ±3%. The integration of the test regions for the entire remnant (section 5.3), the CANGAROO emission region (section 5.5) and the compact central source (section 5.6) were not done on a binned sky map, therefore the error discussed here does not apply for this regions.

5.8.6 Systematic Errors

The final systematic uncertainties were obtained as the quadratic sum of the individual uncertainties discussed in the last sections. The error on the γ-ray rate was estimated from the variations of the zenith angle of the background, from the use of an alternative background and the use of a different atmospheric model in the simulations. The errors on the spectral parameters were estimated from use of an alternative background and a different atmospheric model in the simulations. Additional errors on the spectral parameters arise from variations of the bin size in the differential energy spectrum. The final systematic uncertainties are summarised in Table 5.11.

The systematic error on the integral flux can be calculated from the systematic studies discussed in the previous sections and by propagating the

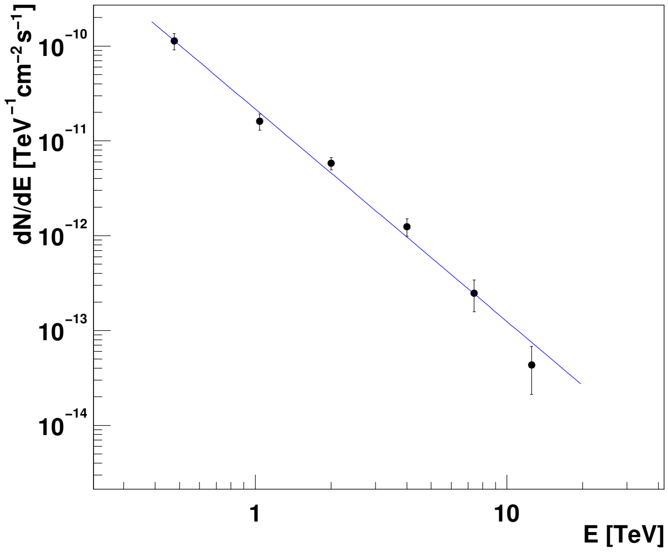

Figure 5.26: **Differential photon flux spectrum of RX J0852.0−4622 obtained with alternative simulations.** The error bars denote ±1 σ statistical errors. The line is the result of a power law fit to the data with χ^2/ndf = 6.4/4.

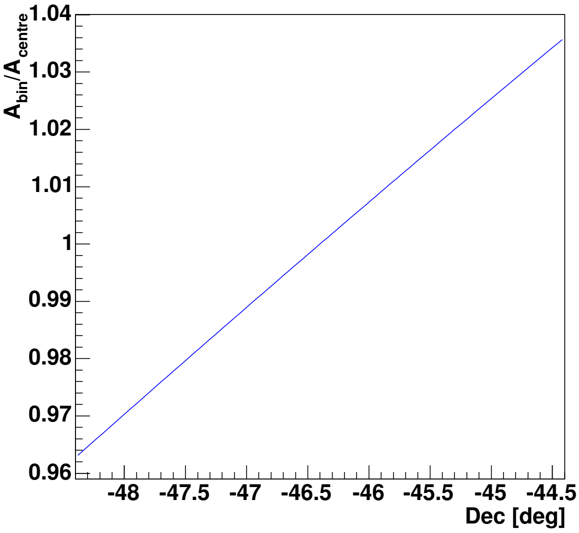

Figure 5.27: **Systematic error on the areas in the sky maps.** The graph shows the ratio of the area of a sky bin to the area of a sky bin at the centre of the sky maps (Dec $= 44°22'$) as a function of the declination.

errors of the spectral fit parameters. Both calculations give the same systematic error of 21%.

Due to the not area conserving transformation the sky maps contain a systematic error of ±3% depending on the declination. This error does not affect the systematic uncertainties of the flux and the spectral parameters shown in Table 5.11.

5.9 Discussion

RX J0852.0−4622 was observed with H.E.S.S. in February 2004 for 4.5 h. In this data set, a strong signal of γ-rays at a rate of $3.5 \pm 0.3_{\text{stat}} \pm 0.2_{\text{syst}}\,\text{min}^{-1}$ with a significance of $11.9\,\sigma$ was found. RX J0852.0−4622 is confirmed to be a γ-ray emitter.

A spectral analysis of the γ-ray excess shows that the differential photon flux spectrum follows a power law

$$\frac{\mathrm{d}\Phi}{\mathrm{d}E} = (2.1 \pm 0.2_{\text{stat}} \pm 0.5_{\text{syst}}) \times 10^{-11}\,\text{TeV}^{-1}\text{cm}^{-2}\text{s}^{-1} \cdot \left(\frac{E}{1\,\text{TeV}}\right)^{-(2.1 \pm 0.1_{\text{stat}} \pm 0.2_{\text{syst}})}.$$

The integral photon flux above 1 TeV is calculated to be

$$\Phi(E > 1\,\text{TeV}) = (1.9 \pm 0.2_{\text{stat}} \pm 0.4_{\text{syst}}) \times 10^{-11}\text{cm}^{-2}\text{s}^{-1}.$$

This is at the level of the Crab flux which makes RX J0852.0−4622 one of the brightest γ-ray sources in the sky.

The γ-ray emission region of RX J0852.0−4622 is found to be clearly extended. Therefore, RX J0852.0−4622 is the second extended SNR which can be resolved at VHE γ-rays following the detection of RX J1713.7−3946 [AAA⁺04b]. The γ-ray emission region of RX J0852.0−4622 is roughly a ring-like structure with a diameter of $\approx 2°$. Significant emission comes from the northern, north-western, western and south-eastern part of the rim, whereof the north-western part is the brightest. The morphology of the γ-ray and X-ray emissions are clearly correlated. Correlation coefficients of $0.65^{+0.06}_{-0.07}$ with ROSAT data and $0.61^{+0.08}_{-0.10}$ with ASCA data have been found. This suggests that the X-ray and γ-ray emission originate from the same emission regions.

The resolution of the morphology allows to investigate parts of the remnant. The brightest emission region is the north-western part, coincident with the maximum of the X-ray emission and target of the high resolution observations by XMM-Newton and *Chandra* [IAB⁺05, BYH05]. It is also the region from where CANGAROO detected γ-ray emission [KEK⁺05]. The

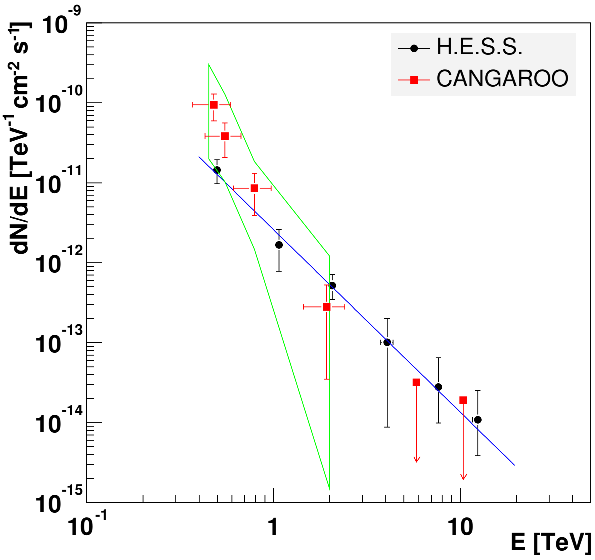

Figure 5.28: **Differential photon flux spectrum of the CANGAROO emission region.** The black data points are the H.E.S.S. measurement. The error bars are $\pm 1\,\sigma$ statistical errors. The blue line represents the result of a fit of a power law to the data. The red points are the CANGAROO measurement [KEK$^+$05]. The arrows denote $2\,\sigma$ upper limits. The green region is the uncertainty of the CANGAROO fit.

detection of the γ-rays from the CANGAROO region can be confirmed with $4.9\,\sigma$. The integral flux above 1 TeV is at the level of 11% of the Crab flux confirming the CANGAROO result of 12% of the Crab Nebula published by **(author?)** [KEK$^+$05]. A power law fit to the CANGAROO data points yields an integral flux above 1 TeV of $(1.2 \pm 1.1) \times 10^{-12}\,\mathrm{cm}^{-2}\mathrm{s}^{-1}$. Within statistical errors this result agrees well with the integral flux measured with H.E.S.S. Figure 5.28 shows the data points of the differential photon flux spectra of CANGAROO and H.E.S.S. **(author?)** [KEK$^+$05] derive a power-law index of $4.3^{+4.4}_{-1.7}$ from their data which is apparently a steeper spectrum than the H.E.S.S. result presented here (spectral index 2.3 ± 0.3). However, given the large uncertainty of the CANGAROO measurement the difference between the two values is on a level of $1.2\,\sigma$ where only statistical errors are taken into account. **(author?)** [KEK$^+$05] give a confidence region of the CANGAROO measurement by the range were the χ^2 of the fit is less than $\chi^2_{\mathrm{min}} + 1$. This confidence region, indicated by the green region in Fig. 5.28, is consistent with the H.E.S.S. data.

A search for a possible emission of γ-rays from the compact central X-ray source AX J0851.9−4617.4 has been performed. No significant emission has been found. The upper limit on the integral photon flux above 1 TeV is calculated to be $\Phi(E > 1\,\mathrm{TeV}) < 1.1 \times 10^{-12}\mathrm{cm}^{-2}\mathrm{s}^{-1}$ at a 99.9% confidence level. This is at a level of 6% of the Crab flux above this energy. To confirm the observed flux with a significance of $5\,\sigma$ a total observation time of 39 h would be needed.

Given the high flux and large extension of RX J0852.0−4622 it is a prime candidate for further deep observations. A detailed discussion of the measurements presented here with respect to the source particles responsible for the γ-ray radiation will be given in the next chapter.

Chapter 6

Interpretation

It was shown in the last chapter that γ-rays from the RX J0852.0−4622 supernova remnant were detected with high significance. Therefore, following the detection by CANGAROO [KEK$^+$05], RX J0852.0−4622 can be established as a γ-ray emitter. In this chapter the observational results will be discussed with respect to the parent particles producing the γ-rays.

6.1 Morphology

In Fig. 5.10 of the last chapter the spatial distribution of the γ-rays is shown. Even though the low statistics do not allow to discuss details of the morphology, the γ-ray emission seems to form a ring-like structure with almost no emission from the projected inner parts of the remnant. If the emission would come uniformly from the entire remnant including the interior one would expect to see a disc with the centre being the brightest part. Thus, it can be ruled out that the emission originates from the interior of the remnant. If the emission comes only from a thin shell one would expect the lowest emission from the projected centre where the line of sight passes only a small fraction of the emitting shell. Most of the emission is expected at the projected rim where the line of sight passes much more of the emitting material. Thus, the ring-like structure suggests that the γ-rays originate from the shell of the supernova remnant, indicating that they are produced by particles which were accelerated in the shock front of the expanding supernova remnant.

A high correlation of the γ-ray emission with X-ray emission has been shown (see Fig. 5.12 and section 5.4.1) on an angular scale of about 0.3°. Due to the poorer angular resolution of H.E.S.S. (0.1°) compared to X-ray experiments ($\approx 0.5''$) it cannot be proved if the γ-ray emission has the same filamentary structure as in X-rays (shown in Fig. 2.3 and 2.4). However, the good correlation between γ-ray and X-ray morphology suggests that both emissions are produced in the same region — the shell of the supernova remnant.

6.2 The Energy Spectrum

The observed γ-rays from the entire supernova remnant follow a power law in energy, with a spectral index of 2.1.

The low statistics of the measurement do not allow to draw conclusions on possible deviations from a power law. A steepening of the spectrum to higher energies is expected for a source population with a certain maximum energy. Further observations are needed to test for a cut-off in the observed γ-ray spectrum.

6.3 Acceleration Mechanisms

The observed γ-rays are produced by source particles of non-thermal energy distribution. Diffusive Shock Acceleration (see section 3.5) is a powerful mechanism of accelerating particles in the shock fronts of supernova remnants. Two scenarios have to be distinguished, the acceleration of electrons or protons. In the following sections it will be discussed if these mechanisms could explain the observed γ-ray radiation.

6.3.1 Electronic Scenario

X-ray Emission and Synchrotron Radiation

X-ray emission from the shell of RX J0852.0$-$4622 with energies between 0.5 and 10 keV was observed with the ASCA satellite [SHE$^+$01]. This emission can be explained as synchrotron emission of electrons. Using equation (3.26) one can estimate the energy of the electrons which are emitting the synchrotron radiation. This is shown in Fig. 6.1 for various magnetic field strengths. Based on the width of the X-ray filaments in the north-western part of RX J0852.0$-$4622 (see Fig. 2.4) a magnetic field in this region of $\approx 500\,\mu$G is discussed [BYH05]. From the widths of the shells of other supernova remnants **(author?)** [VBK05] calculated magnetic fields between 100 and 500 μG. It can be seen in Fig. 6.1 that magnetic fields in the order of several hundred μG require electron energies of several tens of TeV in order to describe the observed X-ray emission as synchrotron radiation. Electron energies of more than 100 TeV are required for magnetic fields around $3\,\mu$G,

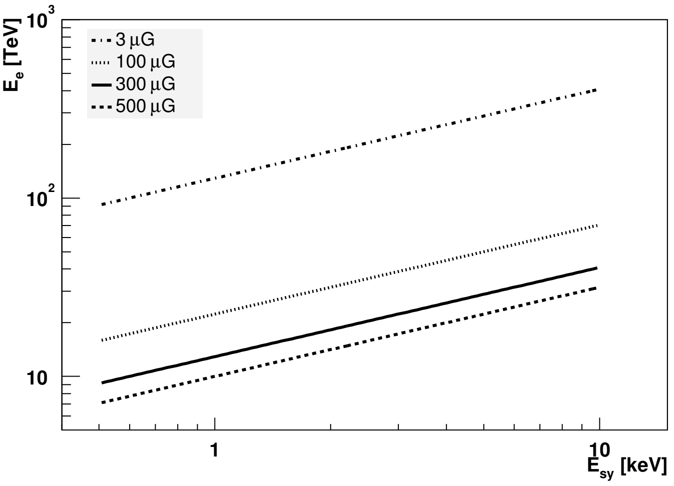

Figure 6.1: **Electron energy.** The plot shows the electron energy E_e which is required to emit synchrotron radiation of energy $E_{\rm sy}$ for several magnetic fields.

comparable to the interstellar magnetic field. The observation of synchrotron emission is evidence for the acceleration of electrons up to energies of more than 10 TeV.

Inverse Compton Radiation

These high energy electrons undergo inverse Compton scattering, mainly on the cosmic microwave background. From equation (3.38) one can estimate the energy range in which the inverse Compton radiation of these electrons can be expected. For magnetic fields of several hundred μG inverse Compton radiation is expected at energies around 1 to 10 TeV, the energy range where γ-rays were observed with H.E.S.S. It will be now discussed if the observed γ-ray emission could be explained as being inverse Compton radiation of these high energy electrons.

Assuming that both inverse Compton radiation and synchrotron radiation are emitted isotropically one can use equation (3.37) to estimate the inverse Compton flux at Earth. The observed energy flux in X-rays from the entire remnant was measured with ASCA to be $w_{\rm X} = 9.9 \times 10^{-11}\,\mathrm{erg\,cm^{-2}\,s^{-1}}$ [SHE+01][1]. This value is shown in Fig. 6.2. The width of the line indicates the energy range of the measurement. Using equation (3.37) one can estimate the expected energy flux from inverse Compton scattering on the cosmic microwave background. These estimations are shown in Fig. 6.2 for various magnetic fields. Assuming a magnetic field of 300 μG one can directly com-

---

[1] Note, that in the original paper no uncertainty of this measurement is given and that the measurement does not cover the entire region covered by the H.E.S.S. measurement.

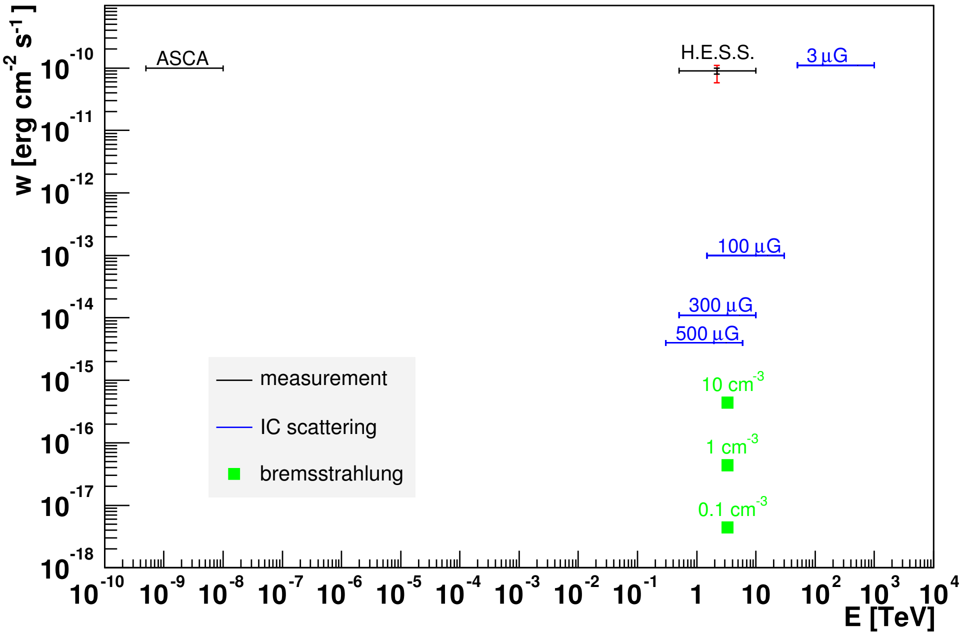

Figure 6.2: **Emission of electrons.** The plot shows the energy flux as a function of the photon energy as measured by H.E.S.S. and ASCA. The blue lines denote the energy flux expected from inverse Compton scattering for several magnetic fields. The green points denote the expected energy flux due to bremsstrahlung produced by 10 TeV electrons. The statistical and systematic uncertainties of the H.E.S.S. energy flux are denoted by the black and red error bars, respectively. The horizontal widths of the data points denote the covered energy range.

pare the synchrotron emission between 0.5 and 10 keV and the γ-ray emission between 0.5 and 10 TeV (see eq. 3.38). It can be seen that for $B = 300\,\mu\text{G}$ an energy flux of $w_\gamma(0.5 - 10\,\text{TeV}) \approx 10^{-14}\,\text{erg}\,\text{cm}^{-2}\,\text{s}^{-1}$ is expected. The observed energy flux in γ-rays can be calculated from the power law spectrum of the photon flux and the spectral parameters shown in Table 5.2 to be

$$\begin{aligned} w_\gamma &= \int\limits_{0.5\,\text{TeV}}^{10\,\text{TeV}} E\varphi_{1\,\text{TeV}} \cdot \left(\frac{E}{1\,\text{TeV}}\right)^{-\Gamma} \mathrm{d}E \\ &= (9 \pm 1_{\text{stat}} \pm 2_{\text{syst}}) \times 10^{-11}\,\text{erg}\,\text{cm}^{-2}\,\text{s}^{-1}, \end{aligned}$$

which is shown in Fig. 6.2. The horizontal width of the data point denotes the range of the energy spectrum, 0.5 to 10 TeV. It can be seen that this flux is much higher than expected from inverse Compton scattering.

A much lower magnetic field of $\approx 3\,\mu\text{G}$, comparable to the interstellar magnetic field, could explain such a high inverse Compton flux. From equation (3.38) it can be seen that the inverse Compton radiation of the electrons would show up at photon energies between 50 and 1000 TeV. Thus, this assumption can be tested with further data to be taken which would extend the photon spectrum to several tens of TeV.

The high inverse Compton flux can also be explained if the energy loss is much higher than assumed. A higher energy density in the photon field is necessary to make the inverse Compton scattering more efficient (eq. 3.31). From equation (3.36) the required energy density can be approximated:

$$U_{\text{rad}} = U_{\text{mag}} \frac{w_\gamma}{w_{\text{X}}} \approx 250 \left(\frac{B}{100\,\mu\text{G}}\right)^2 \text{eV}\,\text{cm}^{-3}.$$

For a magnetic field of $300\,\mu\text{G}$ this would require $2250\,\text{eV}\,\text{cm}^{-3}$ which is almost four orders of magnitude larger than the energy density in the cosmic microwave background (eq. 3.32). Candidates for further radiation fields are the infrared background and star light background. These background photon fields are not uniformly distributed in the universe like the cosmic microwave background. Therefore, their energy densities are not easy to estimate. However, the required energy density is too high to be explained by these backgrounds. Additionally, the inverse Compton scattering on these photons is in the Klein-Nishina regime (eq. 3.29) and the energy loss is less efficient.

Bremsstrahlung

Another energy loss mechanism for electrons is bremsstrahlung. Based on the assumption that the X-ray emission is synchrotron radiation in a magnetic field of 300 μG, the energy of the electrons was estimated to be at least 10 TeV. These electrons would emit bremsstrahlung photons with a mean energy of $\approx$ 3 TeV. Using equation (3.35) one can estimate the energy loss due to bremsstrahlung compared to inverse Compton scattering on the cosmic microwave background. This relation depends on the electron energy for which 10 TeV will be assumed. For this assumption the expected energy flux due to bremsstrahlung is

$$w_{\mathrm{br}} = 0.004 \left(\frac{n}{1\,\mathrm{cm}^{-3}} \right) w_{\mathrm{IC}}.$$

In Fig. 6.2 the bremsstrahlung energy flux expected from 10 TeV electrons and various densities of the interstellar material is shown. It can be seen that the inverse Compton scattering is much more efficient than the bremsstrahlung process. Therefore, the bremsstrahlung radiation can be neglected.

Summary

The observed synchrotron emission is evidence for the acceleration of electrons. These electrons undergo inverse Compton scattering on the cosmic microwave background producing γ-rays. From the synchrotron energy flux the expected inverse Compton radiation was estimated. It could be shown that the observed energy flux in γ-rays is three to four orders of magnitude higher than expected. Therefore, the observations can only partly be explained as being inverse Compton emission of accelerated electrons. It is likely that another radiation component contributes significantly to the γ-ray flux.

6.3.2 Hadronic Scenario

Another possible population of source particles capable of γ-ray production are protons which were accelerated in the shock front. These protons can undergo nuclear interactions with the ambient interstellar matter producing π^0 mesons. These mesons decay into γ-ray photons. Let us assume that the measured γ-ray flux is entirely due to π^0-decay produced in nuclear interactions. It has been shown in section 3.6.1 that these protons must have energies between between 5 and 100 TeV in order to produce photons of energies between 0.5 and 10 TeV. Further on it was discussed that the γ-ray spectrum reflects the shape of the initial proton spectrum. Thus, protons with energies between 5 and 100 TeV following a power law with spectral index 2.1 are required to explain the observed γ-ray flux. The spectral index of about 2 suggests that these protons are accelerated by Diffusive Shock Acceleration in the shock front of the supernova remnant.

Assuming that the γ-rays are emitted isotropically by the supernova remnant one can calculate from the γ-ray energy flux of $w_\gamma \approx 10^{-10}\,\mathrm{erg\,cm^{-2}\,s^{-1}}$ the total γ-ray luminosity due to π^0-decay:

$$L_\gamma = 4\pi d^2 w_\gamma,$$

where d is the distance of the observer to the supernova remnant. With equation (3.17) one can calculate the energy in protons which is required to produce the observed γ-ray flux:

$$W_p(5-100\,\mathrm{TeV}) = \tau_{\pi^0} 4\pi d^2 w_\gamma$$

$$= 1.9\times 10^{48}\left(\frac{n}{\mathrm{cm^{-3}}}\right)^{-1}\left(\frac{d}{200\,\mathrm{pc}}\right)^{2}\left(\frac{w_\gamma}{10^{-10}\,\mathrm{erg\,cm^{-2}\,s^{-1}}}\right)\,\mathrm{erg}.$$

For this calculation the knowledge of the density of the interstellar matter and the distance to the supernova remnant is required. For a density of $1\,\mathrm{cm^{-3}}$ and a distance of 200 pc an energy in protons of $\approx 10^{48}$ erg is required which could easily be provided by a supernova remnant with a kinetic energy of 10^{51} erg.

Before the effects of the density and distance on the energy estimate are discussed the total energy in accelerated protons will be calculated. The observed γ-rays reflect only a part of the proton population. Assuming that the proton population follows a power law with spectral index 2.1 down to an energy of 1 GeV (the rest mass of the proton) one can estimate the total energy in the proton population between 1 GeV and 100 TeV to be

$$W_{\mathrm{tot}} = W(1\,\mathrm{GeV}-100\,\mathrm{TeV}) = 2.6 W_p(5-100\,\mathrm{TeV}).$$

The total energy in protons as a function of the distance to the supernova remnant is shown in Fig. 6.3. Several estimates for the density of the interstellar material are denoted by the lines. From X-ray observations the density of the ambient material surrounding RX J0852.0−4622 was estimated to be $0.6(d/200\,\mathrm{pc})^{-0.5}\,\mathrm{cm^{-3}}$ [AIS99] or to be $0.9(d/200\,\mathrm{pc})^{-0.5}\,\mathrm{cm^{-3}}$ [TMA+00], depending on the distance d to the SNR. In addition, curves for a density of $1\,\mathrm{cm^{-3}}$, a low density of $0.1\,\mathrm{cm^{-3}}$ and a relatively high density of $10\,\mathrm{cm^{-3}}$ are shown to illustrate the range of possible densities. The various distance estimates are illustrated by shaded areas and black lines. It can be seen that for small distances and low densities the total amount of energy in protons is in the order of several percent up to 30% of the kinetic energy of supernovae ($\sim 10^{51}$ erg). In these cases RX J0852.0−4622 would be an efficient accelerator of protons and could contribute to the cosmic ray production. Higher densities of the interstellar medium would make the energy loss process more

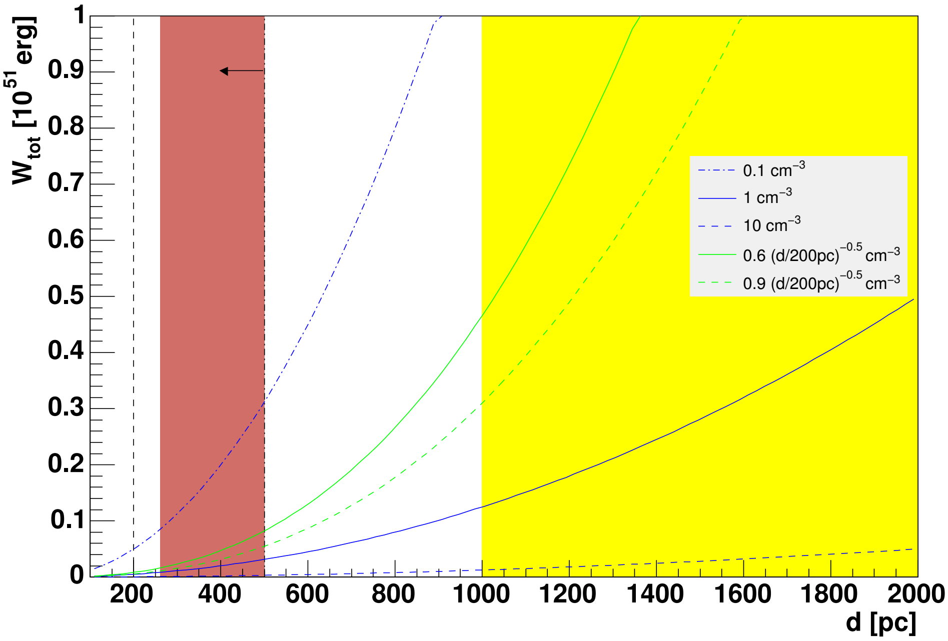

Figure 6.3: **The total energy in protons.** The plot shows the total energy in protons in units of 10^{51} erg as function of the distance to the SNR. The green lines denote the density of the interstellar medium as inferred from X-ray observations [AIS99, TMA$^+$00], the blue lines denote fixed densities. The shaded areas represent the distance estimates by **(author?)** [BYH05] (red) and **(author?)** [SHE$^+$01] (yellow). The distance of 200 pc [ISB$^+$98, AIS99] is denoted by the dashed black line. The upper limit of **(author?)** [AIS99] is represented by the dot-dashed black line and the arrow.

efficient. Thus, the transfer of only a small fraction of the kinetic energy of the supernova remnant to the accelerated protons would be required to explain the observed energy flux in γ-rays.

On the other hand, much larger distances to RX J0852.0−4622 are discussed by **(author?)** [SHE$^+$01]. For such large distances the low densities of the interstellar medium discussed by **(author?)** [AIS99] and **(author?)** [TMA$^+$00] would require more energy than the supernova can provide. Hence, a combination of a large distance and interaction with interstellar material of low density cannot explain the observed γ-rays as the result of accelerated protons. A large distance of several kpc would place RX J0852.0−4622 near the Vela Molecular Ridge, a cloud of dense molecular hydrogen. If the supernova remnant is interacting with a cloud of denser material then the energy loss would be more efficient and only a fraction of the kinetic energy of the supernova needs to be transferred to accelerated protons. For densities of more than $10\,\mathrm{cm}^{-3}$ the energy loss becomes very efficient and only a small fraction of the kinetic energy of the supernova is required to be transferred to protons.

Obviously, the distance to the supernova remnant and the density of the ambient interstellar medium are crucial ingredients in the interpretation of the observation with respect to the acceleration of protons. However, it can be seen that for certain combinations of assumed distances and densities the supernova remnant could indeed deliver the required energy to explain the observed γ-ray flux as originating from the interaction of accelerated protons with ambient material.

6.4 Conclusion

The observation of non-thermal radiation from the shell of the RX J0852.0 −4622 supernova remnant in X-rays and γ-rays is evidence for the acceleration of charged particles in the shell. A final conclusion on the type of accelerated particles cannot be drawn yet. The synchrotron emission in X-ray is evidence for the acceleration of electrons. The interaction of these electrons with the cosmic microwave background results in the emission of γ-rays. However, the γ-ray radiation expected from inverse Compton scattering of electrons is far too low to explain the observed flux. Thus, it is likely that another mechanism contributes to the γ-ray emission of RX J0852.0−4622. Interpreting the observed γ-ray flux as originating from accelerated protons the total amount of energy in protons was estimated. For a wide range of distances to the supernova remnant and the density of the interstellar material this energy makes up a fraction of several percent of the assumed kinetic energy of the supernova. According to the estimation laid out in section 1.3, the transfer of several percent of the supernova remnant's kinetic energy to the acceleration of protons is required if supernova remnants are the sources of galactic cosmic rays. Thus, RX J0852.0−4622 is a good candidate for contributing to the acceleration of cosmic rays.

6.5 Outlook

As no final conclusion on the particles generating the observed γ-ray flux can be drawn yet, further observations and studies are needed.

This work provided a spectrum of the γ-ray emission with photon energies between 0.5 and 10 TeV. A spectrum over a larger energy range would allow to distinguish the emission processes using the spectral shape of the emission.

The analysis presented here required a hard cut on the image intensities for background suppression. This cut resulted in a high energy threshold. Improved background suppression methods would avoid this hard cut and would extend the spectrum to lower energies of about 100 GeV. The H.E.S.S. array will be upgraded with one telescope with roughly $600\,\mathrm{m}^2$ mirror area and a camera field of view of 3.5°. This H.E.S.S.–II telescope, operational in 2008, will reduce the energy threshold to $\approx 20\,\mathrm{GeV}$ [P.05].

A further extension of the spectrum to lower energies will be provided by the GLAST satellite [GLA05] which will start its observations in 2007. GLAST is dedicated to the observation of γ-rays in the range between 20 MeV and 300 GeV with angular resolutions of $< 3.5°$ (at 100 MeV) and $< 0.15°$ (at more than 10 GeV).

The detection of a steepening and a cut-off of the photon spectrum at higher energies would allow to draw conclusions on the maximum energy of the accelerated particles. An extension of the spectrum to higher energies of several tens of TeV can be achieved with further observations at high zenith angles. Further observations would also reduce the uncertainties of the spectral points and would provide a more accurate spectrum. Additionally, data with higher statistic would allow detailed studies of the morphology. In addition to the spatial distribution of the γ-ray emission, differences in the spectral shape at different points of the shell could be investigated.

The discussion of the emission processes in this work is based on very rough estimations which did not take the spectrum of the source particles into account. Additionally, it is likely that the accelerated particles already lose energy during the acceleration process. Thus, the different energy loss processes cannot be discussed independently. Simulations of the acceleration and energy loss processes could provide models for the multi-wavelength emission of the supernova remnant which can be fit to the observational data. This work was already performed for the supernova remnant RX J1713.7−3946 [AAB$^+$05c]. The shell-type supernova remnant RX J1713.7−3946 is the first source for which an extended γ-ray morphology was observed [AAA$^+$04b].

For the interpretation of the γ-ray emission as the emission of accelerated protons the density of the interstellar material is important. The supernova remnant could expand into almost empty interstellar space with a very low density of material or can interact with clouds of high densities. A candidate for interaction with RX J0852.0−4622 is the Vela Molecular Ridge (VMR). The VMR is a molecular cloud which consists mainly of hydrogen. Such clouds also contain carbon monoxide (CO) the emission of which can be detected at radio wavelengths [see e.g. MYO$^+$01]. A correlation of CO emission and γ-ray emission would be a sign for interaction of the supernova remnant's shell with the molecular cloud and emission of γ-rays due to bremsstrahlung of electrons and interaction of protons. An interaction of only certain parts of the remnant with the cloud could also explain the non-uniform synchrotron and γ-ray emission.

The discussion presented here makes RX J0852.0−4622 a good candidate for the acceleration of cosmic rays. This encourages further deep observations and detailed studies.

Chapter 7

Summary

Shell-type supernova remnants are believed to be a main source of galactic cosmic rays. The expanding shells of these supernova remnants can accelerate charged particles to very high energies. The hypothesis that protons are accelerated can be tested with the observations of γ-rays originating from strong interactions of these protons with the interstellar material. RX J0852.0−4622 is a shell-type supernova remnant discovered in X-rays in 1998. Observations of γ-rays from this supernova remnant were carried out with the H.E.S.S. telescope system in the beginning of 2004.

H.E.S.S. is a system of four imaging Cherenkov telescopes. With its good sensitivity and large field of view it is the ideal instrument to observe extended sources in γ-rays with energies between 100 GeV and several tens of TeV. The experimental setup and the analysis chain which was used in this work has been verified using observations of the Crab Nebula. The Crab Nebula, the standard candle in TeV astronomy, could be detected with very high significance and the reconstructed energy spectrum and position are in good agreement with previous measurements.

Emission of γ-rays from RX J0852.0−4622 was detected with H.E.S.S. with a significance of $12\,\sigma$. The energy spectrum of the γ-rays was reconstructed in the range between 0.5 and 10 TeV. It follows a power law with a spectral index of $2.1 \pm 0.1_{\mathrm{stat}} \pm 0.2_{\mathrm{syst}}$. The integral photon flux above 1 TeV is found to be $(1.9 \pm 0.2_{\mathrm{stat}} \pm 0.4_{\mathrm{syst}}) \times 10^{-11}\,\mathrm{cm}^{-2}\mathrm{s}^{-1}$, which is at the level of the flux from the Crab Nebula at these energies. The energy flux in photons between 0.5 and 10 TeV is $(9 \pm 1_{\mathrm{stat}} \pm 2_{\mathrm{syst}}) \times 10^{-11}\,\mathrm{erg\,cm}^{-2}\,\mathrm{s}^{-1}$.

The spatial distribution of the emission suggests that the emission region is roughly a shell-like structure, with brightening of the northern, northwestern, western and southern part of the shell. Following the detection of RX J1713.7−3946 with H.E.S.S.in 2004, RX J0852.0−4622 is the second supernova remnant of which an extended γ-ray morphology could be detected.

The brightest part is the north-western part, coincident with the brightest X-ray emission and the detection by CANGAROO. The morphology was found to be correlated with the emission in X-rays. This suggests that both emissions are produced in the same regions. As the X-ray emission is synchrotron radiation from electrons accelerated in the shock front of the expanding shell, it is concluded that the γ-rays also originate from the shock front of the shell.

Two γ-ray emission scenarios have been discussed. The synchrotron emission in X-rays is produced by accelerated electrons with energies in the order of 10 TeV. These electrons interact with the photons of the cosmic microwave background via inverse Compton scattering producing γ-rays. From the observed synchrotron energy flux the energy flux to be expected from inverse Compton scattering was estimated. The observed energy flux in γ-rays is too high to be explained solely by inverse Compton emission. Bremsstrahlung was found to be less efficient than inverse Compton scattering and can therefore not explain the high γ-ray flux. Hence, it is likely that another radiation component contributes to the γ-ray emission.

Accelerated protons can produce γ-rays in strong interactions with the ambient interstellar material. From the observed γ-ray flux the total energy in protons was estimated. Crucial parameters in this estimation are the distance to the supernova remnant and the density of the interstellar medium. These parameters are currently under discussion in the literature. It could be shown for a wide range of both parameters that the supernova remnant can provide the energy in protons required to produce the observed γ-rays. Depending on these parameters, the transfer of 1% up to 30% of the kinetic energy kinetic energy of the supernova remnant to the acceleration of protons is required to explain the observed energy flux. Thus, RX J0852.0$-$4622 is indeed a candidate for acceleration of cosmic rays.

The conclusions of this work encourage further studies of RX J0852.0 $-$4622 to establish it as accelerator of cosmic rays. It is required to extend the γ-ray spectrum to both lower and higher energies. This can be achieved with further observations with H.E.S.S. These observations could reveal deviations from the power law spectrum providing more information on the underlying photon production mechanism. Further on, the morphology of the emission region and differences in the photon spectrum over the remnant can be investigated in detail. The future upgrade of H.E.S.S. and the start of new experiments will allow to further extend the energy spectrum to lower energies.

The work presented here marks only the beginning of detailed γ-ray observations and studies of RX J0852.0$-$4622. The detection of extended morphologies of supernova remnants with H.E.S.S. is a milestone in the search for the sources of the cosmic rays. The observation of shell-type supernova remnants in γ-rays could finally bring the evidence that these supernova remnants contribute to the acceleration of cosmic rays.

Bibliography

[AA00] Aharonian, F. A.; Atoyan, A. M.: Broad-band diffuse gamma ray emission of the galactic disk. In: *A&A*, volume 362:pp. 937–952, October 2000.

[AAA⁺04a] Aharonian, F.; Akhperjanian, A. G.; Aye, K.-M.; Bazer-Bachi, A. R.; Beilicke, M.; Benbow, W.; Berge, D.; Berghaus, P.; Bernlöhr, K.; Bolz, O.; Boisson, C.; Borgmeier, C.; Breitling, F.; Brown, A. M.; Chadwick, P. M.; Chitnis, V. R.; Chounet, L.-M.; Cornils, R.; Costamante, L.; Degrange, B.; de Jager, O. C.; Djannati-Ataï, A.; Drury, L. O. '.; Ergin, T.; Espigat, P.; Feinstein, F.; Fleury, P.; Fontaine, G.; Funk, S.; Gallant, Y. A.; Giebels, B.; Gillessen, S.; Goret, P.; Guy, J.; Hadjichristidis, C.; Hauser, M.; Heinzelmann, G.; Henri, G.; Hermann, G.; Hinton, J.; Hofmann, W.; Holleran, M.; Horns, D.; Jung, I.; Khélifi, B.; Komin, N.; Konopelko, A.; Latham, I. J.; Gallou, R. L.; Lemoine, M.; Lemière, A.; Leroy, N.; Lohse, T.; Marcowith, A.; Masterson, C.; McComb, T. J. L.; de Naurois, M.; Nolan, S. J.; Noutsos, A.; Orford, K. J.; Osborne, J. L.; Ouchrif, M.; Panter, M.; Pelletier, G.; Pita, S.; Pohl, M.; Pühlhofer, G.; Punch, M.; Raubenheimer, B. C.; Raue, M.; Raux, J.; Rayner, S. M.; Redondo, I.; Reimer, A.; Reimer, O.; Ripken, J.; Rivoal, M.; Rob, L.; Rolland, L.; Rowell, G.; Sahakian, V.; Sauge, L.; Schlenker, S.; Schlickeiser, R.; Schuster, C.; Schwanke, U.; Siewert, M.; Sol, H.; Steenkamp, R.; Stegmann, C.; Tavernet, J.-P.; Théoret, C. G.; Tluczykont, M.; van der Walt, D. J.; Vasileiadis, G.; Vincent, P.; Visser, B.; Volk, H. J.; Wagner, S. J. (H.E.S.S.): Calibration of cameras of the H.E.S.S. detector. In: *Astroparticle Physics*, volume 22:pp. 109–125, November 2004.

[AAA⁺04b] Aharonian, F. A.; Akhperjanian, A. G.; Aye, K.-M.; Bazer-Bachi, A. R.; Beilicke, M.; Benbow, W.; Berge, D.; Berghaus, P.; Bernlöhr, K.; Bolz, O.; Boisson, C.; Borgmeier, C.; Breitling, F.; Brown, A. M.; Bussons Gordo, J.; Chadwick, P. M.; Chitnis, V. R.; Chounet, L.-M.; Cornils, R.; Costamante, L.; Degrange, B.; Djannati-Ataï, A.; Drury, L. O.; Ergin, T.; Espigat, P.; Feinstein, F.; Fleury, P.; Fontaine, G.; Funk, S.; Gallant, Y. A.; Giebels, B.; Gillessen, S.; Goret, P.; Guy, J.; Hadjichristidis, C.; Hauser, M.; Heinzelmann, G.; Henri, G.; Hermann, G.; Hinton, J. A.; Hofmann, W.; Holleran, M.; Horns, D.; de Jager, O. C.; Jung, I.; Khélifi, B.; Komin, N.; Konopelko, A.; Latham, I. J.; Le Gallou, R.; Lemoine, M.; Lemière, A.; Leroy, N.; Lohse, T.; Marcowith, A.; Masterson, C.; McComb, T. J. L.; de Naurois, M.; Nolan, S. J.; Noutsos, A.; Orford, K. J.; Osborne, J. L.; Ouchrif, M.; Panter, M.; Pelletier, G.; Pita, S.; Pohl, M.; Pühlhofer, G.; Punch, M.; Raubenheimer, B. C.; Raue, M.; Raux, J.; Rayner, S. M.; Redondo, I.; Reimer, A.; Reimer, O.; Ripken, J.; Rivoal, M.; Rob, L.; Rolland, L.; Rowell, G.; Sahakian, V.; Saugé, L.; Schlenker, S.; Schlickeiser, R.; Schuster, C.; Schwanke, U.; Siewert, M.; Sol, H.; Steenkamp, R.; Stegmann, C.; Tavernet, J.-P.; Théoret, C. G.; Tluczykont, M.; van der Walt, D. J.; Vasileiadis, G.; Vincent, P.; Visser, B.; Völk, H. J.; Wagner, S. J.: High-energy particle acceleration in the shell of a supernova remnant. In: *Nature*, volume 432:pp. 75–77, November 2004.

[AAB$^+$00] Aharonian, F. A.; Akhperjanian, A. G.; Barrio, J. A.; Bernlöhr, K.; Bojahr, H.; Calle, I.; Contreras, J. L.; Cortina, J.; Denninghoff, S.; Fonseca, V.; Gonzalez, J. C.; Götting, N.; Heinzelmann, G.; Hemberger, M.; Hermann, G.; Heusler, A.; Hofmann, W.; Horns, D.; Ibarra, A.; Kankanyan, R.; Kestel, M.; Kettler, J.; Köhler, C.; Kohnle, A.; Konopelko, A.; Kornmeyer, H.; Kranich, D.; Krawczynski, H.; Lampeitl, H.; Lindner, A.; Lorenz, E.; Lucarelli, F.; Magnussen, N.; Mang, O.; Meyer, H.; Mirzoyan, R.; Moralejo, A.; Padilla, L.; Panter, M.; Plaga, R.; Plyasheshnikov, A.; Prahl, J.; Pühlhofer, G.; Rauterberg, G.; Röhring, A.; Sahakian, V.; Samorski, M.; Schilling, M.; Schmele, D.; Schröder, F.; Stamm, W.; Tluczykont, M.; Völk, H. J.; Wiebel-Sooth, B.; Wiedner, C.; Willmer, M.; Wittek, W.: The Energy Spectrum of TEV Gamma Rays from the Crab Nebula as Measured by the HEGRA System of Imaging Air Cerenkov Telescopes. In: *ApJ*, volume 539:pp. 317–324, August 2000.

[AAB$^+$04] Aharonian, F.; Akhperjanian, A.; Beilicke, M.; Bernlöhr, K.;

Börst, H.-G.; Bojahr, H.; Bolz, O.; Coarasa, T.; Contreras, J. L.; Cortina, J.; Denninghoff, S.; Fonseca, M. V.; Girma, M.; Götting, N.; Heinzelmann, G.; Hermann, G.; Heusler, A.; Hofmann, W.; Horns, D.; Jung, I.; Kankanyan, R.; Kestel, M.; Kohnle, A.; Konopelko, A.; Kranich, D.; Lampeitl, H.; Lopez, M.; Lorenz, E.; Lucarelli, F.; Mang, O.; Mazin, D.; Meyer, H.; Mirzoyan, R.; Moralejo, A.; Oña-Wilhelmi, E.; Panter, M.; Plyasheshnikov, A.; Pühlhofer, G.; de los Reyes, R.; Rhode, W.; Ripken, J.; Rowell, G.; Sahakian, V.; Samorski, M.; Schilling, M.; Siems, M.; Sobzynska, D.; Stamm, W.; Tluczykont, M.; Vitale, V.; Völk, H. J.; Wiedner, C. A.; Wittek, W.: The Crab Nebula and Pulsar between 500 GeV and 80 TeV: Observations with the HEGRA Stereoscopic Air Cerenkov Telescopes. In: *ApJ*, volume 614:pp. 897–913, October 2004.

[AAB$^+$05a] Aharonian, F.; Akhperjanian, A. G.; Bazer-Bachi, A. R.; Beilicke, M.; Benbow, W.; Berge, D.; Bernlöhr, K.; Boisson, C.; Bolz, O.; Borrel, V.; Braun, I.; Breitling, F.; Brown, A. M.; Chadwick, P. M.; Chounet, L.-M.; Cornils, R.; Costamante, L.; Degrange, B.; Dickinson, H. J.; Djannati-Ataï, A.; O'C. Drury, L.; Dubus, G.; Emmanoulopoulos, D.; Espigat, P.; Feinstein, F.; Fontaine, G.; Fuchs, Y.; Funk, S.; Gallant, Y. A.; Giebels, B.; Gillessen, S.; Glicenstein, J. F.; Goret, P.; Hadjichristidis, C.; Hauser, M.; Heinzelmann, G.; Henri, G.; Hermann, G.; Hinton, J. A.; Hofmann, W.; Holleran, M.; Horns, D.; Jacholkowska, A.; de Jager, O. C.; Khélifi, B.; Komin, N.; Konopelko, A.; Latham, I. J.; Le Gallou, R.; Lemière, A.; Lemoine-Goumard, M.; Leroy, N.; Lohse, T.; Martin, J. M.; Martineau-Huynh, O.; Marcowith, A.; Masterson, C.; McComb, T. J. L.; de Naurois, M.; Nolan, S. J.; Noutsos, A.; Orford, K. J.; Osborne, J. L.; Ouchrif, M.; Panter, M.; Pelletier, G.; Pita, S.; Pühlhofer, G.; Punch, M.; Raubenheimer, B. C.; Raue, M.; Raux, J.; Rayner, S. M.; Reimer, A.; Reimer, O.; Ripken, J.; Rob, L.; Rolland, L.; Rowell, G.; Sahakian, V.; Saugé, L.; Schlenker, S.; Schlickeiser, R.; Schuster, C.; Schwanke, U.; Siewert, M.; Sol, H.; Spangler, D.; Steenkamp, R.; Stegmann, C.; Tavernet, J.-P.; Terrier, R.; Théoret, C. G.; Tluczykont, M.; Vasileiadis, G.; Venter, C.; Vincent, P.; Völk, H. J.; Wagner, S. J.: Detection of TeV γ-ray emission from the shell-type supernova remnant RX J0852.0-4622 with HESS. In: *A&A*, volume 437:pp. L7–L10, July 2005.

[AAB^{+}05b] Aharonian, F.; Akhperjanian, A. G.; Bazer-Bachi, A. R.; Beilicke, M.; Benbow, W.; Berge, D.; Bernlöhr, K.; Boisson, C.; Bolz, O.; Borrel, V.; Braun, I.; Breitling, F.; Brown, A. M.; Chadwick, P. M.; Chounet, L.-M.; Cornils, R.; Costamante, L.; Degrange, B.; Dickinson, H. J.; Djannati-Ataï, A.; O'C. Drury, L.; Dubus, G.; Emmanoulopoulos, D.; Espigat, P.; Feinstein, F.; Fontaine, G.; Fuchs, Y.; Funk, S.; Gallant, Y. A.; Giebels, B.; Gillessen, S.; Glicenstein, J. F.; Goret, P.; Hadjichristidis, C.; Hauser, M.; Heinzelmann, G.; Henri, G.; Hermann, G.; Hinton, J. A.; Hofmann, W.; Holleran, M.; Horns, D.; Jacholkowska, A.; de Jager, O. C.; Khélifi, B.; Komin, N.; Konopelko, A.; Latham, I. J.; Le Gallou, R.; Lemière, A.; Lemoine-Goumard, M.; Leroy, N.; Lohse, T.; Martin, J. M.; Martineau-Huynh, O.; Marcowith, A.; Masterson, C.; McComb, T. J. L.; de Naurois, M.; Nolan, S. J.; Noutsos, A.; Orford, K. J.; Osborne, J. L.; Ouchrif, M.; Panter, M.; Pelletier, G.; Pita, S.; Pühlhofer, G.; Punch, M.; Raubenheimer, B. C.; Raue, M.; Raux, J.; Rayner, S. M.; Reimer, A.; Reimer, O.; Ripken, J.; Rob, L.; Rolland, L.; Rowell, G.; Sahakian, V.; Saugé, L.; Schlenker, S.; Schlickeiser, R.; Schuster, C.; Schwanke, U.; Siewert, M.; Sol, H.; Spangler, D.; Steenkamp, R.; Stegmann, C.; Tavernet, J.-P.; Terrier, R.; Théoret, C. G.; Tluczykont, M.; Vasileiadis, G.; Venter, C.; Vincent, P.; Völk, H. J.; Wagner, S. J.: Observations of the Crab Nebula with H.E.S.S. In: *to be submitted to A&A*, 2005.

[AAB^{+}05c] Aharonian, F.; Akhperjanian, A. G.; Bazer-Bachi, A. R.; Beilicke, M.; Benbow, W.; Berge, D.; Bernlöhr, K.; Boisson, C.; Bolz, O.; Borrel, V.; Braun, I.; Breitling, F.; Brown, A. M.; Chadwick, P. M.; Chounet, L.-M.; Cornils, R.; Costamante, L.; Degrange, B.; Dickinson, H. J.; Djannati-Ataï, A.; O'C. Drury, L.; Dubus, G.; Emmanoulopoulos, D.; Espigat, P.; Feinstein, F.; Fontaine, G.; Fuchs, Y.; Funk, S.; Gallant, Y. A.; Giebels, B.; Gillessen, S.; Glicenstein, J. F.; Goret, P.; Hadjichristidis, C.; Hauser, M.; Heinzelmann, G.; Henri, G.; Hermann, G.; Hinton, J. A.; Hofmann, W.; Holleran, M.; Horns, D.; Jacholkowska, A.; de Jager, O. C.; Khélifi, B.; Komin, N.; Konopelko, A.; Latham, I. J.; Le Gallou, R.; Lemière, A.; Lemoine-Goumard, M.; Leroy, N.; Lohse, T.; Martin, J. M.; Martineau-Huynh, O.; Marcowith, A.; Masterson, C.; McComb, T. J. L.; de Naurois, M.; Nolan, S. J.; Noutsos, A.; Orford, K. J.; Osborne, J. L.; Ouchrif, M.; Panter, M.; Pelletier, G.; Pita, S.; Pühlhofer, G.;

Punch, M.; Raubenheimer, B. C.; Raue, M.; Raux, J.; Rayner, S. M.; Reimer, A.; Reimer, O.; Ripken, J.; Rob, L.; Rolland, L.; Rowell, G.; Sahakian, V.; Saugé, L.; Schlenker, S.; Schlickeiser, R.; Schuster, C.; Schwanke, U.; Siewert, M.; Sol, H.; Spangler, D.; Steenkamp, R.; Stegmann, C.; Tavernet, J.-P.; Terrier, R.; Théoret, C. G.; Tluczykont, M.; Vasileiadis, G.; Venter, C.; Vincent, P.; Völk, H. J.; Wagner, S. J.: A detailed spectral and morphological study of the gamma-ray supernova remnant RX J1713.7−3946. In: *to be submitted to A&A*, 2005.

[AAK97] Aharonian, F. A.; Atoyan, A. M.; Kifune, T.: Inverse Compton gamma radiation of faint synchrotron X-ray nebulae around pulsars. In: *MNRAS*, volume 291:pp. 162–176, October 1997.

[ACH^{+}03] Aye, K-M.; Chadwick, P.M.; Hadjichristidis, C.; Latham, J.; Le Gallou, R.; Noutsos, A.; McComb, T.J.L.; McKenny, J.; Osborne, J.L.; Rayner, S.M.; McMillan, J.E. for the H.E.S.S.čollaboration: A Novel Alternative to UV-Lasers Used in Flat-fielding VHE -ray Telescopes. In: *Proc. 28th ICRC, Tsukuba*, p. 2879. Univ. Academy Press, Tokyo, 2003.

[Afa96] Afanasiev et al.: In: *Proceedings Int. Symposium of Extremely High Energy Cosmic Rays*, volume Tokyo:p. 32, 1996.

[Aha04] Aharonian, F. A.: *Very high energy cosmic gamma radiation : a crucial window on the extreme Universe*. River Edge, NJ: World Scientific Publishing, 2004.

[AHKV97] Aharonian, F. A.; Hofmann, W.; Konopelko, A. K.; Völk, H. J.: The potential of ground based arrays of imaging atmospheric Cherenkov telescopes. I. Determination of shower parameters. In: *Astroparticle Physics*, volume 6:pp. 343–368, March 1997.

[AIS99] Aschenbach, B.; Iyudin, A. F.; Schönfelder, V.: Constraints of age, distance and progenitor of the supernova remnant RX J0852.0-4622/GRO J0852-4642. In: *A&A*, volume 350:pp. 997–1006, October 1999.

[AKC^{+}96] Anderson, G. P.; Kneizys, F. X.; Chetwynd, J. H.; Rothman, L. S.; Hoke, M. L.; Berk, A.; Bernstein, L. S.; Acharya, P. K.; Snell, H. E.; Mlawer, E.; Clough, S. A.; Wang, J.; Lee, S.; Revercomb, H. E.; Yokota, T.; Kimball, L. M.; Shettle, E. P.; Abreu, L. W.; Selby, J. E.: Reviewing atmospheric radiative transfer modeling: new developments in high- and moderate-resolution FASCODE/FASE and MODTRAN. In: Hays, Paul B.; Wang, Jinxue, editors, *Optical Spectroscopic Techniques and Instrumentation for Atmospheric and Space Research II*, volume 2830 of *Proc. SPIE*, pp. 82–93. October 1996.

[Asc98] Aschenbach, B.: Discovery of a young nearby supernova remnant. In: *Nature*, volume 396:pp. 141–142, 1998.

[BCC+03] Bernlöhr, K.; Carrol, O.; Cornils, R.; Elfahem, S.; Espigat, P.; Gillessen, S.; Heinzelmann, G.; Hermann, G.; Hofmann, W.; Horns, D.; Jung, I.; Kankanyan, R.; Katona, A.; Khélifi, B.; Krawczynski, H.; Panter, M.; Punch, M.; Rayner, S.; Rowell, G.; Tluczykont, M.; van Staa, R.: The optical system of the H.E.S.S. imaging atmospheric Cherenkov telescopes. Part I: layout and components of the system. In: *Astroparticle Physics*, volume 20:pp. 111–128, November 2003.

[BCD+94] Bird, D. J.; Corbato, S. C.; Dai, H. Y.; Dawson, B. R.; Elbert, J. W.; Emerson, B. L.; Green, K. D.; Huang, M. A.; Kieda, D. B.; Luo, M.; Ko, S.; Larsen, C. G.; Loh, E. C.; Salamon, M. H.; Smith, J. D.; Sokolsky, P.; Sommers, P.; Tang, J. K. K.; Thomas, S. B.: The cosmic-ray energy spectrum observed by the Fly's Eye. In: *ApJ*, volume 424:pp. 491–502, March 1994. doi:10.1086/173906.

[Ber00] Bernlöhr, K.: Monte carlo images of air showers. web resource, 2000. URL `http://www.mpi-hd.mpg.de/hfm/~bernlohr/HESS/MC_images`.

[Ber03] Bernlöhr, K.: CORSIKA and sim_hessarray - Simulation of the imaging atmospheric Cherenkov technique for the H.E.S.S. experiment. web resource, 2003. URL `http://www.mpi-hd.mpg.de/hfm/~bernlohr/HESS/Software/sim_hessarray/`.

[BKd+03] Borgmeier, C.; Komin, Nu.; de Naurois, M.; Schlenker, S.; Schwanke, U.; Stegmann, C. for the H.E.S.S.c̃ollaboration: The Central Data Acquisition System of the H.E.S.S. Telescope System. In: *Proc. 28th ICRC, Tsukuba*, p. 2891. Univ. Academy Press, Tokyo, 2003.

[BMS01] Borgmeier, C.; Mauritz, K.; Stegmann, C.: The central data acquisition system for the H.E.S.S. telescope system. In: *Proc. 27th ICRC, Hamburg*, p. 2896. Copernicus Gesellschaft, 2001.

[Bol04] Bolz, O.: *Absolute Energiekalibration der abbildenden Cherenkov-Teleskope des H.E.S.S. Experiments und Ergebnisse erster Beobachtungen des Supernova–Überrests RX J1713.7–3946*. Ph.D. thesis, Ruprecht–Karls–Universität Heidelberg, 2004.

[BRB$^+$05] Brun, R.; Rademakers, F.; Buncic, N.; Fine, V.; Canal, P.; Panacek, S.: ROOT, An Object-Oriented Data Analysis Framework. web resource, 2005. URL `http://root.cern.ch`.

[Bro05] Brown, A.M.: Atmospheric monitoring for the H.E.S.S. Cherenkov telescope array by transmissometer and LIDAR. In: *Proc. 29th ICRC, Pune*. 2005.

[BYH05] Bamba, A.; Yamazaki, R.; Hiraga, J. S.: Chandra Observations of A Galactic Supernova Remnant Vela Jr.: A New Sample of Thin Filaments Emitting Synchrotron X-Rays. In: *submitted to ApJ, astro-ph/0506331*, 2005.

[BZ00] Burgess, C. P.; Zuber, K.: Footprints of the newly discovered Vela supernova in Antarctic ice cores? In: *Astroparticle Physics*, volume 14:pp. 1–6, August 2000.

[CGJ$^+$03] Cornils, R.; Gillessen, S.; Jung, I.; Hofmann, W.; Beilicke, M.; Bernlöhr, K.; Crarol, O.; Elfahem, S.; Heinzelmann, G.; Hermann, G.; Horns, D.; Kankanyan, R.; Katona, A.; Krawczynski, H.; Panter, M.; Rayner, S.; Rowell, G.; Tluczykont, M.; van Staa, R.: The optical system of the H.E.S.S. imaging atmospheric Cherenkov telescopes. Part II: mirror alignment and point spread function. In: *Astroparticle Physics*, volume 20:pp. 129–143, November 2003.

[CGJ$^+$05] Cornils, R.; Gillessen, S.; Jung, I.; Hofmann, W.; Heinzelmann, G.; Hess Collaboration: Point spread function and long-term stability of the H.E.S.S. reflectors. In: *AIP Conf. Proc. 745: High Energy Gamma-Ray Astronomy*, pp. 736–741. February 2005.

[CRB99] Combi, J. A.; Romero, G. E.; Benaglia, P.: Radio Detection of the Supernova Remnant RX J0852.0-4622. In: *ApJ*, volume 519:pp. L177–L180, July 1999.

[DC57] Davies, J.M.; Cotton, E.S.: Design of the quartermaster solar furnace. In: *Solar Energy*, volume 1(2-3):p. 16, 1957.

[Der86] Dermer, C. D.: Secondary production of neutral pi-mesons and the diffuse galactic gamma radiation. In: *A&A*, volume 157:pp. 223–229, March 1986.

[DG00] Duncan, A. R.; Green, D. A.: The supernova remnant RX J0852.0-4622: radio characteristics and implications for SNR statistics. In: *A&A*, volume 364:pp. 732–740, December 2000.

[EHO+04] Eidelman, S.; Hayes, K.G.; Olive, K.A.; Aguilar-Benitez, M.; Amsler, C.; Asner, D.; Babu, K.S.; Barnett, R.M.; Beringer, J.; Burchat, P.R.; Carone, C.D.; Caso, C.; Conforto, G.; Dahl, O.; D'Ambrosio, G.; Doser, M.; Feng, J.L.; Gherghetta, T.; Gibbons, L.; Goodman, M.; Grab, C.; Groom, D.E.; Gurtu, A.; Hagiwara, K.; Hernández-Rey, J.J.; Hikasa, K.; Honscheid, K.; Jawahery, H.; Kolda, C.; Y., Kwon; Mangano, M.L.; Manohar, A.V.; March-Russell, J.; Masoni, A.; Miquel, R.; Mönig, K.; Murayama, H.; Nakamura, K.; Navas, S.; Pape, L.; Patrignani, C.; Piepke, A.; Raffelt, G.; Roos, M.; Tanabashi, M.; Terning, J.; Törnqvist, N.A.; Trippe, T.G.; Vogel, P.; Wohl, C.G.; Workman, R.L.; Yao, W.-M.; Zyla, P.A.; Armstrong, B.; Gee, P.S.; Harper, G.; Lugovsky, K.S.; Lugovsky, S.B.; Lugovsky, V.S.; Rom, A.; Artuso, M.; Barberio, E.; Battaglia, M.; Bichsel, H.; Biebel, O.; Bloch, P.; Cahn, R.N.; Casper, D.; Cattai, A.; Chivukula, R.S.; Cowan, G.; Damour, T.; Desler, K.; Dobbs, M.A.; Drees, M.; Edwards, A.; Edwards, D.A.; Elvira, V.D.; Erler, J.; Ezhela, V.V.; Fetscher, W.; Fields, B.D.; Foster, B.; Froidevaux, D.; Fukugita, M.; Gaisser, T.K.; Garren, L.; Gerber, H.-J.; Gerbier, G.; Gilman, F.J.; Haber, H.E.; Hagmann, C.; Hewett, J.; Hinchliffe, I.; Hogan, C.J.; Höhler, G.; Igo-Kemenes, P.; Jackson, J.D.; Johnson, K.F.; Karlen, D.; Kayser, B.; Kirkby, D.; Klein, S.R.; Kleinknecht, K.; Knowles, I.G.; Kreitz, P.; Kuyanov, Yu.V.; Lahav, O.; Langacker, P.; Liddle, A.; Littenberg, L.; Manley, D.M.; Martin, A.D.; Narain, M.; Nason, P.; Nir, Y.; Peacock, J.A.; Quinn, H.R.; Raby, S.; Ratcliff, B.N.; Razuvaev, E.A.; Renk, B.; Rolandi, G.; Ronan, M.T.; Rosenberg, L.J.; Sachrajda, C.T.; Sakai, Y.; Sanda, A.I.; Sarkar, S.; Schmitt, M.; Schneider, O.; Scott, D.; Seligman, W.G.; Shaevitz, M.H.; Sjöstrand, T.; Smoot, G.F.; Spanier, S.; Spieler, H.; Spooner, N.J.C.; Srednicki, M.; Stahl, A.; Stanev, T.; Suzuki, M.; Tkachenko, N.P.; Trilling, G.H.; Valencia, G.; van Bibber, K.; Vincter, M.G.; Ward, D.; Webber, B.R.; Whalley, M.; Wolfenstein, L.; Womersley, J.; Woody, C.L.; Zenin, O.V.; Zhu, R.-Y.: Review of Particle Physics. In: *Physics Letters B*, volume 592:pp. 1+, 2004. URL `http://pdg.lbl.gov`.

[FA03] Feinstein, F.; ANTARES collaboration: The analogue ring sampler: A front-end chip for ANTARES. In: *NIM A*, volume 504:p. 258, 2003.

[FC98] Feldman, G. J.; Cousins, R. D.: Unified approach to the classical statistical analysis of small signals. In: *Phys. Rev. D*, volume 57:pp. 3873–3889, April 1998.

[Fer49] Fermi, E.: On the Origin of the Cosmic Radiation. In: *Physical Review*, volume 75:pp. 1169–1174, April 1949.

[FHH$^+$04] Funk, S.; Hermann, G.; Hinton, J.; Berge, D.; Bernlöhr, K.; Hofmann, W.; Nayman, P.; Toussenel, F.; Vincent, P.: The trigger system of the H.E.S.S. telescope array. In: *Astroparticle Physics*, volume 22:pp. 285–296, November 2004.

[Gai90] Gaisser, T. K.: *Cosmic rays and particle physics*. Cambridge and New York, Cambridge University Press, 1990.

[Gil03] Gillessen, S. (for the H.E.S.S. collaboration): Arcsecond level pointing of the h.e.s.s. telescopes. In: *Proc. 28th ICRC, Tsukuba*, p. 2899. Univ. Academy Press, Tokyo, 2003.

[Gil04] Gillessen, S.: *Sub-Bogenminuten-genaue Positionen von TeV-Quellen mit H.E.S.S.* Ph.D. thesis, Ruprecht–Karls–Universität Heidelberg, 2004.

[GLA05] 2005. URL `http://www-glast.stanford.edu`.

[Gre66] Greisen, K.: End to the Cosmic-Ray Spectrum? In: *Physical Review Letters*, volume 16:pp. 748–750, April 1966. doi:10.1103/PhysRevLett.16.748.

[Gri71] Grigorov et al.: In: *Proceedings 12th ICRC, Hobart*, p. 1760, 1971.

[GS64] Ginzburg, V. L.; Syrovatskii, S. I.: *The Origin of Cosmic Rays*. The Origin of Cosmic Rays, New York: Macmillan, 1964, 1964.

[GS65] Ginzburg, V. L.; Syrovatskii, S. I.: Cosmic Magnetobremsstrahlung (synchrotron Radiation). In: *ARA&A*, volume 3:pp. 297–+, 1965. doi:10.1146/annurev.aa.03.090165.001501.

[GS04] Green, D. A.; Stephenson, F. R.: On the footprints of supernovae in Antarctic ice cores. In: *Astroparticle Physics*, volume 20:pp. 613–615, February 2004.

[HAB+98] Hillas, A. M.; Akerlof, C. W.; Biller, S. D.; Buckley, J. H.; Carter-Lewis, D. A.; Catanese, M.; Cawley, M. F.; Fegan, D. J.; Finley, J. P.; Gaidos, J. A.; Krennrich, F.; Lamb, R. C.; Lang, M. J.; Mohanty, G.; Punch, M.; Reynolds, P. T.; Rodgers, A. J.; Rose, H. J.; Rovero, A. C.; Schubnell, M. S.; Sembroski, G. H.; Vacanti, G.; Weekes, T. C.; West, M.; Zweerink, J.: The Spectrum of TeV Gamma Rays from the Crab Nebula. In: *ApJ*, volume 503:pp. 744–+, August 1998.

[Hes12] Hess, V.F.: Über Beobachtungen der durchdringenden Strahlen bei sieben Freiballonfahrten. In: *Physikalische Zeitschrift*, volume 13:p. 1084, 1912.

[HH62] Ho, P. Y.; Ho, P.: Ancient and mediaeval observations of comets and novae in Chinese sources. In: *Vistas in Astronomy*, volume 5:pp. 127–225, 1962.

[Hil85] Hillas, A. M.: Cerenkov light images of EAS produced by primary gamma. In: *NASA. Goddard Space Flight Center 19th Intern. Cosmic Ray Conf., Vol. 3 p 445-448 (SEE N85-34862 23-93)*, volume 3:pp. 445–448, August 1985.

[HJK+99] Hofmann, W.; Jung, I.; Konopelko, A.; Krawczynski, H.; Lampeitl, H.; Pühlhofer, G.: Comparison of techniques to reconstruct VHE gamma-ray showers from multiple stereoscopic Cherenkov images. In: *Astroparticle Physics*, volume 12:pp. 135–143, November 1999.

[HKC+98] Heck, D.; Knapp, J.; Capdevielle, J.N.; Schatz, G.; Thouw, T.: CORSIKA: A Monte Carlo Code to Simulate Extensive Air Showers. Technical Report FZKA 6019, Forschungszentrum Karlsruhe Report, 1998.

[HT99] Han, J. L.; Tian, W. W.: Pulsars identified from the NRAO VLA Sky Survey. In: *A&AS*, volume 136:pp. 571–577, May 1999.

[IAB+05] Iyudin, A. F.; Aschenbach, B.; Becker, W.; Dennerl, K.; Haberl, F.: XMM-Newton observations of the supernova remnant RX J0852.0-4622/GRO J0852-4642. In: *A&A*, volume 429:pp. 225–234, January 2005.

[ISB+98] Iyudin, A. F.; Schönfelder, V.; Bennett, K.; Bloemen, H.; Diehl, R.; Hermsen, W.; Lichti, G. G.; van der Meulen, R. D.; Ryan, J.; Winkler, C.: Emission from ^{44}Ti associated with a previously unknown Galactic supernova. In: *Nature*, volume 396:pp. 142–144, 1998.

[JE91] Jones, F. C.; Ellison, D. C.: The plasma physics of shock acceleration. In: *Space Science Reviews*, volume 58:pp. 259–346, 1991.

[KAA+96] Kohnle, A.; Aharonian, F.; Akhperjanian, A.; Bradbury, S.; Daum, A.; Deckers, T.; Fernandez, J.; Fonseca, V.; Hemberger, M.; Hermann, G.; Hess, M.; Heusler, A.; Hofmann, W.; Kankanian, R.; Köhler, C.; Konopelko, A.; Lorenz, E.; Mirzoyan, R.; Müller, N.; Panter, M.; Petry, D.; Plyasheshnikov, A.; Rauterberg, G.; Samorski, M.; Stamm, W.; Ulrich, M.; Völk, H. J.; Wiedner, C. A.; Wirth, H.: Stereoscopic imaging of air showers with the first two HEGRA Cherenkov telescopes. In: *Astroparticle Physics*, volume 5:pp. 119–131, August 1996.

[KBV05] Ksenofontov, L. T.; Berezhko, E. G.; Völk, H. J.: Dependence of the gamma-ray emission from SN 1006 on the astronomical parameters. In: *submitted to A&A, astro-ph/0508318*, 2005.

[KEK+05] Katagiri, H.; Enomoto, R.; Ksenofontov, L. T.; Mori, M.; Adachi, Y.; Asahara, A.; Bicknell, G. V.; Clay, R. W.; Doi, Y.; Edwards, P. G.; Gunji, S.; Hara, S.; Hara, T.; Hattori, T.; Hayashi, S.; Itoh, C.; Kabuki, S.; Kajino, F.; Kawachi, A.; Kifune, T.; Kiuchi, R.; Kubo, H.; Kurihara, T.; Kurosaka, R.; Kushida, J.; Matsubara, Y.; Miyashita, Y.; Mizumoto, Y.; Muraishi, H.; Muraki, Y.; Naito, T.; Nakamori, T.; Nakase, T.; Nishida, D.; Nishijima, K.; Ohishi, M.; Okumura, K.; Patterson, J. R.; Protheroe, R. J.; Sakamoto, N.; Sakamoto, Y.; Swaby, D. L.; Tanimori, T.; Tanimura, H.; Thornton, G. J.; Tsuchiya, K.; Watanabe, S.; Yamaoka, T.; Yanagita, S.; Yoshida, T.; Yoshikoshi, T.: Detection of Gamma Rays around 1 TeV from RX J0852.0-4622 by CANGAROO-II. In: *ApJ*, volume 619:pp. L163–L166, February 2005.

[KMH05] Khélifi, B.; Masterson, C.; Hinton, J.: VHE observations of pulsar wind nebulae with H.E.S.S. In: *29th ICRC, Pune*. 2005.

[KZ97] Klapdor-Kleingrothaus, H. V.; Zuber, K.: *Teilchenastrophysik*. Stuttgart: Teubner, 1997.

[LBG$^+$03] Leroy, N.; Bolz, O.; Guy, J.; Jung, I.; Redondo, I.; Rolland, L.; Tavernet, J.-P.; Aye, K.-M.; Berghaus, P.; Bernlöhr, K.; Chadwick, P.M.; Chitnis, V.; de Naurois, M.; Djannati-Ataï, A.; Espigat, P.; Hermann, G.; Hinton, J.; Khélifi, B.; Kohnle, A.; LeGallou, R.; Masterson, C.; Pita, S.; Saitoh, T.; Théoret, C.; Vincent, P. for the H.E.S.S.c̃ollaboration: Calibration results for the first two H.E.S.S. array telescopes. In: *Proc. 28th ICRC, Tsukuba*, p. 2895. Univ. Academy Press, Tokyo, 2003.

[Le 03] Le Gallou, R.: Atmospheric Monitoring for the H.E.S.S. Project. In: *Proc. 28th ICRC, Tsukuba*, p. 2879. Univ. Academy Press, Tokyo, 2003.

[LM83] Li, T.-P.; Ma, Y.-Q.: Analysis methods for results in gamma-ray astronomy. In: *ApJ*, volume 272:pp. 317–324, September 1983.

[LNMS05] Le Gallou, R.; Nolan, S.J.; Masterson, C.; Spangler, D.: Atmospheric quality and H.E.S.S. array performance: study using the ceilometer and correction method for γ-ray data. H.E.S.S. internal note, May 2005.

[Lon92] Longair, M. S.: *High energy astrophysics. Vol.1: Particles, photons and their detection*. Cambridge, UK: Cambridge University Press, 2nd edition, 1992.

[Lon94] Longair, M. S.: *High energy astrophysics. Vol.2: Stars, the galaxy and the interstellar medium*. Cambridge, UK: Cambridge University Press, 2nd edition, 1994.

[LRW91] Lawrence, M.A.; Reid, R.J.O.; Watson, A.A.: The cosmic ray energy spectrum above 4×10^{17} eV as measured by the Haverah Park array. In: *J. Phys. G: Nucl. Phys.*, volume 17:p. 733, 1991.

[MBv05] Masterson, C.; Benbow, W.R.; van Eldik, C.: Observations of the Crab nebula with H.E.S.S. In: *29th ICRC, Pune*. 2005.

[MD01] Malkov, M. A.; Drury, L.O'C.: Nonlinear theory of diffusive acceleration of particles by shock waves . In: *Reports of Progress in Physics*, volume 64:pp. 429–481, April 2001.

[Mor97] Mori, M.: The Galactic Diffuse Gamma-Ray Spectrum from Cosmic-Ray Proton Interactions. In: *ApJ*, volume 478:pp. 225–+, March 1997. doi:10.1086/303785.

[MYO$^+$01] Moriguchi, Y.; Yamaguchi, N.; Onishi, T.; Mizuno, A.; Fukui, Y.: A ^{12}CO (J = 1 − 0) Survey of Molecular Clouds toward the Vela Supernova Remnant with NANTEN. In: *PASJ*, volume 53:pp. 1025–1036, December 2001.

[MyS05] 2005. URL `http://www.mysql.com`.

[NBC$^+$97] Norman, E. B.; Browne, E.; Chan, Y. D.; Goldman, I. D.; Larimer, R.-M.; Lesko, K. T.; Nelson, M.; Wietfeldt, F. E.; Zlimen, I.: On the Half-Life of 44Ti. In: *Nuclear Physics A*, volume 621:pp. 92–96, August 1997.

[NHH$^+$84] Nagano, M.; Hara, T.; Hatano, Y.; Hayashida, N.; Kawaguchi, S.; Kamata, K.; Kifune, T.; Mizumoto, Y.: Energy spectrum of primary cosmic rays between $10^{14.5}$ and 10^{18} eV. In: *J. Phys. G: Nucl. Phys.*, volume 10:p. 1295, 1984.

[NTM$^+$92] Nagano, M.; Teshima, M.; Matsubara, Y.; Dai, H.Y.; Hara, T.; Hayashida, N.; Honda, M.; Ohoka, H.; Yoshida, S.: Energy spectrum of primary cosmic rays above $10^{17.0}$ eV determined from extensive air shower experiments at Akeno. In: *J. Phys. G: Nucl. Phys.*, volume 18:p. 423, 1992.

[omn05] 2005. URL `http://omniorb.sourceforge.net`.

[P.05] P., Vincent: H.E.S.S. Phase II. In: *Proc. 29th ICRC, Pune*. 2005.

[Pad00] Padmanabhan, T.: *Theoretical astrophysics. Vol.1: Astrophysical processes.* Cambridge, UK: Cambridge University Press, October 2000.

[Pad01] Padmanabhan, T.: *Theoretical Astrophysics, Vol. 2: Stars and Stellar Systems*. Cambridge, UK: Cambridge University Press, April 2001.

[ROS05] ROSAT: 2005. URL `http://www.xray.mpe.mpg.de/cgi-bin/rosat/rosat-survey`.

[RSZP79] Rood, R. T.; Sarazin, C. L.; Zeller, E. J.; Parker, B. C.: X- or gamma-rays from supernovae in glacial ice. In: *Nature*, volume 282:pp. 701–703, December 1979.

[SHE+01] Slane, P.; Hughes, J. P.; Edgar, R. J.; Plucinsky, P. P.; Miyata, E.; Tsunemi, H.; Aschenbach, B.: RX J0852.0-4622: Another Nonthermal Shell-Type Supernova Remnant (G266.2-1.2). In: *ApJ*, volume 548:pp. 814–819, February 2001.

[SL05] Schwanke, U.; Lohse, T.: Calculating the Error of Correlation Coefficients. H.E.S.S. internal note, February 2005.

[SOS+91] Seo, E. S.; Ormes, J. F.; Streitmatter, R. E.; Stochaj, S. J.; Jones, W. V.; Stephens, S. A.; Bowen, T.: Measurement of cosmic-ray proton and helium spectra during the 1987 solar minimum. In: *ApJ*, volume 378:pp. 763–772, September 1991. doi: 10.1086/170477.

[Swo97] Swordy, S. P.: web resource, 1997. URL `http://astroparticle.uchicago.edu/cosmic_ray_spectrum_picture.htm`.

[TMA+00] Tsunemi, H.; Miyata, E.; Aschenbach, B.; Hiraga, J.; Akutsu, D.: Overabundance of Calcium in the Young SNR RX J0852-4622: Evidence of Over-Production of ^{44}Ti. In: *PASJ*, volume 52:pp. 887–893, October 2000.

[VAB+99] Voges, W.; Aschenbach, B.; Boller, T.; Bräuninger, H.; Briel, U.; Burkert, W.; Dennerl, K.; Englhauser, J.; Gruber, R.; Haberl, F.; Hartner, G.; Hasinger, G.; Kürster, M.; Pfeffermann, E.; Pietsch, W.; Predehl, P.; Rosso, C.; Schmitt, J. H. M. M.; Trümper, J.; Zimmermann, H. U.: The ROSAT all-sky survey bright source catalogue. In: *A&A*, volume 349:pp. 389–405, September 1999.

[VBK05] Völk, H. J.; Berezhko, E. G.; Ksenofontov, L. T.: Magnetic field amplification in Tycho and other shell-type supernova remnants.

In: *A&A*, volume 433:pp. 229–240, April 2005. doi:10.1051/0004-6361:20042015.

[Ve03] Vincent, P.; et al.: Performance of the H.E.S.S. Cameras. In: *International Cosmic Ray Conference*, pp. 2887–+. July 2003.

[Wer93] Werner, K.: Strings, pomerons and the VENUS model of hadronic interactions at ultrarelativistic energies. In: *Phys. Rep.*, volume 232:pp. 87–299, September 1993. doi:10.1016/0370-1573(93)90078-R.

[Wig00] Wigmans, R.: *Calorimetry - Energy Measurement in Particle Physics*, volume 107 of *International Series of Monographs on Physics*. Oxford Univerisity Press, September 2000.

[WW89] Wdowczyk, J.; Wolfendale, A. W.: Highest energy cosmic rays. In: *Annual Review of Nuclear and Particle Science*, volume 39:pp. 43–71, 1989.

Appendix A

Appendix

A.1 Data Sets

run no.	wobble offset	live time [s]	ZA	BG regions
23304	+0.5° Dec	1541	52.4°	1
23309	−0.5° Dec	1585	48.3°	1
23310	+0.5° Dec	1594	50.2°	1
23526	+0.54° RA	1574	46.3°	1
23544	−0.54° RA	1580	48.8°	1
23545	+0.5° Dec	1577	46.3°	1
23546	−0.5° Dec	888	46.0°	1
23547	+1.62° RA	879	44.8°	1
23559	−0.54° RA	1578	45.4°	9
23577	−0.54° RA	1575	45.3°	1
23579	−1.62° RA	910	47.3°	1
23592	−0.5° RA	1581	47.8°	9
23593	−0.5° Dec	1582	46.2°	1
23608	−0.5° Dec	1594	49.3°	1
23642	+0.5° Dec	1585	51.1°	1
23662	−0.5° Dec	1565	46.0°	1
23663	−0.5° Dec	1568	46.4°	1

Table A.1: **Run parameters of the Crab data set.** The table summarises the run number, wobble offset, live time, mean zenith angle (ZA) and the number of background regions.

run no.	wobble offset	live time [s]	ZA
18928	+0.5° Dec	1461	22.8°
18929	−0.5° Dec	1445	24.7°
18947	+0.5° Dec	1465	22.8°
18948	−0.5° Dec	1434	24.1°
18949	+0.5° Dec	1117	25.4°
18994	+0.5° Dec	1484	22.9°
18995	−0.5° Dec	1463	25.3°
18996	+0.5° Dec	1499	27.6°

Table A.2: **Run parameters of the RX J0852.0−4622 on-source data set.** The table summarises the run numbers, wobble offsets, live times and mean zenith angles (ZA) of the data set.

run no.	obs. pos.	live time [s]	ZA
20348	2	1502	19.8°
20420	2	1503	19.1°
20946	2	1524	18.0°
21010	2	1548	33.7°
21020	2	1548	34.8°
21128	2	1556	21.3°
21140	1	1564	32.9°
21143	1	1544	19.1°
21159	1	1560	32.8°
21162	1	1540	19.1°
21193	2	1558	29.0°

Table A.3: **Run parameters of the RX J0852.0−4622 off-source data set.** The table summarises the run numbers, observation positions, live times and mean zenith angles (ZA). The observation positions are position 1 (RA $16\mathrm{h}43\mathrm{m}33\overset{\mathrm{s}}{.}59$, Dec $-39°45'44''$) and position 2 (RA $17\mathrm{h}43\mathrm{m}33\overset{\mathrm{s}}{.}59$, Dec $-39°45'44''$).

run no.	live time [s]	ZA
18416	1464	27.4°
18694	1513	27.9°
19134	1497	28.6°
19172	1492	26.0°
20045	1438	28.3°
20075	1465	29.4°
20123	1458	24.1°

Table A.4: **Run parameters of the RX J0852.0−4622 alternative off-source data set.** These runs were taken at the Vela pulsar. The observation position is (RA 8h35m21s, Dec $-44°40'30''$). The table summarises the run numbers, live times and mean observation zenith angles (ZA).

Acknowledgements

First of all I like to express my gratitude to my supervisor Thomas Lohse for giving me the opportunity to join the H.E.S.S. collaboration and to work on this interesting topic presented here. Without his lessons, the interesting discussions and his permanent help, this work would have been impossible.

Much help and support I received from the members of the Berlin H.E.S.S. group. The weekly meetings, daily conversations and the warm atmosphere are the base for fruitful scientific work. In particular I like to mention Christian Stegmann, for organising the work of the Berlin group and for putting me forward by asking the right questions; Ulli Schwanke, who had patience explaining fundamental correlations and statistics and for reading and commenting my thesis thoroughly; and my officemate Stefan "Schlenk" Schlenker, for being there, for his precise answers and for setting the way I try to follow.

To set up H.E.S.S., as well as analysis and interpretation of the data would have been impossible without the work of many people. I would like to thank all the members of the H.E.S.S. collaboration to make this thing work, for the good team work and nice discussions on all the interesting topics addressed by H.E.S.S. observations. I appreciate the theoretical works of Felix Aharonian and Yves Gallant indicating the direction of how to interpret the data. I am grateful to Wystan Benbow, Jim Hinton and Conor Masterson for discussing experimental aspects of H.E.S.S. in particular and gamma-ray astronomy in general.

Moreover, I would like to thank Stefan Wagner and Patrick Slane for providing the X-ray data used in this work. Valuable input I gained from reading the theses of David Berge, Tülün Ergin, Stefan Schlenker and Fabian Schmidt.

But there is not only help in terms of scientific support which I have got during my work. Without the organising ability of Veronika Fetting I would got stuck in bureaucratic paperwork. Olf Epler kept the computers running and gave me some insights into Linux. The tea and coffee breaks with the Berlin group including the numerous diploma students are unforgettable.

Friends make up an important part of live. Without them work would be impossible and live would be boring. I would like to take the opportunity to thank Jens Vanselow, for long nights discussing Life, the Universe and Everything, for the appropriate quotation, for being a friend. I shared my time at the university with Ralph Dollan, André Felbrich and Volker Schmidt, they remain friends since then. Furthermore, I would like to mention Anne Müller, Daniel Obée, Dieter Hackenberg and the fellows of the “Alm”. I thank all of you, we have spent a lot of time. I will miss you when I have left Berlin.

Last but not least, I wish to express my deepest gratitude to my family: Mum, Dad, “Oma”, my brother Niko and my “sister” Rachel Hill. Thank you very much, without you I would not have gone that far.

Selbständigkeitserklärung

Hiermit erkläre ich, die vorliegende Arbeit selbständig ohne fremde Hilfe verfasst und nur die angegebene Literatur und Hilfsmittel verwendet zu haben.

Nukri Randolf Komin
13. September 2005